USPC
Université Sorbonne
Paris Cité

université PARIS DIDEROT PARIS 7

Thèse de Doctorat

de l'Université Sorbonne Paris Cité

Préparée à l'Université Paris Diderot

Ecole Doctorale (ED°474) Frontières du Vivant (FdV)

Macromolécules et Microsystèmes en Biologie et en Médecine

Développement de Systèmes Biomimétiques Microfluidiques pour l'Etude du Processus Métastatique à Partir de Cellules Tumorales Circulantes

Study of the Metastatic Process of Circulating Tumour Cells by Organ-on-a-Chip *In Vitro* Models

Par Hamizah AHMAD-COGNART

Thèse de Doctorat de Frontières du Vivant

Dirigées par Jean-Louis VIOVY et Catherine VILLARD

Présentée et Soutenue Publiquement à l'Institut Pierre-Gilles de Gennes le 14 Septembre 2018

Présidente du jury	Christine CHOMIENNE, Professeur des Universités-Praticien Hospitalier, Université Paris 7
Rapporteurs	Dominique COLLARD, Directeur de Recherche, CNRS Emilie MAMESSIER, Charge de Recherche, INSERM
Examinateurs	Christine CHOMIENNE, Professeur des Universités-Praticien Hospitalier, Université Paris 7 Benoit LADOUX, Directeur de Recherche, Université Paris 7
Directeur de thèse	Jean-Louis VIOVY, Directeur de Recherche, CNRS
Co-directrice de thèse	Catherine VILLARD, Directeur de Recherche, CNRS

RÉSUMÉ / ABSTRACT

90% de la mortalité par cancer provient de tumeurs disséminées, ou métastases. Ces métastases se forment à partir de cellules tumorales qui s'échappent d'une tumeur primaire, circulent dans le sang, puis quittent les vaisseaux sanguins pour enfin aller nicher dans des organes distants et former des tumeurs secondaires. Les processus par lesquels ces cellules circulantes envahissent les organes distants, remodèlent leur environnement pour créer une «niche micrométastatique», prolifèrent pour produire des métastases macroscopiques, sont mal connus, principalement en raison d'un manque de modèles expérimentaux. En effet ces événements sont rares, se produisent à une échelle microscopique et à des localisations à priori inconnus.

La perte d'adhérence cellulaire des cellules tumorales se détachant des tissus tumoraux primaires est associée à un phénomène de transformation connu sous le nom de transition épithéliale-mésenchymateuse (EMT) conduisant à la perte des caractéristiques épithéliales.

Dans ce travail, nous avons souhaiter aborder la question du processus métastatiques par l'étude de l'influence de l'étape de circulation dans le flux sanguin sur différentes caractéristiques de cellules tumorales. Pour cela, des modèles microfluidiques contenant des constrictions mécaniques afin d'imiter la microcirculation sanguine ont été conçus et fabriqués. Nous avons soumis des cellules provenant de tumeurs primaires du sein dans des situations de confinement périodiques à l'intérieur de ces canaux microfluidiques en utilisant un système de contrôle de flux. Nous avons étudiés l'impact des déformations induites par les constrictions des canaux microfluidiques sur l'expression génétique des marqueurs EMT, la morphologie ainsi que la dynamique des changements morphologiques. Nous montrons que ces paramètres cellulaires sont touchés par la déformation mécanique imposée sous flux,

suggérant que l'étape de circulation des cellules tumorales dans le sang a un rôle important dans la capacité de celles-ci à produire des métastases.

Mots clefs: microfluidiques, systèmes biomimétiques, cancer, métastases, cellules tumorales circulantes, phénotypage mécanique, imagerie, expression génétiques

---

90% of cancer mortality arises from metastases, due to cells that a) escape from a primary tumour, b) circulate in the blood as circulating tumour cells (CTCs), c) leave blood vessels and d) nest in distant organs. The processes by which CTCs invade distant organs and remodel their environment to create a “micro-metastatic niche” - the eventual triggering of a proliferation leading to a macroscopic metastases - are poorly known, mostly because of a lack of experimental models. These events are rare. They occur in the body at unknown places and on a microscopic scale.

The loss of cell adhesion of tumour cells detaching from the primary tumour tissues will undergo a transformation phenomenon known as epithelial-to-mesenchymal transition (EMT) leading to the loss of epithelial characteristics with different expression patterns of EMT protein markers and transcriptional factors (E-cadherin, N-cadherin, Vimentin, Snail1/2, Twist1/2, ZEB1/2, β-catenin and MMP-9). The changes in mechanical and physical properties of interacting cells during morphological and malignant transformation are investigated and their quantifications measured.

Here, microfluidic models containing mechanical constrictions in order to mimic the blood microcirculation have been designed and fabricated. Metastatic breast cancer cells are subjected and confined to the microfluidic channels using a flow control system. These cells are circulated under optimal culture conditions, and monitored in the channels for the observance of biophysical occurrences from continuous mechanical cellular deformations. The biophysical effects of circulation and confinement on tumour cell morphogenesis will be investigated.

Keywords: microfluidics, organ-on-a-chip, cancer, metastases, circulating tumour cells, mechanical phenotyping, imaging, gene expression

DEDICATION, PREFACE AND ACKNOWLEDGEMENT

Where I was before was failure to communicate. But today, I feel a very strong urge to get it off my chest. I have always depended on the kindness of strangers. Through this search for random graciousness, I have lost sight of what is paramount. Those who are dear, who come where I come from, who will never let me down, became victims of my selfish need for something more. However long it may be, it changes you from within involuntarily, in ways that are unfathomable. For me, it sure does feel like now, and I am grateful for the time I have during this moment of realisation to reach out to everyone whom I have crossed paths with. Most importantly, to my family and friends in Singapore, and to souls who consider me a friend. Thank you for the precious occasions you have shared with me.

I always feel like I never managed to stress enough how grateful I am. Since I began my new life in France, I have been blessed with all the beautiful people and things amongst many other great beings. I am not very good with words. I wish I were eloquent enough to express the gratitude I feel to every unique individual that has inspired my life. I wish I could have been more aggressive when given the time. To my family and friends in Bois Le Roi/Fontainebleau/Melun, thank you for your endless affections and generosity. To my friends and colleagues in Paris, thank you for brightening up my days. To my thesis supervisors and tutors, thank you for your constructive criticisms and moral support. Thank you very much, from the bottom of my heart for being there during my life changing moments.

To my sun and stars, Etienne, after almost a decade, and who have truly seen my struggles, thank you for still being here. Thank you for everything.

To my mother and sisters, thank you for my life. Living away from you has only proven that closeness has nothing to do with distance as it has caused us to have more intentional relationships than we might have had otherwise. I cannot thank you enough.

In loving memory of my father; without whom none of this would be possible.

TABLE OF CONTENTS

LIST OF ABBREVIATIONS

AFM - Atomic Force Microscopy

ANOVA - Analysis Of Variance

ARDS - Acute Respiratory Distress Syndrome

bHLH - Basic Helix-Loop-Helix

BSA - Bovine Serum Albumin

CSC - Cancer Stem Cells

CTC - Circulating Tumour Cell

DDR - DNA Damage Response

DMEM - Dulbecco's Modified Eagle's Medium

DMSO - Dimethyl Sulfoxide

DSB - Double-Strand Breaks

ECM - Extracellular Matrix

EMT - Epithelial-to-Mesenchymal Transition

EpCAM - Epithelial Cell Adhesion Molecule

FBS - Foetal Bovine Serum

FDR - False Discovery Rate

GC - Guanime-Cytosime Content

IF - Immunofluorescence

IF - Intermediate Filament

IPA - Isopropyl Alcohol

MDCK - Madin-Darby canine kidney

MET - Mesenchymal-to-Epithelial Transition

MIQE - Minimum Information for Publication of Quantitative Real-Time PCR Experiments

NC - Nuclear to Cytoplasmic

NTC - No Template Control

PBS - Phosphate-Buffered Saline

PDMS - Polydimethylsiloxane

PFA - Paraformaldehyde

qPCR – Quantitative Real-Time PCR

RCF - Relative Centrifugal Force

ROI - Regions Of Interest

RT - Reverse Transcription

RT-PCR - Reverse Transcription PCR

TF - Transcription Factors

UV - Ultra-violet

ZEB - Zinc-finger E-box-Binding

CHAPTER ONE: GENERAL INTRODUCTION

1.1 Cancer Biology

1.2 Microcirculation in Cancer Metastasis

1.3 *In Vitro* Approaches to Study the Biophysics of Cancer Progression

1.4 Overview of Research Thesis

1.1 Cancer Biology

Carcinogenesis is a multistage process of cancer formation whereby it simplistically illustrates the transformation of normal cells to cancer cells in three major stages.[1] The first stage involves aberrant genetic mutations within normal cells for tumour initiation. The subsequent stage exploits the altered genetic expressions through the interactions of receptors for tumour promotion. The daunting, final stage associates genomic instability with malignancy for tumour progression.

Almost two decades ago, Hanahan and Weinberg characterised distinct features of cancer that they deemed fundamental for the assumption of a malignant phenotype, including replicative immortality, evasion of growth suppressors, evasion of apoptosis, stimulation of angiogenesis, stimulation of proliferation, invasion and metastasis.[2] This has led to an influx of modification and expansion of the proposed hallmarks in cancer research;[3] genome instability and metastasis are two that persist.[4–6]

Metastasis plays the deadly villain in large cases of human cancers, yet therapies that have been developed to date are still not very convincing in targeting solely this highly clinically relevant process.[7] The metastatic cascade eloquently demonstrates the completion of a complex succession of cell-biological events that include local invasion, intravasation, survival in the circulation, arrest at a distant organ site, extravasation and colonisation.[6] In the following Figure 1, the metastatic cascade illustrates the clinically detectable metastases as a representation of its end products.[8]

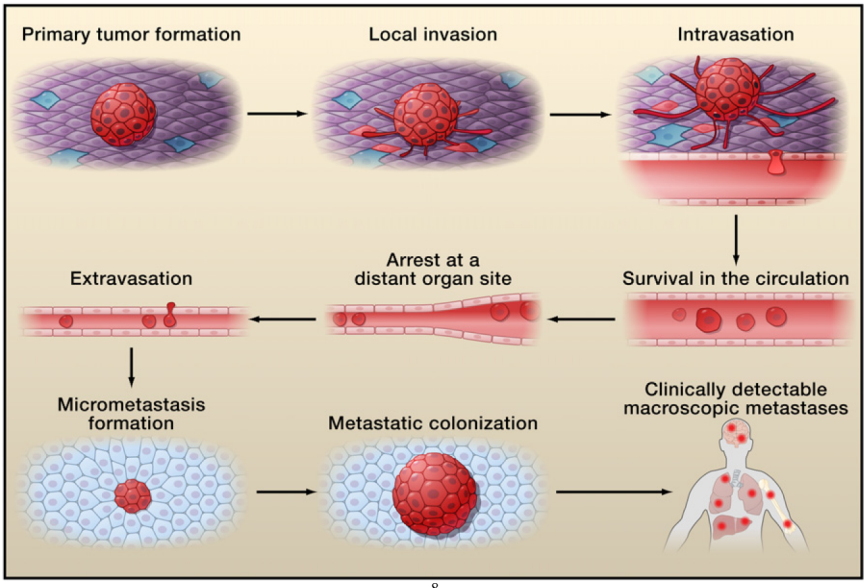

Figure 1 | The Invasion-Metastasis Cascade.[8]

Very little is known about how metastatic cancer cells arrest and adhere to the endothelium of small capillaries, and leave the blood stream by breaching through the vascular wall and squeezing their nucleus. Thus, although metastasis is the leading cause of cancer-related death, the main mechanism enabling this process remains to be elucidated.

The "seed and soil" hypothesis that was first coined by Stephen Paget in 1889, stated that the organ-preference patterns of tumour metastasis are the product of favourable interactions between metastatic tumour cells (the "seed") and their organ microenvironment (the "soil"), in which metastases resulted only when the appropriate seed was implanted in its suitable soil.[9] Well over a century now, an extensive body of clinical data and experimental research has confirmed Paget's original "seed and soil" hypothesis.[10–12] In spite of its allurement, the "seed and soil" hypothesis did not float by without criticisms and oppositions with notable arguments toward a "mechanical" hypothesis, relating the occurring patterns of tumour metastases with the sites' optimal flow patterns.[13] This hypothesis asserts that after tumour cells intravasate, they follow the circulatory drainage and arrest non-specifically in the first organ they encounter. An example of a tumour metastasis pattern based on the "mechanical"

hypothesis is commonly observed when tumours arising from the gastrointestinal tract metastasise in the liver due to the close proximity of both organs and the exclusive sharing of vascular connection through the hepatic portal system.[14] Nonetheless, it has never been mentioned nor contested that both "seed and soil" and "mechanical" hypotheses are mutually exclusive. Therefore, the extent to which either mechanism is operational depends on the tumour under investigation.

As tumour dissemination is one of the preceding processes to metastatic colonies and its process primarily occurs through the blood circulation, it is without doubt that circulating tumour cells are targets of interest and promising biomarkers for various clinical applications including screening, prognosis and monitoring of drug responses.[15–18] Circulating tumour cells, most commonly known as CTCs are cells that have shed into the cardiovascular or lymphatic system from the primary tumour and are transported around the body in the circulation, hence representing an intermediate stage in metastatic dissemination.[18] Since the turn of the millennium, tremendous efforts have been poured into the developments of various methods and devices based on immuno-affinity and biophysical properties to enrich and capture CTCs in blood samples for the extraction of information that may be able to detect cancer early, determine its aggressiveness, monitor and guide therapy.[19–22] Analyses of CTCs may provide a liquid real-time biopsy as an alternative for primary diagnosis of tumours that are inaccessible or not easy to biopsy.[23] Contemporary approaches to capture CTCs are based mainly on 1) antibody-antigen interactions, which rely on a single or a combination of antibodies and 2) cell morphological and mechanical features, which rely on size and deformability.[24,25] However, CTC enrichment technologies that rely on immuno-affinity properties through positive selection of the surface protein expression, such as the epithelial cell adhesion molecule (EpCAM), to discern CTCs from the surrounding

haematopoietic cells, are susceptible to miscounting.[26] This is particularly due to the nature and aspect of the biology of tumour dissemination.[26] On the other hand, CTC enrichment technologies that rely on biophysical properties are susceptible to the overlapping of size and density between CTCs and the surrounding haematopoietic cells.[27,28] Hence, they are unable to overcome the recovery/purity trade-off.[27,28]

The pertinent aspect of the biology of tumour dissemination refers to the observation of aggressive tumour cells that undergo extensive molecular changes, which enhance intravasation and survival in the blood circulation through the process called epithelial-to-mesenchymal transition.[29] The pioneering work of Elizabeth Hay led to observations of epithelial cells that could down-regulate epithelial characteristics and acquire mesenchymal characteristics through changes seen in the primitive streak of chick embryos.[30] Hay's findings of this differentiation process that was initially described as epithelial-to-mesenchymal transformation has now been commonly termed as epithelial-to-mesenchymal transition (EMT) to accentuate its transient nature; mesenchymal-to-epithelial transition (MET) describes the reverse process.[31]

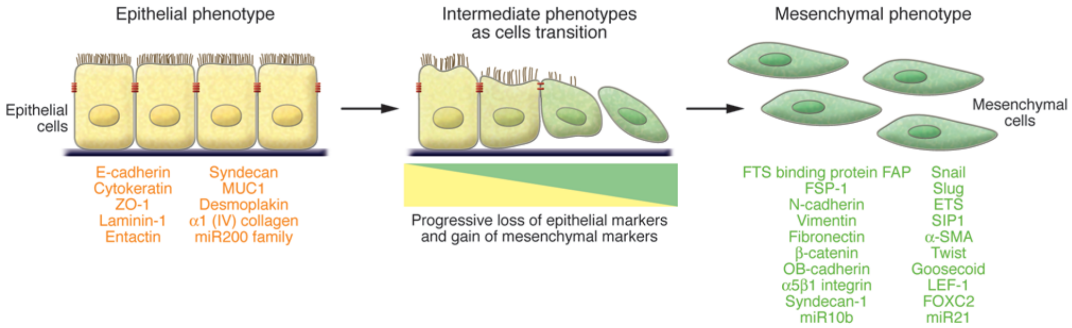

Figure 2 | EMT.[32]

The above Figure 2 portrays the essential markers commonly applied in EMT studies to understand the programming of EMT and its process: it involves a functional transition of

polarised epithelial cells, which are associated with disruptions of intercellular adhesion and apico-basal polarity resulting in the loss of epithelial features and the gain of mesenchymal morphological phenotype.[32] In tumour progression, such feature acquisition of mesenchymal phenotype enhances motility, migration and invasion into the bloodstream as depicted in the following Figure 3.[33]

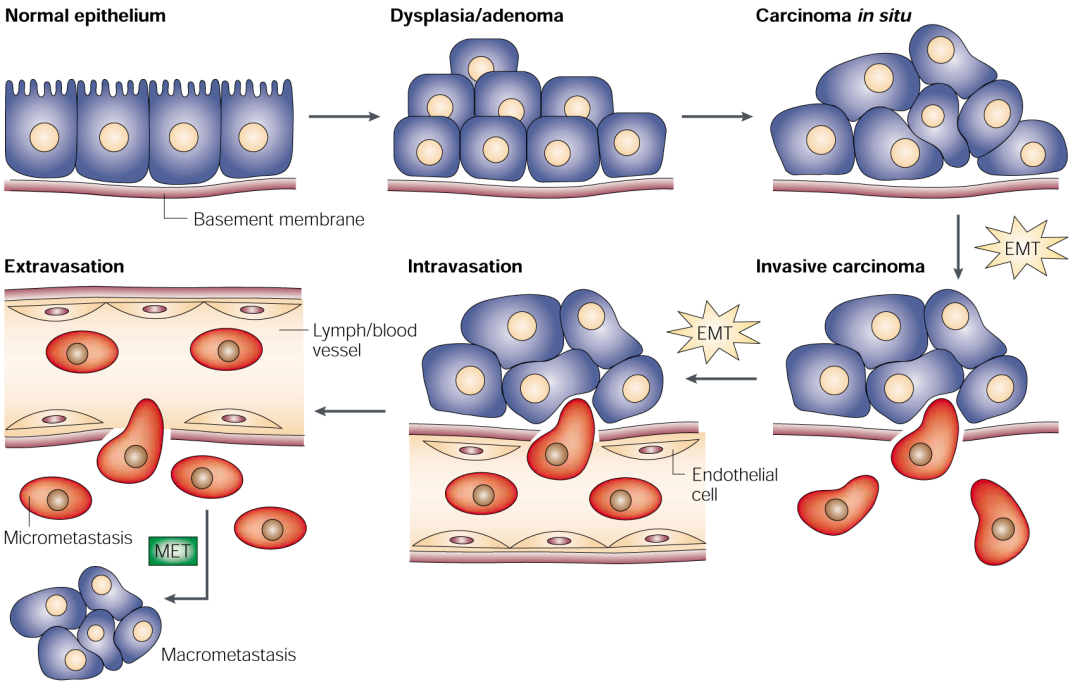

Figure 3 | Sites of EMT and MET in the emergence and progression of carcinoma.[33]

The maintenance of the mesenchymal phenotype such as up-regulation of vimentin, down-regulation of E-cadherin and EpCAM expressions, involves widespread cellular reprogramming by the activation of master regulators including transcription factors such as SNAIL, TWIST and zinc-finger E-box-binding (ZEB), and transforming growth factor, TGF-β.[33,34] These mesenchymal cells actively migrate along while remodelling the surrounding tissue either as single or as clusters, and exhibiting an increase in self-renewal capacity, stem cell-like characteristics and heterogeneous epithelial and mesenchymal phenotypes.[35,36] Due to their transient nature, the disseminated cells can establish micrometastases through the reverse process called MET.[37] Antecedently, studies in cancer biology pertaining the

importance of EMT in tumour progression were largely executed within the theoretical framework built on observations performed *in vitro*.[38] Therefore, the evidence supporting the epithelial and mesenchymal plasticity *in vivo* is highly debated.[38] The pathologic evidence of EMT in human cancer tissue samples has not yet been well established on the grounds that tissue samples obtained from human tumours were extracted at varying time points of different and sometimes unknown metastatic origins, causing it arduous to demonstrate the applicability of EMT in tumour progression.[39] The tissues extracted from these sites might not have undergone EMT yet or they might have already undergone MET.[40] Moreover, as briefly aforementioned, the current technology used to determine the role of EMT during *in vivo* dissemination was principally dependable on the detection of the expression of epithelial markers of CTCs resulting in a dubious representation of metastases.[41]

As CTCs resulted from the detachment of cells from the primary tumour into the bloodstream through the induction of EMT, they also can express stem cell properties.[29] Due to the phenotypic instability of CTCs, the prevailing model of metastasis has led to the discovery of cancer progenitor cells or cancer stem cells (CSCs), a subset of cells bearing the essentials of migratory, proliferative and dissemination potential of a tumour.[42] This suggests that the global characterisation of a tumour may be an inadequate representation of tumour cells to be targeted and may only lead to those bearing the lowest risk for patient outcome.[43] This is why in the last decade intense interest for CTCs has been booming.[44] However, they are still an elusive biomarker particularly in early stages due to their extreme rarity and phenotypic instability.[45] The conditions in the bloodstream are harsh, in which CTCs have to brace through haemodynamic forces and compete with billions of other cells in order to survive before extravasating.[26,46] Of the phases in the metastatic cascade, survival in the circulation has been somewhat a neglected child only because monitoring and visualising the events of

tumour cells circulating in the bloodstream *in vivo* has biological, clinical and technological limitations, and recapitulating such events and minute structures *in vitro* is highly intricate.[47] Henceforth, studying this process is highly needed.

1.2 Microcirculation in Cancer Metastasis

Following the transformation from *in situ* to invasive carcinoma behaviour, the next stage essential in the metastatic cascade involves the entry of tumour cells into the general circulation, a process called intravasation.[4] The rate of tumour cell escaping into the circulation is controlled by a number of factors, namely tumour vascularity, number of migrating tumour cells, anatomical factors including the structure of the basement membrane in the tumour capillary bed, and the specific properties of tumour cells.[48] Once in the circulation, tumour cells must successfully evade host defences, survive the trauma of fluid flow, and arrest in small vessels.[49] The endothelium is the innermost lining of all blood vessels that is normally biocompatible with the circulating blood.[50] Blood cells and plasma proteins do not adhere to its surface unless the endothelium is injured or perturbed causing the pathological occurrence of blood vessel wall interactions.[50]

In normal tissue, the microvascular network is responsible for the flow of blood, nutrients, hormones, oxygen and other gases to and from cells for the maintenance of homeostasis.[51] This has been generally understood as the microcirculation that consists of complex structures of diverging tree of arterioles that feeds the capillaries, which in turn drain into a converging tree of venules.[52] These structures have diameters ranging from a few hundred micrometres down to a few micrometres.[52] Thiriet's chapter on the physiology of microcirculation summarised the general structure of the endothelium.[53] Endothelial cells cover the entire surface area of the microvascular network as a single cell layer. They are approximately 20 x 50 μm in area and 6 to 8 μm in thickness. The physical properties of the endothelial cell monolayer differ depending upon the area within the microvascular network. The endothelium is the thickest in the aorta and the thinnest in the capillaries. Most endothelial cell monolayers are continuous. For instance, this is the case in the arteries, veins,

and capillaries of muscles. However, they are fenestrated in the capillaries of the viscera, the internal organs of the body. The endothelial cells in arteries and veins align longitudinally according to the direction of blood flow. Where the blood flow is turbulent, e.g. at the orifices and bifurcations of blood vessels, the endothelial cells in the capillary are more polygonal in shape without any distinct longitudinal orientation. In the following Figure 4, Pries and Secomb visualised the microvascular structure in rat mesentery that illustrated the highly heterogeneous organisation of the microcirculation.[54]

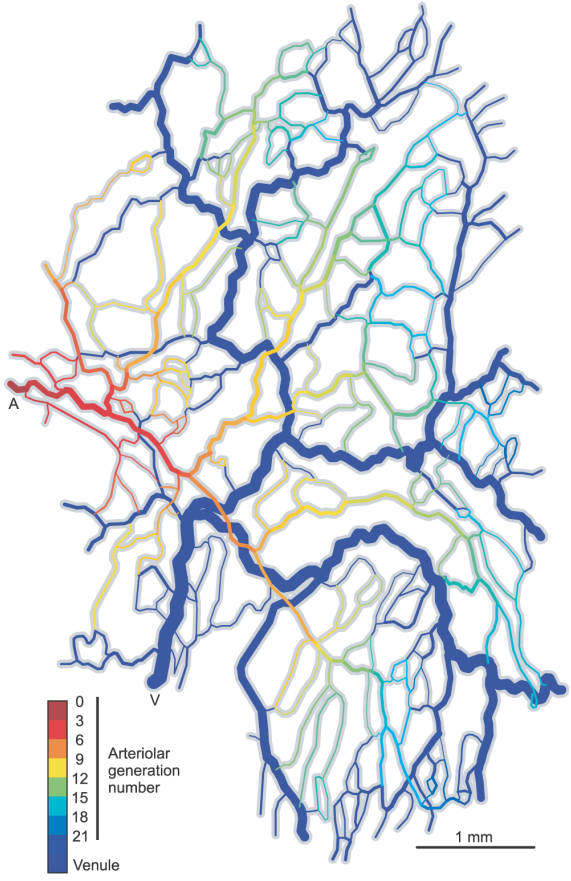

Figure 4 | Computer-generated image of a microvascular network in rat mesentery, illustrating the characteristic structural heterogeneity of the microcirculation. The main feeding arteriole is labelled A and the main draining venule is labelled V. Generation numbers of terminal branches (capillaries) range from 3 to 21 in this network.[54]

This heterogeneity has important effects on the functional behaviour of the microcirculation because the arterioles, capillaries and venules cannot be regarded as a set of equivalent vessels.[55] Thus, circulating and endothelial cells experience widely varying haemodynamic

flow patterns and functional conditions.[55] In all types of cells present in the microcirculation, these mechanical forces in the microenvironment are translated into biochemical signals in a process called mechanotransduction.[56] Thus, mechanical forces direct cell behaviour including motility, proliferation, and differentiation, and become important in physiological processes such as development and wound healing.[57]

In cancer metastasis, the effects of geometric heterogeneity of the microcirculation as well as mutations and modifications that interfere with normal mechanotransduction can lead to aberrant cell behaviour and disease.[58] Notably, it should be emphasised that the major proportion of endothelial cells is found within the capillary bed where cancer-endothelial cell interactions preferentially occur.[59] Following the events of intravasation, the circulatory path of CTCs continued to be influenced by a number of physical and mechanical parameters including the pattern of blood flow, the diameter of the blood vessels and the complex interplay between shear flow and intercellular adhesion that leads to cell arrest.[60] Such mechanical cell arrest is illustrated in Figure 5 where a CTC transports along a microvascular channel with the haemodynamic flow force and gets arrested as it approaches a blood vessel, whose diameter (d) is smaller than that of the tumour cell. Furthermore, recent research work by Follain and colleagues elegantly illustrated the manipulations of blood flow forces in driving the arrest and extravasation of CTCs using the zebrafish embryo model.[61] This highlights the importance of physical and mechanical effects in influencing the survival path of CTCs following intravasation.

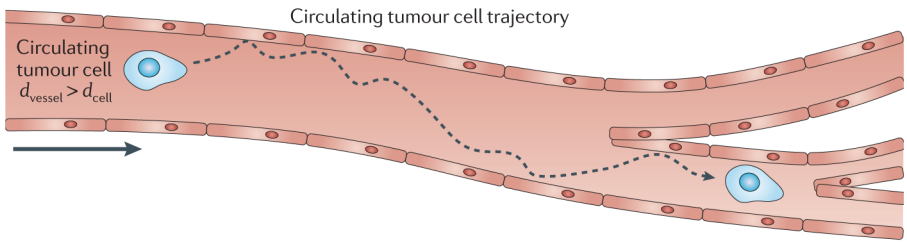

Figure 5 | Arrest of circulating tumour cells.[60]

Reasonable amount of *in vitro* evidence to date suggests that tumour extravasation and metastasis is a result of (1) blood circulation patterns (directions) and origins of CTCs,[62,63] (2) mechanical trapping of CTCs due to physical occlusion,[64,65] and (3) optimal blood flow patterns (haemodynamic forces).[66–68] Overall, while the impact of biomechanics on tumour growth and invasion are mechanistically relatively well understood, the molecular mechanisms driving survival in the circulation, arrest, and successful extravasation of CTCs still remain to be elucidated. It appears that depending upon the anatomical location, the blood flow patterns, the mechanical constraints, the state of endothelial cell integrity, and the specific enzymatic and adhesion receptors of different tumour cells, some tumour cells will be able to arrest at specific sites of the vasculature while others will not. Hence, microcirculation is an important physiological system for the up- and down-regulation of metastasis-promoting mechanisms; and its physical and mechanical features should be translated into biophysical tools to explore molecular signatures and pathways that have been overlooked; or are difficult to assess by traditional biological methods.

1.3 *In Vitro* Approaches to Study the Biophysics of Cancer Progression

Since the early 2000s, one of the rapidly flourishing fields of research is uncovering the changes in the biomechanical and biophysical properties within cells and their external structures.[69] Principally, this research focuses on how these changes influence and are influenced by the onset and progression of human diseases particularly in cancer.[69] From then on, *in vitro* approaches applying biophysical techniques including membrane stretching, atomic force microscopy (AFM), optical traps, and micropipette aspiration have shown that abnormalities in the elastic properties of cells are associated with disease pathogenesis and tumour progression.[70] A widely utilised model to study the invasion or migration of cancer cells *in vitro* is based on the Boyden chamber system, which is relatively simple to operate.[71] Nonetheless, it is restricted in investigating the complex interactions between tumour cells and the endothelium that take place during metastasis due to its lack of the basic components of blood vessels.[72] Furthermore, limitations of the progress in this direction have been mostly attributed to the lack of *in vivo* models to study the fate of cancer cells after intravasation.[73] However, current technological advancements and developments notably microfluidic tools, now offer the means to overcome the above limitations by proposing *in vitro* models of these phenomena.[74] In this research thesis, the utilisation of an organ-on-a-chip approach will be proposed to shed new light on the fate of cancer cells in the circulation.

Organ-on-a-chip is a field of intense interest, whose current systems are still often relatively limited regarding to the level of accuracy of cellular organisation.[75] Nonetheless, as the field is rapidly progressing, several research groups have developed elaborate mimics of organs including a model lung[76] and a model intestine comprising a reconstituted epithelial layer on

a membrane that separated the air compartment from the liquid compartment and allowed the introduction of the peristaltic motion.[77] There have also been studies on the reconstitution of the microvasculature in microfluidic systems using the strong self-organising properties of endothelial cells. One of these studies involved the development of a model liver sinusoid from hepatocytes, but the spatial architecture was still far from the physiological one.[78] Later, the spatial organisation was improved upon through the establishments of open channels with well-defined architectures covered with a confluent monolayer of endothelial cells; these architectures were used to study angiogenesis and thrombosis following inflammatory signalling.[79] However, these systems do not involve the extracellular matrix (ECM) and thus, are not well adapted to model the events leading up to extravasation. Although rather sparse, the progress of *in vitro* experimental models for the study of extravasation has been quite promising. An interesting work by Chen and colleagues used a spontaneously reconstituted *in vitro* microvascular network, which permitted studies on extravasation using MDA-MB-231, HT-1080 and MCF-10A cell lines.[80] Jeon and co-authors developed another type of architecture, in which a rectangular model vessel is covered with a reconstituted endothelium that was in complete contact with a hydrogel.[81] Then, Riahi's group improved upon this design, perfusing the hydrogel with chemokines, in order to investigate the hypothesis that organ-specific extravasation could be driven by chemical signalling as illustrated in the following Figure 6.[82]

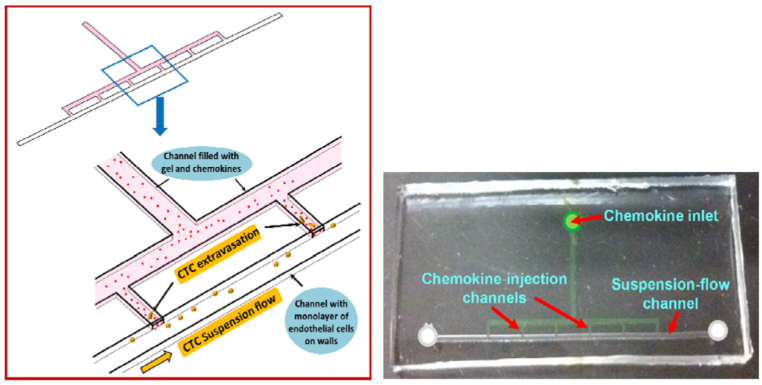

Figure 6 | Device design and fabrication: (a) Schematic illustration of the device structure and operation, and (b) an image of a fabricated microfluidic device.[82]

Notwithstanding, the lack of microfluidic guidance of these vasculature models led to a random porous organisation that lacked the possibilities to study the effect of fluid flow stress or mechanical constraints on CTC arrest and extravasation. Therefore, there is a need to address how these physical and structural changes alter single-cell mechanical responses, including elastic and viscoelastic deformation characteristics; and how changes in cellular deformability and shape affect the metastatic process.

Pioneering work by Preira and colleagues investigated the role of adhesion, friction and deformability in the pathological arrest of leukocytes in the blood microcirculation of the lungs, which is the triggering event of the acute respiratory distress syndrome (ARDS) by devising a microfluidic system.[83] In the following Figure 7, they mimicked the multiple branches and constrictions of the blood microvasculature network by fabricating series of interconnected crenelled 4 µm-wide constrictions with symmetric and asymmetric geometries to study the behaviour of cells.[83] They showed that the cell transit of compliant cells was disturbed in asymmetric geometries but the global transit times were still comparable to the transit in symmetric geometries.[83] However, the transit time was drastically disturbed with stiff cells in asymmetric geometries.[83]

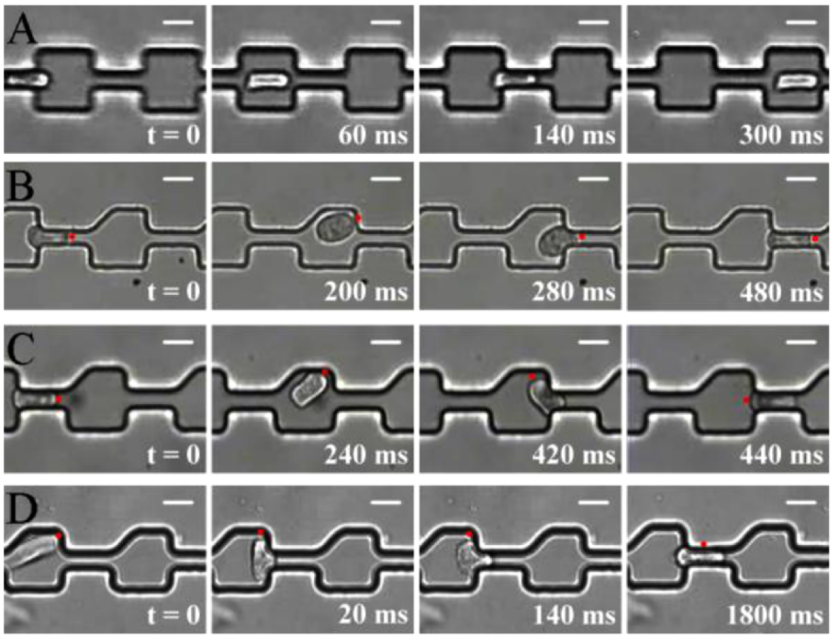

Figure 7 | The effect of symmetric and asymmetric geometries on the transit time of THP-1 white blood cells. (A-C) Correspond to compliant cells and (D) to stiff cells.[83]

Preira et al. also designed a new artificial micro vessel with porous walls to mimic the porosity of real blood vessels; allowing the study of leukocyte extravasation, transmigration and metastasis.[84] They further analysed the role of the hydrodynamic stress on the migration of leukocytes at the inner surface of blood vessels and showed how normal T-lymphocyte crawl upstream in opposition to the exerted force.[85]

Since then and just within the last five years, microfluidic systems mimicking fluid flow stress and mechanical constraints as experienced by CTCs in the microcirculation blossomed tremendously.

Rathod et al. developed a microfluidic system that combined substrate rigidity and flow-induced shear stress.[86] These authors showed that there was a positive correlation between either incidence and the cell surface area of HUVEC cells; the stiffer the substrate and/or higher the shear stress, the larger the surface area.[86] Such cell mechanical response to fluid flow was later observed by Follain et al. in zebrafish embryo when haemodynamic forces

regulated the remodelling of endothelial cells for extravasation.[61] They further demonstrated that through manipulations of flow forces in order to encourage CTCs to adhere better to the endothelium, successful arrest and extravasation of CTCs were observed.[61] They also observed early arrests of CTCs when flow dynamics were decreased and observed promotion of extravasation when flow dynamics were increased.[61] Regmi et al. on the other hand reported that 90% of tumour cells circulated in a microfluidic system underwent necrosis when exposed to shear stresses comparable with that occurring in human arteries during periods of intensive exercise and the remaining surviving cells underwent apoptosis even at post-circulation.[87] This suggests the existence of a threshold in modulating fluid shear stress as a possible mechanical inhibitor and promoter of CTC arrest and extravasation. At the same time, this opened up another view of fluid shear stress as a physical deterrent of CTC metastasis, however these results have to be correlated with occurrences using *in vivo* models.

Chivukula et al. investigated the impact of fluid shear stress on the mechanical properties of suspended cancer cells that were passed through a 30 gauge needle ten times.[88] The Young's moduli of these cells were determined using the micropipette aspiration technique and they found that transformed prostate cancer (PC-3) cells became less stiff than non-transformed PC-3; demonstrating the acquired deformability of cancer cells.[88] This acquired deformability of cancer cells was demonstrated by Au et al. using CTC clusters in both microfluidic and zebrafish embryo models.[36] They observed that CTC clusters of epithelial and mesenchymal phenotypes were shown to migrate in a similar fashion through narrow constrictions by cellular reorganisation into a single file that resulted in the reduction of transit resistance of a channel with mechanical constraints.[36] However, Shaw Bagnall et al. reported that increased CTC deformability was not always necessary in the metastatic process.[89] First, they

demonstrated in an *in vivo* model that metastatic colonies were formed in mice after being injected with murine mammary carcinoma cells in their tail veins.[89] More interestingly, they then observed the tumour cells that had shed into the circulation from these metastatic colonies were not especially more deformable than the initially injected population of tumour cells.[89] Using a microfluidic system, they also found that regardless of cellular deformability, human prostate CTCs exhibited a transit time similar to that of blood cells, when crossing microfluidic constrictions; this is most likely due to the small size of CTCs.[89] This absence of correlation between cellular deformability and metastatic potential does not portray to contradict current knowledge but to illustrate the complexity of cancer metastasis, in which another unknown mechanism could possibly be at play. Additionally, these experimental studies still have not attempted to elucidate the underlying molecular mechanisms governing CTC arrest and extravasation in order to make the association of genetic with mechanical factors.

Simultaneously, multiple reports within the last five years have also showed that mechanical constraints can induce nuclear deformability[90,91], nuclear envelope rupture and DNA damage.[92,93] It had already been hypothesised that modifications in nuclear structure and composition may promote cancer cell invasion and metastasis.[5] Davidson et al. observed that nuclei of fibroblasts deformed in order to migrate through narrow constrictions and that reduced expression of the nuclear envelope protein, lamin A/C modulated nuclear stiffness by impairing the physical coupling between the actin cytoskeleton and nucleus, which in turn promoted the passage of these fibroblasts through the narrow constrictions.[90]

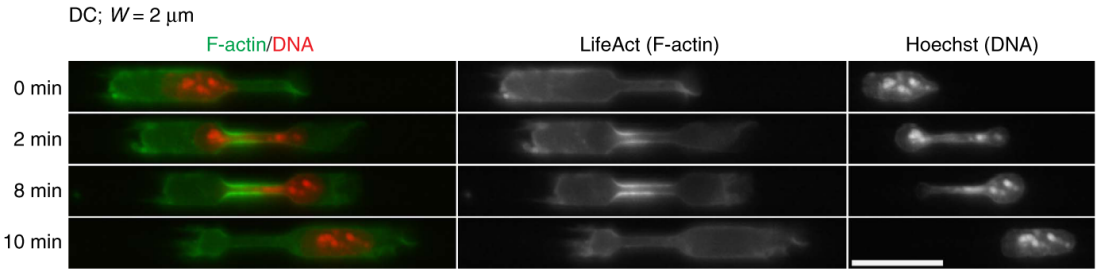

Figure 8 | Sequential images of a representative LifeAct-GFP (green) expressing dendritic cell stained with Hoechst (red) passing a 2 µm-wide constriction. Scale bar, 20 µm.[91]

In the above Figure 8, Thiam et al. further observed the nuclear deformation of dendritic cells migrating through narrow constrictions, and reported that Arp2/3 complex was required to drive actin polymerisation in deforming the nucleus for successful clearance of cell passage.[91] They showed that the positioning of the nucleus (at the entry of constriction) was also crucial for successful clearance of cell passage regardless of the presence of actin polymerisation.[91] In the same year, a couple of studies by Raab et al. and Denais et al. explained the role of DNA repair machinery in surviving cells after migration through narrow constrictions.[92,93] They found that endosomal sorting complex required for transport III (ESCRT-III) was required to repair nuclear envelope rupture and DNA damage caused by nuclear deformation.[92,93] A recent study by Irianto et al. reported that in U2OS osteosarcoma cells, migration through narrow constrictions also led to lasting genomic instability that could be associated with heritable changes.[94]

The aforementioned described the difference in nucleus behaviour depending on the cell type and process, which leads to the question: what are the repercussions of these large nuclear deformations during migration on gene expressions? These recent findings have opened up a new level of complexity in understanding the role of nuclear dynamics during cell migration. Therefore, further investigations about how nuclear squeezing without regulates gene expression have to be scrutinised. Moreover, majority of *in vitro* studies to date had been revolving around the process of intravasation through spontaneous cell migration on adhesive

surfaces. Despite the current developments of microfluidic devices in demonstrating great potential to fine-tune specific physical, biochemical, or cellular signals to investigate metastasis, their translatability to *in vivo* models still remain limited. Let alone metastatic events modelled by flow-driven cell migration mimicking the survival of CTCs in the microcirculation. It comes as no surprise that *in vitro* studies based on flow-driven cell migration in micro channels are scarce as their experimental arduousness is much more gruelling. Here, this will be ascertained.

1.4 Overview of Research Thesis

The process of tumour cell invasion and metastasis is complex, and attempts to focus on one particular aspect may neglect other aspects of the process that are equally important. Certainly, changes in adhesiveness resulting from alterations in the tumour extracellular matrix are not solely responsible for invasion and metastasis. Factors influencing the ultimate fate and localisation of disseminating tumour cells in the body include differences in the exposed cell surface antigens, cellular and secreted enzymes, other secreted products, and inflammatory and coagulative responses. The question of variation in the properties of tumour cells derived from primary and secondary lesions is complex and difficult to study as metastases have been shown to be antigenically and biochemically distinct from their primary tumours. Major differences in biological characteristics that also influence dissemination of tumour cells include the capacity of the cells to invade blood vessels and tissues; and subsequently to colonise and proliferate within specific target tissues.

Nonetheless, there is convincing evidence that 1) consistent alterations in blood flow patterns and mechanical constraints of the microcirculation accompany transformation,[13,46] 2) these alterations lead to changes in cellular and nuclear behaviours,[90–93] and 3) changes in nuclear envelope environment are critical to invasion and metastasis.[5,94]

Cellular and nuclear deformability involves the loss of adhesion and stiffness, both of which are biophysical properties and are thought to be hallmarks of EMT.[2,3,95] Particular mechanical properties of epithelial and mesenchymal cells can be unique indicators of metastatic cancer.[60] Characterisation of the biomechanical properties, such as elastic stiffness, may allow a more accurate prognosis of metastasis.[61,96–98] Furthermore, this mechanical

characterisation of the cell is important for understanding the changes in the molecular networks.

In this research thesis, the main aim is to study how circulation and constrictions can regulate gene expressions and genome integrity. Tumour cells will be circulated in microfluidic channels using a flow control system to mimic the blood flow of microcirculation. While under assisted circulation, the tumour cells will be constrained due to the presence of evenly-spaced multiple constrictions to mimic the mechanical condition in the blood capillary bed. The ways in which shear flow and mechanical constraints can promote genomic instability and metastasis, two hallmark features of cancer, will be investigated and elaborated regarding the following hypotheses.

Hypothesis 1: Fluid flow stress regulates the cellular deformability of epithelial and mesenchymal cells. To test this hypothesis, tumour cells of epithelial and mesenchymal origins will be circulated in several geometrical models consisting of 6 μm-wide constrictions and their transit time, trajectory and elongation ratios will be measured.

Hypothesis 2: Fluid flow stress and mechanical constraints regulate EMT and MET. To test this hypothesis, tumour cells of epithelial and mesenchymal origins that will have been circulated in several geometrical models consisting of 6 μm-wide constrictions will be isolated and characterised; and their gene expressions and protein levels will be measured and associated with epithelial and mesenchymal phenotypes.

The outline of this research thesis is defined as following:

First, the fabrication of the micro constrictions will be described. The assembly of a microfluidic system will illustrate the mimicry of flow dynamics and mechanical constraints as observed in the blood microcirculation. This microfluidic system will be used as a biophysical tool to characterise the circulating tumour cell mechanical phenotype.

Second, the isolation of the circulated tumour cells from the microfluidic system will be shown. Techniques of immunofluorescence will be implemented to characterise cell and nuclear morphologies. This will allow the examination of immediate effects of fluid flow stress and mechanical constraints on the circulated tumour cells.

Third, the retrieval of the circulated tumour cells from the microfluidic system for downstream molecular analysis will be depicted. Epithelial and mesenchymal genes will be used as candidate genes to analyse genetic variations within tumour cells circulated in different geometrical models.

Finally, the results obtained will be summarised and their potential relationships to metastatic outcomes will be discussed.

CHAPTER TWO: GENERAL MATERIALS AND METHODS

2.1 Work Flow

2.2 Microfabrication

2.3 Microfluidics

2.4 Cell Tissue Culture

2.5 Molecular Analysis

2.6 Immunofluorescence (IF)

2.7 Image Analysis

2.8 Statistical Analysis

2.1 Work Flow

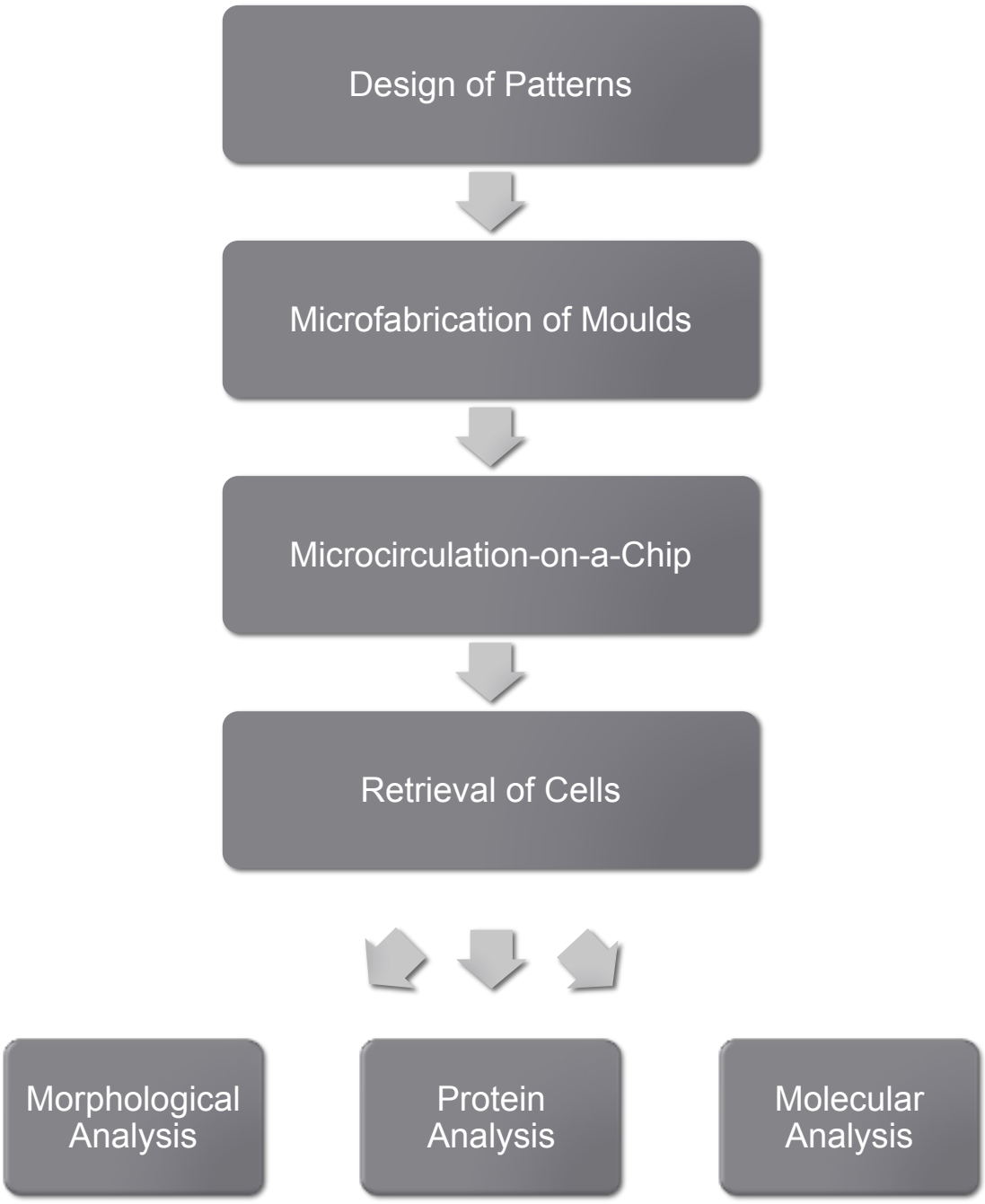

Figure 2-1 | General Work Flow of Research Thesis.

2.2 Microfabrication

Photo-Masks Design

A computer-aided design software application for two-dimensional design and drafting called QCAD was used to design different types of geometry (Figure 2-2). The total length of one geometrical channel is 420 µm. Each type of design consists of four 420 µm-long channels that are arranged in parallel. A control design without constrictions has a channel width of 26 µm. Here, a constriction is defined as having a width of 6 µm. For three types of designs containing constrictions, the length of constriction is varied. The first type contains 11 constrictions with each measuring 20 µm in length. The second type contains 7 constrictions with each measuring 40 µm in length. The third type contains 5 constrictions with each measuring 60 µm in length. The constrictions are connected with a resting chamber that is 20 µm by 26 µm in dimension. The channel height will be defined in the following section.

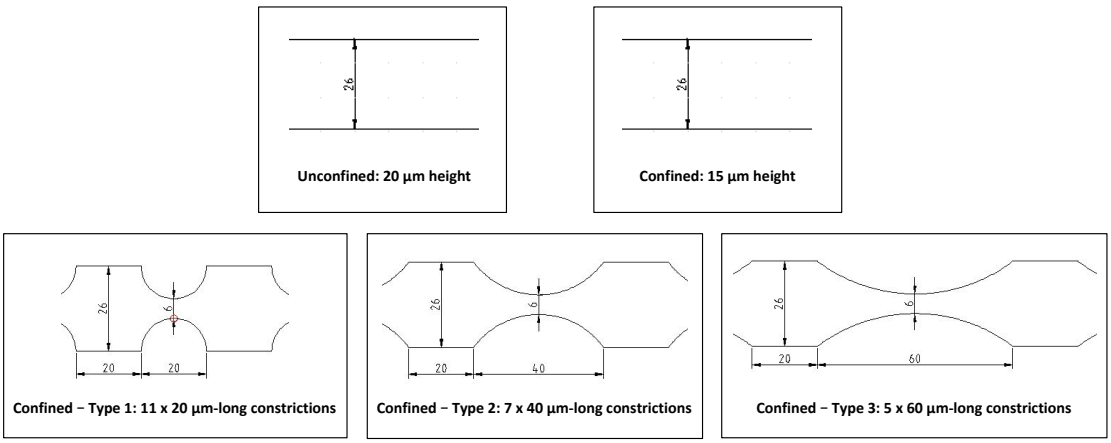

Figure 2-2 | Types of two-dimensional geometrical designs. Dimensions are in micrometres.

Optical Photolithography

These two-dimensional geometrical designs were etched onto a glass substrate with a chrome layer. The production of this chrome mask was outsourced to Selba S.A., Switzerland. From this chrome mask, a silicon master mould was fabricated in a cleanroom where provisions were made to reduce particulate contamination and control other environmental parameters such as temperature, humidity and pressure. This fabrication process is summarised in the following Figure 2-3.

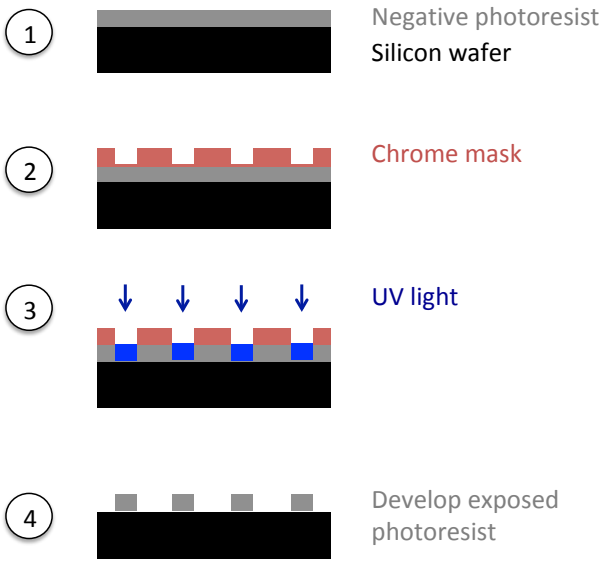

Figure 2-3 | Fabrication of a silicon master mould.

A silicon wafer was used as a substrate. A negative photoresist called SU-8 is spin-coated onto the substrate. Different types of SU-8 photoresists that are spin-coated onto substrates at different speeds will produce SU-8 photoresist films of different thickness (Figure 2-4). This thickness will define the height of structures.

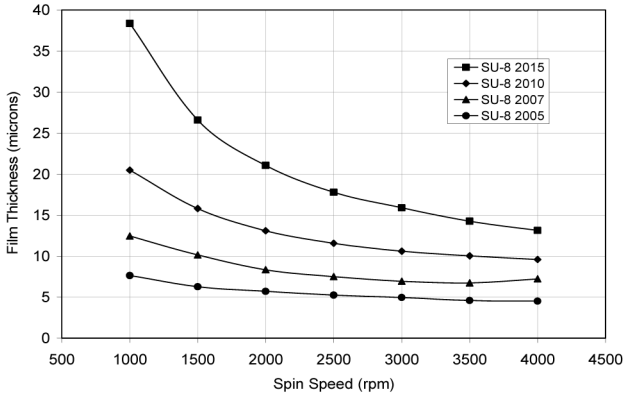

Figure 2-4 | SU-8 photoresists' spin speed versus thickness. Adapted from MicroChem, USA.

Here, SU-8 2010 photoresist was used to obtain structures with structure heights of 20 µm and 15 µm. After spin-coating the substrate with SU-8 2010 photoresist, the photoresist-coated substrate is soft baked at 95°C (Table 2-1).

Thickness (µm)	Spin-coating Time (s)	Spin-coating Speed (rpm)	Soft Bake Time (min)
20	30	1000	3.5
15	30	1500	3

Table 2-1 | Conditions for spin-coating and soft bake.

A negative photoresist is a type of photoresist in which the portion of the photoresist that is exposed to ultra-violet (UV) light becomes insoluble to the photoresist developer. This results in the unexposed portion of the photoresist to be dissolved by the photoresist developer. An optical lithography mask aligner called MJB4 (SÜSS MicroTec AG, Germany) was used to expose UV light unto the chrome mask that was aligned on the photoresist-coated substrate. The UV light exposure dosage was optimised for each of the desired thickness (Table 2-2). Post exposure bake at 95°C is carried out directly after exposure.

Thickness (µm)	Exposure Energy (mJ/cm^2)	Exposure Time (s)	Post Exposure Bake Time (min)
20	145	16	4.5
15	140	17	4

Table 2-2 | Optimal exposure dosage and post exposure bake.

The exposed photoresist was then developed in a shaking bath of photoresist developer (Table 2-3).

Thickness (µm)	Development Time (min)	Shaker Speed (rpm)
20	3.5	100
15	3	100

Table 2-3 | Development times for SU-8 developer.

After development, the developed image was rinsed with fresh developer solution for approximately 10 seconds, followed by a rinse with Isopropyl Alcohol (IPA) for another 10 seconds. Then, it was air-dried with pressurised air and hard baked for 30 minutes at 300°C. The fabrication of a silicon master mould is now complete.

Soft Lithography

From this silicon master mould, a microfluidic polydimethylsiloxane (PDMS) chip is fabricated through soft lithography. This fabrication process is summarised in the following Figure 2-5.

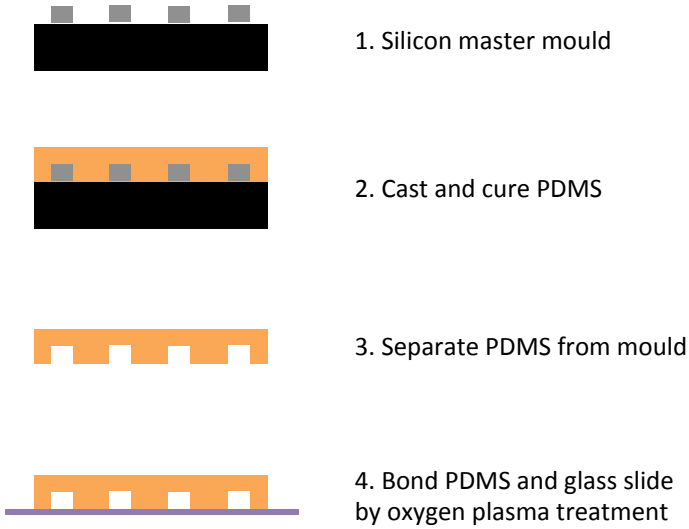

Figure 2-5 | Fabrication of a microfluidic PDMS chip.

PDMS silicon elastomer, Sylgard 184 was purchased from Dow Corning (Michigan, USA). It was mixed with a curing agent at a ratio of 9:1 and then poured over the silicon master mould. They were cured at 70°C and left to harden for 4 hours. After curing, the PDMS stamp was separated from the silicon master mould. 1.5 mm holes were punctured on the designated areas of the PDMS stamp in order to create reservoirs. Oxygen plasma treatment was performed. Conducting an oxygen plasma treatment modifies the surface of the PDMS stamp with the imprints of structures. Oxygen plasma treatment disrupts surface silicon-oxygen bonds thus creating a hydrophilic surface. When an oxygen plasma-treated glass slide is placed on the activated side of the PDMS stamp, bonds begin to reform. Once activation wears off, silicon-oxygen bonds are formed between the surface atoms of the glass and the surface atoms of the PDMS. This causes the glass slide to become permanently sealed to the PDMS stamp, thus creating a waterproof channel. From this, PDMS-bonded slides were used as chips for the microfluidic system.

2.3 Microfluidics

Experimental Set-Up of the Microfluidic System

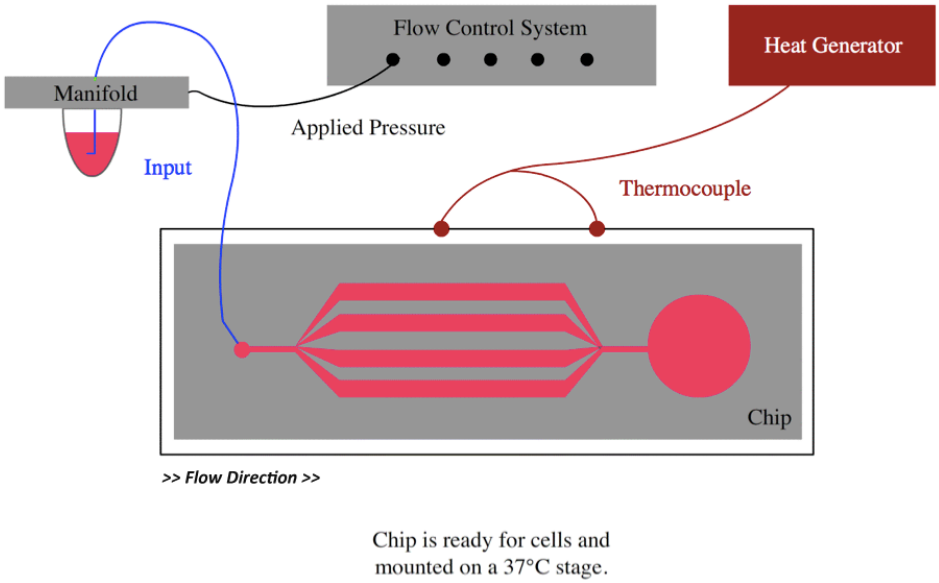

Figure 2-6 | Overall set-up of the microfluidic system.

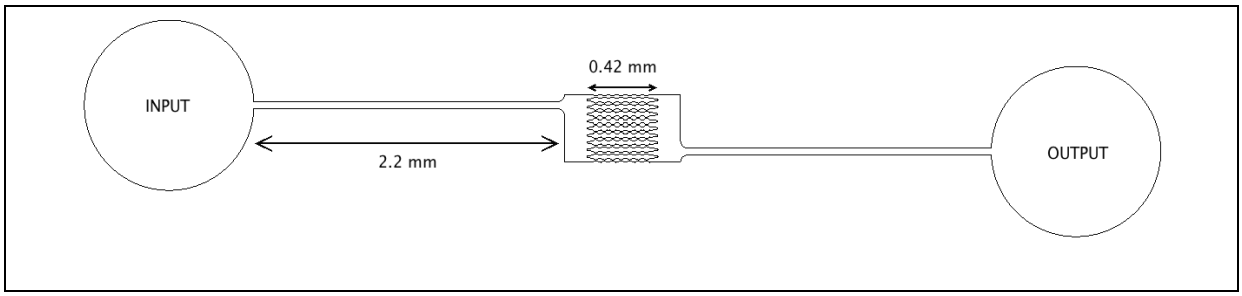

Figure 2-7 | The Diagonal Series model consists of 10-parallel channels. Each channel is 420 µm in length. The model comes with channels with different lengths of constriction geometry as illustrated in Figure 2-2. This model was used for optimisation protocols.

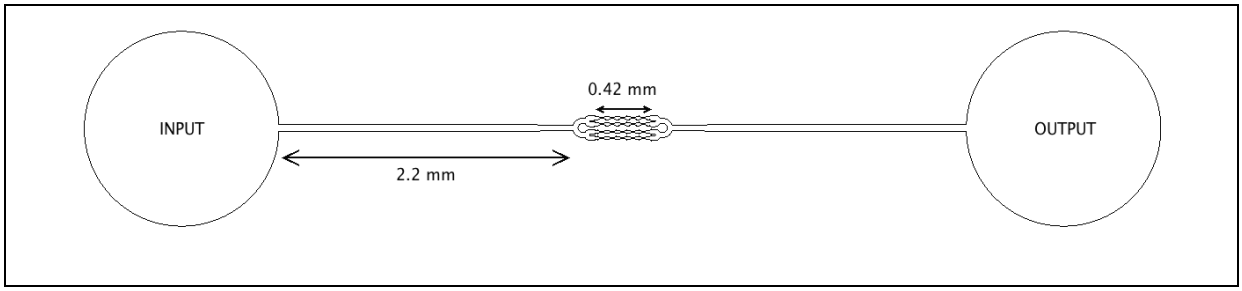

Figure 2-8 | The Bell Series model consists of 4-parallel channels. Each channel is 420 µm in length. The model comes with channels with different lengths of constriction geometry as illustrated in Figure 2-2. This model was used for final experimental protocols.

Experiments with the Microfluidic System

Based on the above Figure 2-6, all reagents and cell suspensions used during the experiments were stored in pressurised containers that were connected to the microfluidic chip through a manifold valve (Fluigent, France). An MFCS-8C Flow Controller (Fluigent, France) was used to control the pressure independently in each container to drive all reagents and cell suspensions into the microfluidic chip. A heat generator was used to warm the microfluidic device at 37°C throughout the experimental duration in order to achieve optimal culture conditions for experiments with live cells. Each microfluidic chip experiment experienced three major stages.

Stage 1: Priming of Chip

The microfluidic channels were sterilised with 70% Ethanol (EtOH) followed by a washing step with 1X Phosphate-Buffered Saline (PBS). In order to have non-adhesive surfaces, the channels were coated with 100% of 1 mg of PLL-g-PEG (Susos AG, Switzerland) solution that was dissolved in 100 mM of sodium bicarbonate ($NaHCO_3$) buffer at pH 8.5 for 1 hour.[99] The channels were washed with 1X PBS and then filled with serum-free Dulbecco's modified Eagle's medium (DMEM) with HEPES (ThermoFisher Scientific, USA).

Stage 2: Introduction of Cells into the Chip

A suspension volume of approximately 5000 cells in serum-free DMEM with HEPES was introduced into the microfluidic chip. This approximation of cell number was deemed optimal for the microfluidic models used in order to optimally observe single cell flow-

induced migration in the channels without cell clumping or channel clogging. Here, single cell flow-induced migration was recorded based on the image acquisition control of frame rate. The image acquisitions of cells crossing the micro channels of constrictions at 50 frames per second were produced using the Basler acA800-510um USB 3.0 camera (Basler AG, Germany).

Stage 3: Retrieval of Cells from the Chip

Following the introduction of cells into the microfluidic chip, the circulation of cells was allowed for 1 hour. Then, the cells were carefully retrieved from the output reservoir for two follow-up tests. The final volume of retrieved cells from one microfluidic experiment was approximately 10 µL. Hence, tremendous care had to be applied when manipulating the cell retrieval process. The first follow-up test was for molecular genetic analysis and the second follow-up test was for immunofluorescence (IF) analysis of cellular proteins.

2.4 Cell Tissue Culture

Culture Maintenance and Harvesting Procedure

3D Morphology	Cell Line	Organism	Disease	Tissue Source	Tumourigenicity	Tumour Classification
Epithelial-like	MDCK II	Dog	Normal	Kidney	No	-
Grape-like	SK-BR-3	Human	Adenocarcinoma	Metastatic Pleural Effusion	Yes	Luminal
Stellate	MDA-MB-231	Human	Adenocarcinoma	Metastatic Pleural Effusion	Yes	Basal

Table 2-4 | Characteristics of Cell Lines.

All cell lines were purchased from American Type Culture Collection (Virginia, USA). All cell culture reagents were purchased from Gibco, ThermoFisher Scientific (Massachusetts, USA). Human breast cancer cell lines: SK-BR-3 and MDA-MB-231; and epithelial Madin-Darby canine kidney (MDCK) II cells were cultured in complete Dulbecco's modified Eagle's medium (DMEM) that was supplemented with 100 U/ml aqueous penicillin, 100 mg/ml streptomycin and 10% foetal bovine serum (FBS). Cells were maintained at 37°C in a humidified atmosphere containing 5% CO^2 and harvested with TrypLE (1X). Cell dissociation was deactivated with complete media. Cells were pelleted by centrifugation at 180 x g (relative centrifugal force, RCF) for 5 minutes and then re-suspended in complete media. The cell suspensions were used only when their viability as assessed by trypan blue exclusion exceeded 95% before use.

TGFβ1 Treatment

Cell cultures were passaged and allowed to grow for 24 hours before treatment with 10 ng/mL of transforming growth factor beta 1 (TGFβ1) for 24 hours.[100,101] Control sets for TGFβ1 treatment were prepared by adding 0.1% of dimethyl sulfoxide (DMSO) for 24 hours. Cells were pelleted by centrifugation at 180 x g (relative centrifugal force, RCF) for 5 minutes and then re-suspended in complete media. The cell suspensions were used only when their viability as assessed by trypan blue exclusion exceeded 95% before use.

Trypan Blue Exclusion

Cell viability was determined and calculated as the number of viable cells divided by the total number of cells within the grids on a haemocytometer. If cells take up trypan blue, they are considered non-viable. The cell density of cell suspensions was determined using a haemocytometer. 0.1 mL of 0.4% of trypan blue solution was added to 0.1 mL of cells. The trypan blue solution and cell mixture was loaded into a haemocytometer and examined immediately under a microscope at low magnification. The number of blue staining cells and the number of total cells were counted. Cell viability should be at least 95% for healthy log-phase cultures.

$$\text{Percentage of viable cells} = \text{number of blue cells} \div \text{number of total cells} \times 100$$

2.5 Molecular Analysis

Total RNA Extraction

Total RNA extraction was performed using the ARCTURUS® PicoPure® RNA Isolation Kit (Applied Biosystems, USA). The kit was designed to recover high-quality total RNA consistently from fewer than ten cells and even from a single cell. Total RNA extraction was executed according to the following steps.

1. In a 1.5 mL micro-centrifuge tube, 50 µL of extraction buffer was added to 10 µL of cell suspensions that were retrieved from the microfluidic chip device as aforementioned.
2. The extraction buffer and cell suspension mixtures were vortexed thoroughly and incubated for 30 minutes at room temperature. The mixtures were then centrifuged at 800 x g for 2 minutes.
3. RNA purification columns were pre-conditioned by dispensing 250 µL of conditioning buffer onto the purification column filter membrane. The purification columns were incubated for 5 minutes at room temperature. The columns were then centrifuged at 16, 000 x g for 1 minute to remove the flow-through.
4. 60 µL of 70% Ethanol (EtOH) were dispensed into the cell extracts from Step 2. They were mixed by pipetting and were not centrifuged.
5. The cell extract and EtOH mixtures were into the pre-conditioned RNA purification columns from Step 3.
6. In order to bind the RNA to the column, the columns were centrifuged at 100 x g for 2 minutes and then followed by an immediate centrifugation at 16, 000 x g for 30 seconds to remove the flow-through.

7. 100 µL of Wash Buffer 1 was dispensed into the columns and then centrifuged at 8, 000 x g for 1 minute.
8. 100 µL of Wash Buffer 2 was dispensed into the columns and then centrifuged at 8, 000 x g for 1 minute.
9. 100 µL of Wash Buffer 2 was dispensed into the columns again and then centrifuged at 16, 000 x g for 2 minutes.
10. The flow-through wastes were discarded and the columns were re-centrifuged at 16, 000 x g for 1 minute to remove all traces of the wash buffers prior to the elution step.
11. The purification columns were transferred to a new 0.5 mL micro-centrifuge tube.
12. 12 µL of Elution Buffer were directly dispensed onto the membranes of the purification columns.
13. The purification columns were incubated at room temperature for 1 minute.
14. The purification columns were centrifuged at 1, 000 x g for 1 minute to distribute the Elution Buffer in the columns.
15. The purification columns were then centrifuged at 16, 000 x g for 1 minute to elute the RNA.
16. The RNA samples were used immediately for downstream analyses or stored at -80°C for future usage.

Quantification of Total RNA

Total RNA was measured using Qubit RNA reagents (Invitrogen, USA). Measurements were conducted using the Qubit 3.0 Fluorometer (Invitrogen, USA). 0.5 mL PCR tubes were used to set up the assay. 2 tubes were prepared for the standards and 1 tube was used for each sample. Qubit Working Solution was prepared by diluting the Qubit RNA reagent in the

Qubit RNA buffer at 1:200. 200 µL of Qubit Working Solution was prepared for each standard and sample. Assay tubes were prepared based on the following Table 2-5.

Volume	Standards	Samples
Working Solution	190 µL	199 µL
Standards 1 and 2	10 µL	-
Sample	-	1 µL
Total in each Assay Tube	200 µL	200 µL

Table 2-5 | Qubit RNA Assay Sample Preparation.

Assay tubes were vortexed for 3 seconds and incubated at room temperature for 2 minutes. The Qubit 3.0 Fluorometer was calibrated with the standards before the samples were measured and recorded.

Reverse Transcription PCR (RT-PCR)

All the RNA samples did not undergo more than two freeze-thaw cycles to avoid any potential nucleic acid degradation. Total RNA reverse transcription (RT) was performed using the High-Capacity cDNA Reverse Transcription Kit (Applied Biosystems, USA). The RT process is summarised in the following Table 2-6.

Procedural Overview		
1.	Prepare 2X reverse transcription Master Mix	
2.	Add RNA to reverse transcription reactions	
3.	Perform reverse transcription in a thermal cycler	
4.	Use the reverse transcription reactions (cDNA) directly for quantitative or other PCR applications	Store the reverse transcription reactions (cDNA) at: • 2°C to 6°C for short term storage • -15°C to -25°C for long term storage

Table 2-6 | Procedural Overview of cDNA Synthesis.

The components of the kit were allowed to thaw on ice. A 2X RT Master Mix was prepared based on the components listed in the following Table 2-7. The 2X RT Master Mix was mixed gently and placed on ice.

Component	Volume (µL) per Reaction
10X RT Buffer	2.0
25X dNTP Mix (100 mM)	0.8
10X RT Random Primers	2.0
MultiScribe™ Reverse Transcriptase	1.0
RNase Inhibitor	1.0
Nuclease-Free Water	3.2
Total per Reaction	10.0

Table 2-7 | 2X RT Master Mix Reaction Components.

For every RT reaction, 10 µL of 2X RT Master Mix were dispensed into a 0.5 mL PCR tube. Then, 10 µL of 30 ng of total RNA were added to each RT reaction. The RT reactions were accompanied by a RT negative control (NRT) in order to assess the amount of genomic DNA contamination during RNA preparation. The RT reaction tubes were lightly vortexed and spun before being reversed transcribed in a thermal cycler. The following Table 2-8 sets the thermal cycling conditions for reverse transcription. After reverse transcription, the cDNAs were diluted by 10-fold before amplification.

	Step 1	Step 2	Step 3	Step 4
Temperature	25°C	37°C	85°C	4°C
Time	10 min	120 min	5 min	∞

Table 2-8 | Thermal Cycling Conditions for RT.

Quantitative Real-Time PCR (qPCR)

All quantitative real-time PCR (qPCR) experiments were complied with the Minimum Information for Publication of Quantitative Real-Time PCR Experiments (MIQE) guidelines.[102] cDNA amplification was performed using KiCqStart® SYBR® Green qPCR ReadyMix™ (Merck, Germany). A reaction cocktail without the sample template (cDNA) was prepared to reduce pipetting errors and maximise assay precision. The real-time PCR reaction assay components are described in the following Table 2-9. The mRNA primer designs (Sigma-Aldrich, USA) are listed in the following Table 2-10.

Components	Volume (µL) per Reaction	Final Concentration
KiCqStart® SYBR® Green qPCR ReadyMix™ (2X)	10.0	1X
Forward Primer (10 µM)	1.0	500 nM
Reverse Primer (10 µM)	1.0	500 nM
Nuclease-Free Water	3.0	-
cDNA	5.0	1 pg to 2 ng
Final Volume	20.0	-

Table 2-9 | Real-Time PCR Reaction Assay Components.

Gene Symbol	Gene Name	Forward Sequence (5' – 3')	Reverse Sequence (5' – 3')
VIM	Vimentin	GGAAACTAATCTGGATTCACTC	CATCTCTAGTTTCAACCGTC
CDH1	E-cadherin	CCGAGAGCTACACGTTC	TCTTCAAAATTCACTCTGCC
CDH2	N-cadherin	ACATATGTGATGACCGTAAC	TTTTTCTCGATCAAGTCCAG
SNAI1	Snail1	CTCTAATCCAGAGTTTACCTTC	GACAGAGTCCCAGATGAG
SNAI2	Snail2 / Slug	CAGTGATTATTTCCCCGTATC	CCCCAAAGATGAGGAGTATC
TWIST1	Twist1	CTAGATGTCATTGTTTCCAGAG	CCCTGTTTCTTTGAATTTGG
TWIST2	Twist2	CATAGACTTCCTCTACCAGG	CATCATTCAGAATCTCCTCC
ZEB1	ZEB1	AAAGATGATGAATGCGAGTC	TCCATTTTCATCATGACCAC
ZEB2	ZEB2	AAGACTTCGCAGATCGAG	TGATAAGAGCGGATCAGATG

CTNNB1	β-catenin	CAACTAAACAGGAAGGGATG	CACAGGTGACCACATTTATATC
MMP9	MMP-9	AAGGATGGGAAGTACTGG	GCCCAGAGAAGAAGAAAAG
GAPDH	GAPDH	ACAGTTGCCATGTAGACC	TTGAGCACAGGGTACTTTA

Table 2-10 | The mRNA Primers.

15 µL of the reaction cocktail with all the required components except the sample template (cDNA) were dispensed into separate SmartCycler® reaction tubes (Cepheid Inc., USA). Then, 5 µL of the sample template (cDNA) were added to each reaction as the final step. The real-time PCR reactions were accompanied by a no template control (NTC) in order to assess for DNA contamination and primer-dimer artefacts that could produce false positive results. The reaction tubes were briefly spun using a Cepheid mini centrifuge. All real-time PCR reactions were performed in triplicates using a SmartCycler® automated real-time PCR system (Cepheid Inc., USA). The following Table 2-11 sets the thermal cycling conditions for amplification.

	PCR Stage	Temperature	Time
Stage 1	Hold	95°C	10 min
Stage 2	Cycle (40 Cycles)		
	Denature	95°C	15 s
	Anneal/Extend	60°C	60 s
Stage 3	Melt Curve (Dissociation Stage)	95°C	10 s
		0.2°C Increments	
		60°C to 95°C	10 s

Table 2-11 | Thermal Cycling Conditions for cDNA Amplification.

RT-qPCR Data Analysis

All real-time PCR reactions were performed in triplicates and these were considered as technical replicates. The triplicates were only validated when the standard deviation (SD) was

smaller than 0.25. Post-amplification melting-curve analysis was used to check the real-time PCR reactions for primer-dimer artefacts and to ensure the reaction specificity. As the melting temperature of nucleic acids was affected by length, GC content and the presence of base mismatches amongst other factors, different real-time PCR reaction products could be distinguished by their melting characteristics. The characterisation of real-time PCR reaction products via the melting curve analysis reduced the need for time-consuming gel electrophoresis.

Independent real-time PCR reactions were performed thrice and these were considered as biological replicates. All target mRNA expressions were normalised to reference gene GAPDH. A relative expression was based on the Ct of a target gene versus the Ct of a reference gene (Delta Ct). The higher the Delta Ct value, the lower the relative gene expression. All results were expressed as relative expressions.

2.6 Immunofluorescence (IF)

Fixation

1. Using a hydrophobic barrier pen, a 10 mm circle was drawn on a poly-L-lysine coated glass slide (Sigma-Aldrich, USA).
2. 10 µL of cell suspensions that were retrieved from the microfluidic chip device as aforementioned were dispensed within the circle on the glass slide.
3. Equal volume of 4% paraformaldehyde (PFA) was dispensed on the glass and not directly on the cells.
4. The cell suspensions were carefully smeared on the glass slide within the circle with the side of a 200 µL pipette tip.
5. The cells were incubated at room temperature for 15 minutes.

Permeabilisation

6. The fixed cells were washed for 15 minutes by dispensing 200 µL of 1X PBS on the slide.
7. The solution was discarded by careful tilting of the slide and the washing step was repeated.
8. 200 µL of 0.1% Triton-X 100 was dispensed on the slide and then incubated at room temperature for 10 minutes.
9. The solution was discarded by careful tilting of the slide and the washing step was repeated twice.

Blocking

10. The cells were blocked with 4% Bovine Serum Albumin (BSA) for 1 hour at room temperature by dispensing 200 µL of blocking solution on the slide.
11. The solution was discarded by careful tilting of the slide and the washing step was repeated twice.

Primary Antibody Incubation

12. The cells were incubated with 200 µL of primary antibody cocktail in 2% BSA at room temperature for 2 hours (Table 2-12).
13. The solution was discarded by careful tilting of the slide and the washing step was repeated twice.

Secondary Antibody Incubation

14. In a dark room, the cells were incubated with 200 µL of secondary antibody cocktail in 2% BSA at room temperature for 1 hour (Table 2-12).
15. The solution was discarded by careful tilting of the slide and the washing step was repeated twice.

Counterstain

16. 1 drop of ProLong Gold Antifade Mountant with DAPI (Invitrogen, USA) was dispensed on the sample.
17. The slide was mounted with a cover slip.
18. The cells were visualised using the Leica TCS SP8 confocal laser scanning microscopy platform (Leica Microsystems, Germany).

Primary Antibody Cocktail				
Antibody	Catalog	Initial Concentration	Host	Final Dilution
TWIST2 Polyclonal Antibody	PA5-66539, ThermoFisher Scientific	0.3 mg/mL	Rabbit	1:200
Phospho-Histone H2A.X (Ser140) Monoclonal Antibody (3F2)	MA1-2022, ThermoFisher Scientific	1 mg/mL	Mouse	1:500
Secondary Antibody Cocktail				
Antibody		Catalog		Final Dilution
Goat anti-Rabbit IgG (H+L) Secondary Antibody, Alexa Fluor® 594 conjugate		R37117, ThermoFisher Scientific		1:200
F(ab')2-Goat anti-Mouse IgG (H+L) Secondary Antibody, Alexa Fluor® 488 conjugate		A-11017, ThermoFisher Scientific		1:200

Table 2-12 | Primary and secondary antibody cocktails.

2.7 Image Analysis

All acquired images were analysed with ImageJ Version 1.51. Regions of interest (ROIs) were used to define specific parts of an image that was processed independently or measured. Hence, only the pixel within any ROI that was drawn was included in the calculations when measured.

Transit Time Analysis

The Mtrack2 plugin was installed on ImageJ. It was used to track the positions of a cell cross a channel with constrictions.

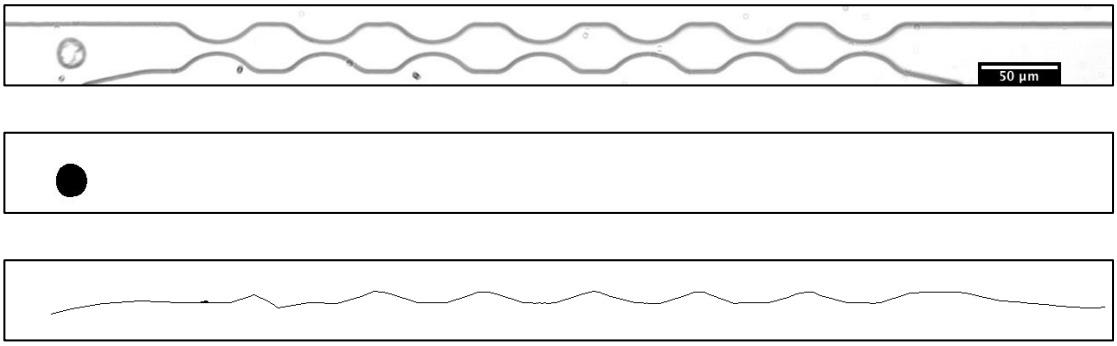

Figure 2-9 | SK-BR-3 Cell Trajectory by Flow-Induced Migration. Top: original image of the first frame. Middle: a ROI of the first frame. Bottom: the path the cell takes to cross the channel.

First, the entire image sequences were converted to mask. Then, the outline of the channel was substracted from each image sequence. Finally, the positions of the cell were measured from each image sequence. This method automatically churned the measurements of the position vector of the cell that allowed the calculations of cell velocity and cell residence time. Nonetheless, this method is only effective when there is only one cell crossing a channel from beginning to end. Manual tracking was done on image sequences that had more than one cell crossing the channel within a single time frame.

Morphological Analysis

Similarly, ROIs were used to analyse the morphology of cells. ImageJ's set measurements function allowed the generation of the following data: area, aspect ratio and integrated density. This method was also used to measure the protein presence and its localisation in a cell. Integrated Density is the product of "Area" and "Mean Gray Value".

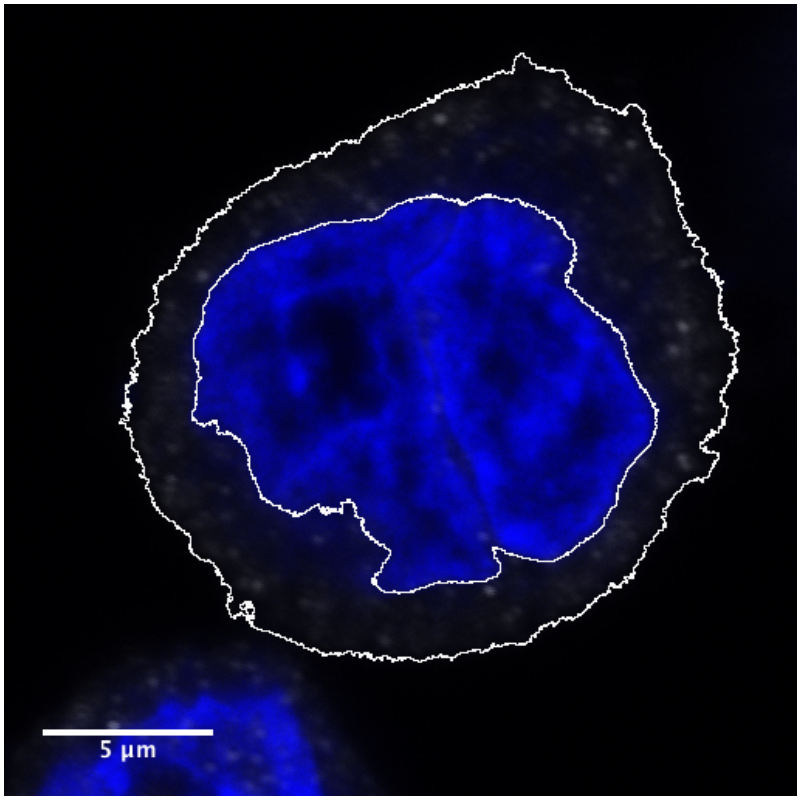

Figure 2-10 | ROIs of a SK-BR-3's nucleus envelope and cell membrane.

2.8 Statistical Analysis

All statistical hypothesis testing was conducted using the GraphPad Prism 7 software (GraphPad Software Inc., USA). An alpha of 0.05 was used as the cut-off for significance.

The Mann-Whitney test was used to compare two independent samples from populations having non-normal distributions. Although the Mann-Whitney test does not require the assumption of normal distributions, it is nearly as efficient as the t-test on normal distributions.[103] In chapter three, this method was used to compare data on velocity, transit time and residence time of cells in the microcirculation from two different applied pressure forces.

The Kruskal-Wallis test was used to compare three or more independent samples of equal or different sample sizes. The Kruskal-Wallis test extends the Mann-Whitney test when there are only two groups. In chapter three, this method was used to compare data on velocity, transit time and residence time of cells in the microcirculation on five independent samples from the same applied pressure force. In chapter four, this method was used to compare data on nucleus area, nucleus length, nuclear to cytoplasmic area ratio, nucleus aspect ratio, cell area and nuclear to cytoplasmic ratio of γH2AX protein of cells post-microcirculation on seven independent samples from the same applied pressure force. In chapter five, this method was used to compare data on the localisation of Twist2 protein of cells post-microcirculation on seven independent samples from the same applied pressure force.

The two-way analysis of variance (ANOVA) was used to examine the influence of two different categorical independent variables on one continuous dependent variable. The two-way ANOVA was also used to assess the main effect of each independent variable as well as

the interaction between them. In chapter four, this method was used to compare between two types of cells on nucleus area, nucleus length, nuclear to cytoplasmic area ratio, nucleus aspect ratio and cell area data. Also in chapter four, this method was used to compare between two areas of a cell on γH2AX protein localisation data.

The Welch's t-test was used to compare between two samples with unequal variances. Although the Welch's t-test is designed for unequal variances, the assumption of normality is maintained. This method was used to compare gene expression data between a control and a treated group for each target gene.

Correcting for Multiple Comparisons

Multiple comparisons arise when a statistical analysis involves multiple simultaneous statistical tests, each of which has a potential to produce a "discovery." A stated confidence level generally applies only to each test considered individually, but often it is desirable to have a confidence level for the whole family of simultaneous tests. Failure to compensate for multiple comparisons can have important real-world consequences.[104]

In this research thesis, several methods of multiple comparison corrections were applied depending on the experimental design of the analysed data. These methods correct for multiple comparisons resulting in the computation of a separate adjusted P value for each comparison in a family of comparisons. Therefore, the value of these adjusted P values depends on the entire family.

Conversely, the Q value presented in this research thesis is a P value that has been adjusted for the False Discovery Rate (FDR) two-stage linear step-up procedure of Benjamini, Krieger and Yekutieli. The FDR is the proportion of false positives that can be expected from a test. While a P value of 5% means that 5% of all tests will result in false positives, a Q value of 5% means that 5% of significant results will result in false positives. Therefore, the FDR approach has higher power to find truly significant results.[105]

CHAPTER THREE: TUMOUR CELL MECHANICAL PHENOTYPING BY FLOW-INDUCED MIGRATION IN MICRO CONSTRICTIONS

3.1 Introduction

As was previously discussed in Chapter One, various techniques have been established for studying cell mechanics such as atomic force microscopy[106–108], optical tweezers[109], micropipette aspiration[110] and cell stretching[111]. The mechanical properties of cells have been considered as biomarkers to indicate presence of various diseases and changes in cell states.[95] For instance, it is known that epithelial tumour cells are larger in size and are more deformable as compared to normal healthy cells.[73]

Circulating tumour cells are a component of the "liquid biopsy" concept, which holds great potential to transform the current landscape of cancer therapy.[24] However, little is known about the changes in cell mechanical properties and on the mechanisms behind the fate of intravasated cells while in the microcirculation.

In this chapter, the changes in the mechanical phenotype of normal and cancer epithelial cells to fluid shear stress from circulation and mechanical constraint from constrictions are investigated based on their flow-induced migration. The combined experimental and theoretical technique that enables the characterisation of transit time, cell area and deformability of various biological cells will be discussed. The cells were driven into a microfluidic device that comprises micro constrictions. As multiple cells simultaneously transit through the device, channel occlusions can alter flow rates, and thus entry velocities of cells into neighbouring constrictions. Transient lane occlusions may also contribute to variation in transit time within channels. Fabricating a device that comprises multiple parallel channels of micro constrictions can eliminate device clogging and facilitate characterisation of single cells of different sizes and types on a single device with high-throughput performance.

3.2 Aims

The objective of this experiment is to characterise the mechanical phenotype of epithelial cells while in circulation, confinement and constrictions within the microfluidic system from transit time data.

1) To test the fluid dynamics of the microfluidic model that contains channels with mechanical constrictions, one type of geometry is fabricated and used in order to apply different pressure points for flow induction. Each channel is 420 μm in total length with a height of 20 μm and multiple 6 μm-wide constrictions spaced apart by 26 μm-wide chambers that are 20 μm in length. There are a total of 10 channels arranged in parallel in one microfluidic device.

2) To optimise and characterise the microfluidic system, two epithelial cell types are loaded into separate microfluidic devices. The flow-induced migration of these epithelial cells through the micro constrictions is recorded and measured for their speed and residence time. The first type of epithelial cell is a breast cancer cell line, SK-BR-3. The second type of epithelial cell is a normal kidney tubule cell line, MDCK II.

3) To test the effects of mechanical constrictions on the flow-induced migration behaviour of single tumour cells, different geometric microfluidic models are used while keeping the applied pressure constant. Two types of tumour cells are chosen, both originating from the same organ: breast cancer cell lines SK-BR-3 and MDA-MB-231. These two types of tumour cells will remain as experimental models for follow-up tests in the sequential chapters.

3.3 Results

In order to optimise and characterise the microfluidic system, one type of geometry was used. Microfluidic chips containing 10 channels arranged in parallel were fabricated. Each channel consisted of 7 x 40 µm-long constrictions (Figure 3-1). This type of geometry was selected for the optimisation and initial characterisation of the microfluidic system because it resulted in substantial and observable cellular deformations. This microfluidic design was calculated for its flow resistance based on Newtonian fluid in order to estimate the flow rate of different applied pressure points (Figure 3-2). Then, cancer and normal epithelial cell lines were delivered into this microfluidic device for single cell mechanical phenotyping by flow-induced migration.

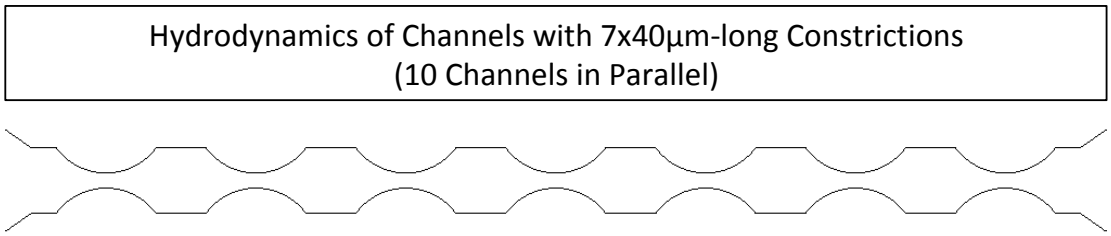

Figure 3-1. Geometry of a single channel of 7x40µm-long constrictions out of 10 channels in parallel.

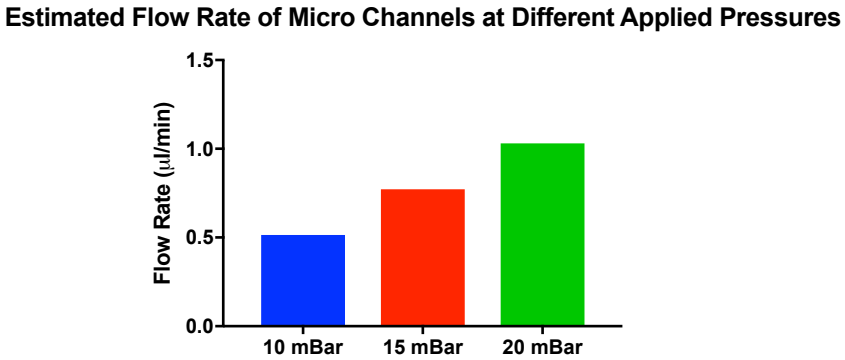

Figure 3-2. The estimated flow rate of the microfluidic device with 10 channels of 7x40µm-long constrictions arranged in parallel at different applied pressures based on an estimated flow resistance of 1.6 x 10^{13} Pa/um^3.

Figure 3-3A illustrates the trajectory of a cell in a micro channel with 7 x 40 µm-long constrictions. SK-BR-3 breast cancer cells were loaded into the microfluidic device at 10 mBar and 15 mBar through a flow control system. Their flow-induced migration positions through the channel were recorded and plotted as shown in Figure 3-3B for 10 mBar and 15 mBar.

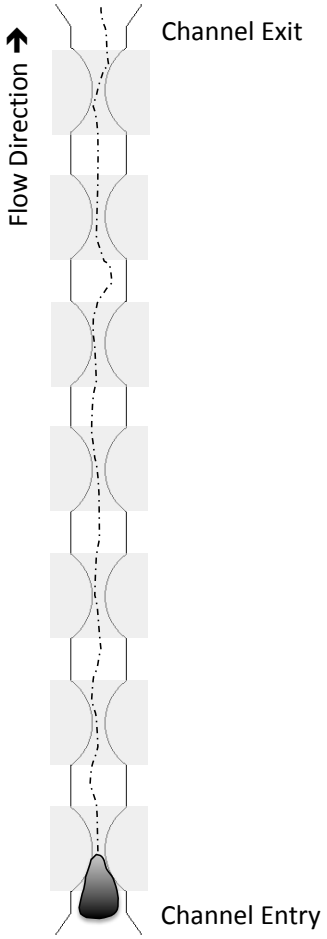

Figure 3-3A. An illustration of a cell entering a micro channel of 7x40µm-long constrictions. The dotted lines represent the path taken by the cell during transit. Grey regions represent area of constrictions.

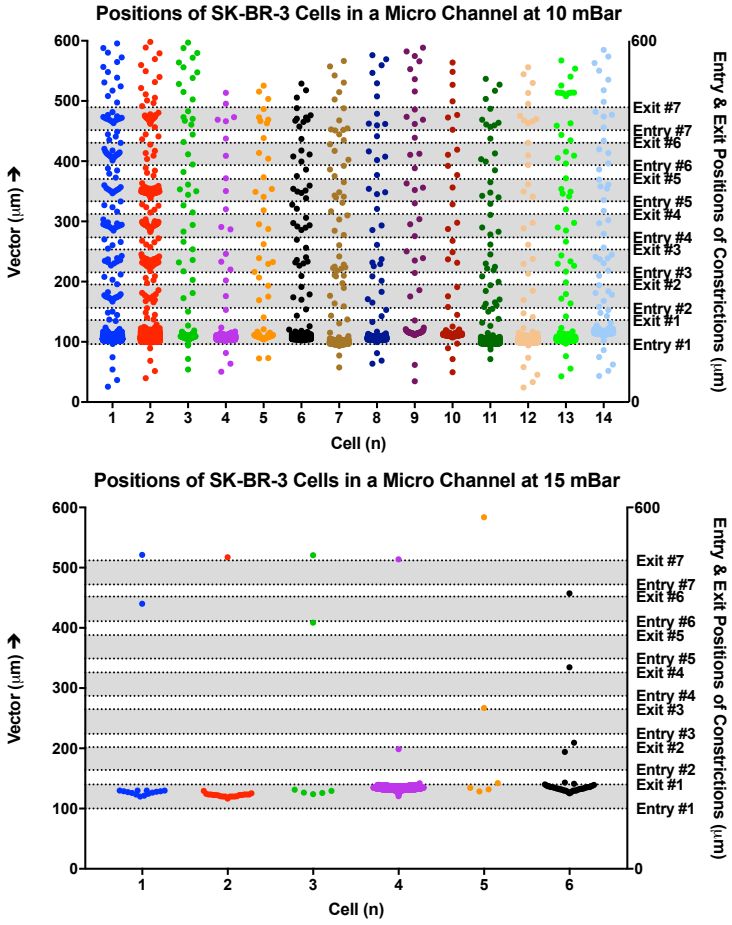

Figure 3-3B. The cell positions of SK-BR-3 cells transiting through a micro channel of 7x40µm-long constrictions at 10 mBar (top) and 15 mBar (bottom) are plotted. Each point represents the position of a cell in a micro channel. Grey regions represent area of constrictions. White regions within grey regions represent unconfined/unconstricted chambers. Image acquisitions at 30 frames per second for 10 mBar and 50 frames per second for 15 mBar.

Their flow-induced migration positions as a function of time were then plotted as shown in Figure 3-4 for 10 mBar and 15 mBar.

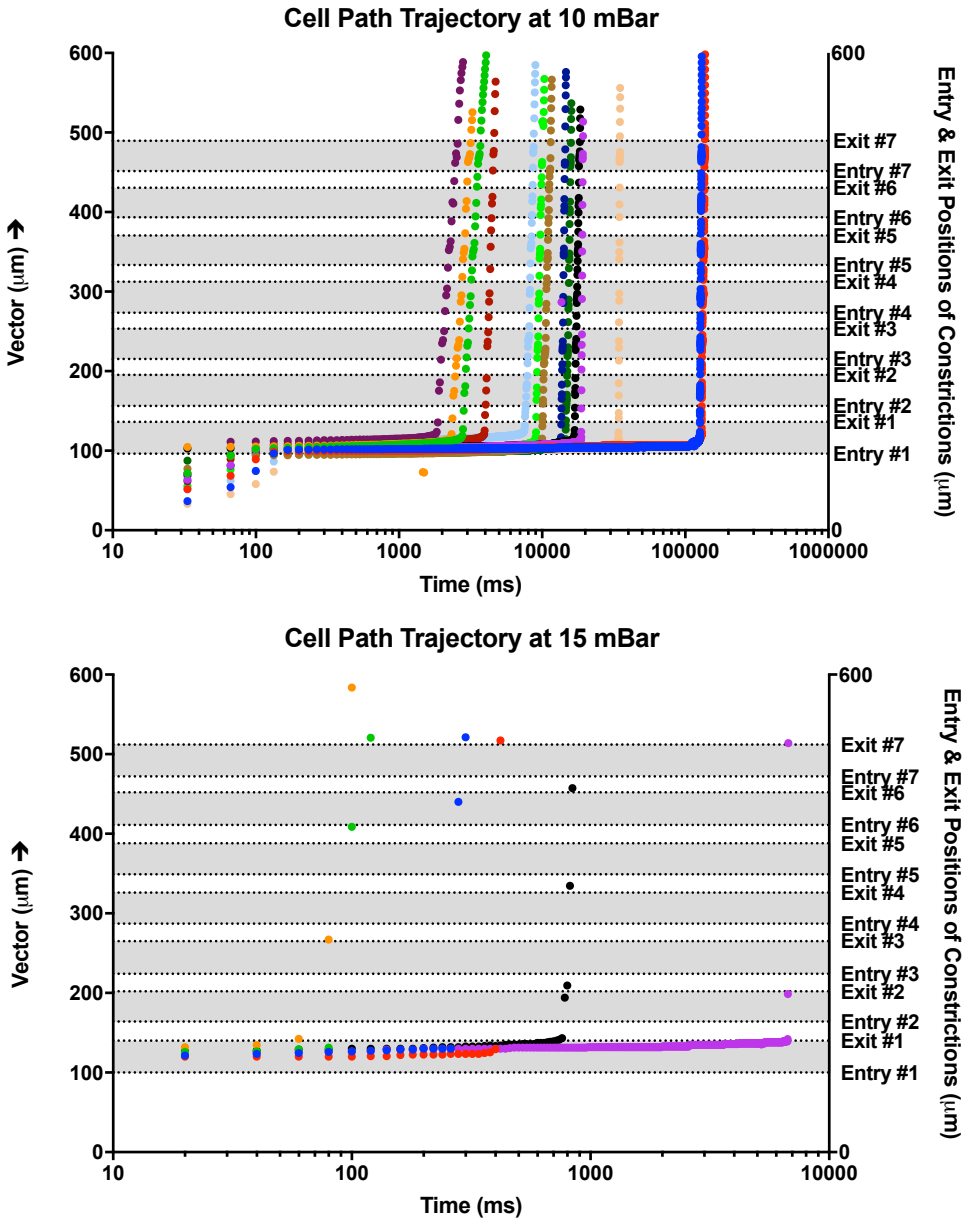

Figure 3-4. The cell positions of SK-BR-3 cells transiting through a micro channel of 7x40µm-long constrictions at 10 mBar (top) and 15 mBar (bottom) as a function of time are plotted. Each coloured trajectory represents the positions of one cell in a micro channel. Grey regions represent area of constrictions. White regions within grey regions represent unconfined/unconstricted chambers. Image acquisitions at 30 frames per second for 10 mBar and 50 frames per second for 15 mBar.

From these trajectories, the velocity (Figure 3-5), global transit time (the average time spent to cross the entire channel, Figure 3-6), transit time during the initial cellular deformation in the first constriction (the average time spent within the first constriction, Figure 3-7) and residence time (the average proportion of the time spent in the first constriction over the global transit time, Figure 3-8) were measured.

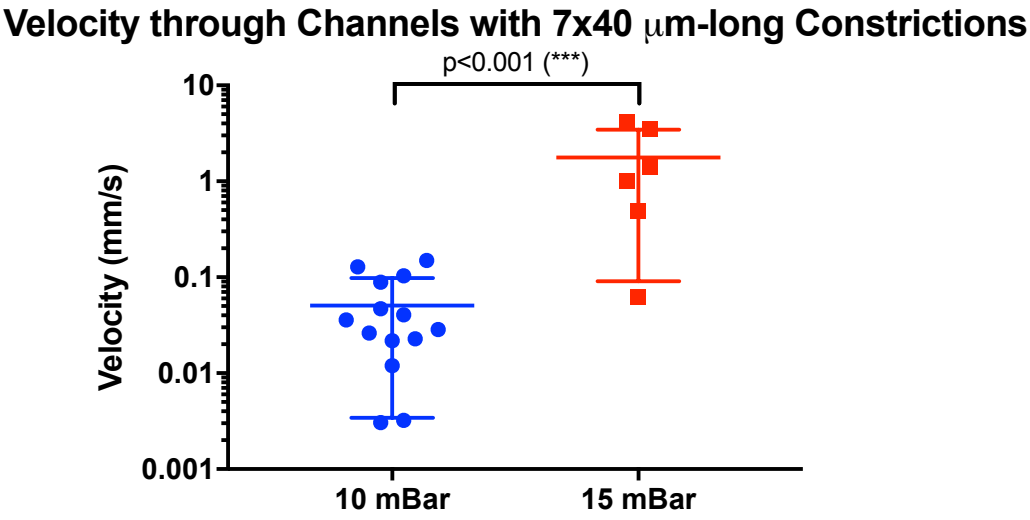

Figure 3-5. Velocity of SK-BR-3 cells transiting through micro channels with 7x40µm-long constrictions at two different applied pressures in log scale. 10 mBar (n=14) and 15 mBar (n=6). Error bars represent standard deviation. Mann-Whitney test was used at the 5% (0.05) significance level.

The velocity of SK-BR-3 cells at 15 mBar was significantly increased (1.78 mm/s) as compared to the velocity of SK-BR-3 cells at 10 mBar (0.05 mm/s, $p<0.001$).

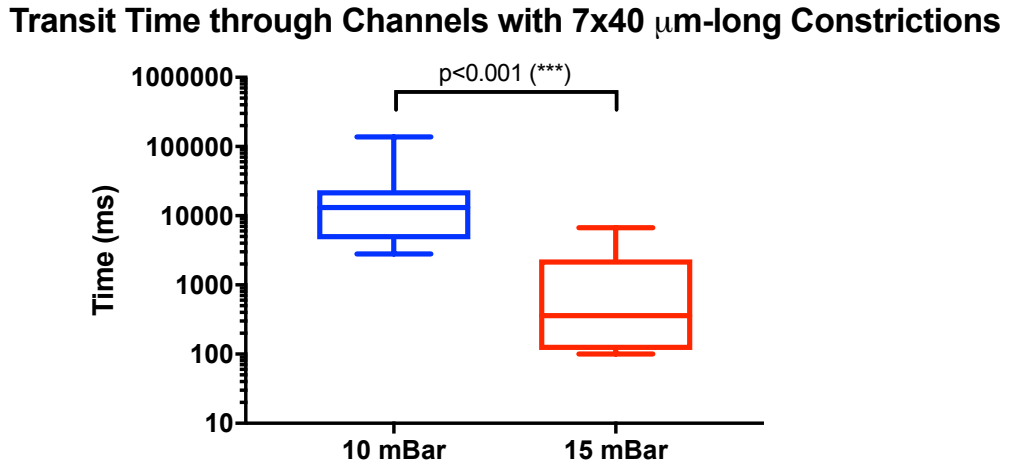

Figure 3-6. Box plots in log scale of the global transit time of SK-BR-3 cells transiting through micro channels with 7x40µm-long constrictions at two different applied pressures. 10 mBar (n=14) and 15 mBar (n=6). Error bars represent 5-95 percentiles. Mann-Whitney test was used at the 5% (0.05) significance level.

The global transit time of SK-BR-3 cells at 15 mBar (1.42 s) were significantly decreased as compared to those of SK-BR-3 cells at 10 mBar (29.8 s, p<0.001).

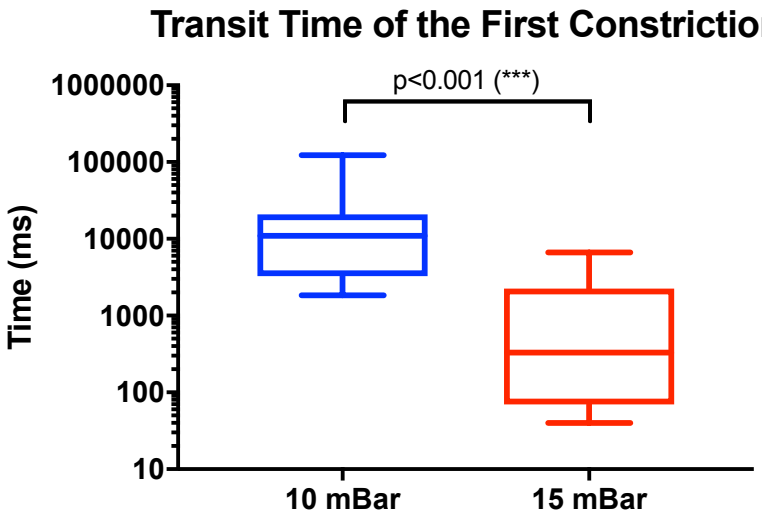

Figure 3-7. Box plots in log scale of the first constriction transit time of SK-BR-3 cells transiting through micro channels with 7x40µm-long constrictions at two different applied pressures. 10 mBar (n=14) and 15 mBar (n=6). Error bars represent 5-95 percentiles. Mann-Whitney test was used at the 5% (0.05) significance level.

The transit time of the first constriction of SK-BR-3 cells at 15 mBar (1.37 s) were significantly decreased as compared to those of SK-BR-3 cells at 10 mBar (26.2 s, p<0.001).

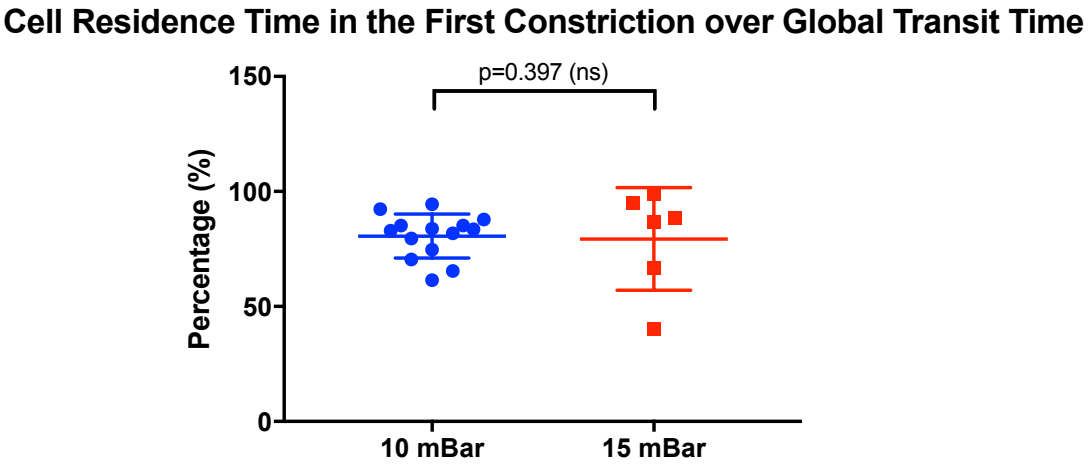

Figure 3-8. A categorical scatter plot of the percentage of cell residence time of SK-BR-3 cells in the first constriction over the global transit time at two different applied pressures. 10 mBar (n=14) and 15 mBar (n=6). Error bars represent 5-95 percentiles. Mann-Whitney test was used at the 5% (0.05) significance level.

However, the percentage of cell residence time in the first constriction over the global transit time between 10 mBar and 15 mBar was insignificantly different (80.6% and 79.3% at 10 mBar and 15 mBar respectively, p=0.397).

Then, normal epithelial cells were analysed in order to compare to the results obtained from cancer epithelial SK-BR-3 cells. MDCK II normal kidney tubule cells were loaded into the microfluidic device at 15 mBar and 20 mBar through a flow control system. Similarly, their flow-induced migration positions through the channel with constrictions were recorded and plotted as shown in Figure 3-9 for 15 mBar and 20 mBar respectively.

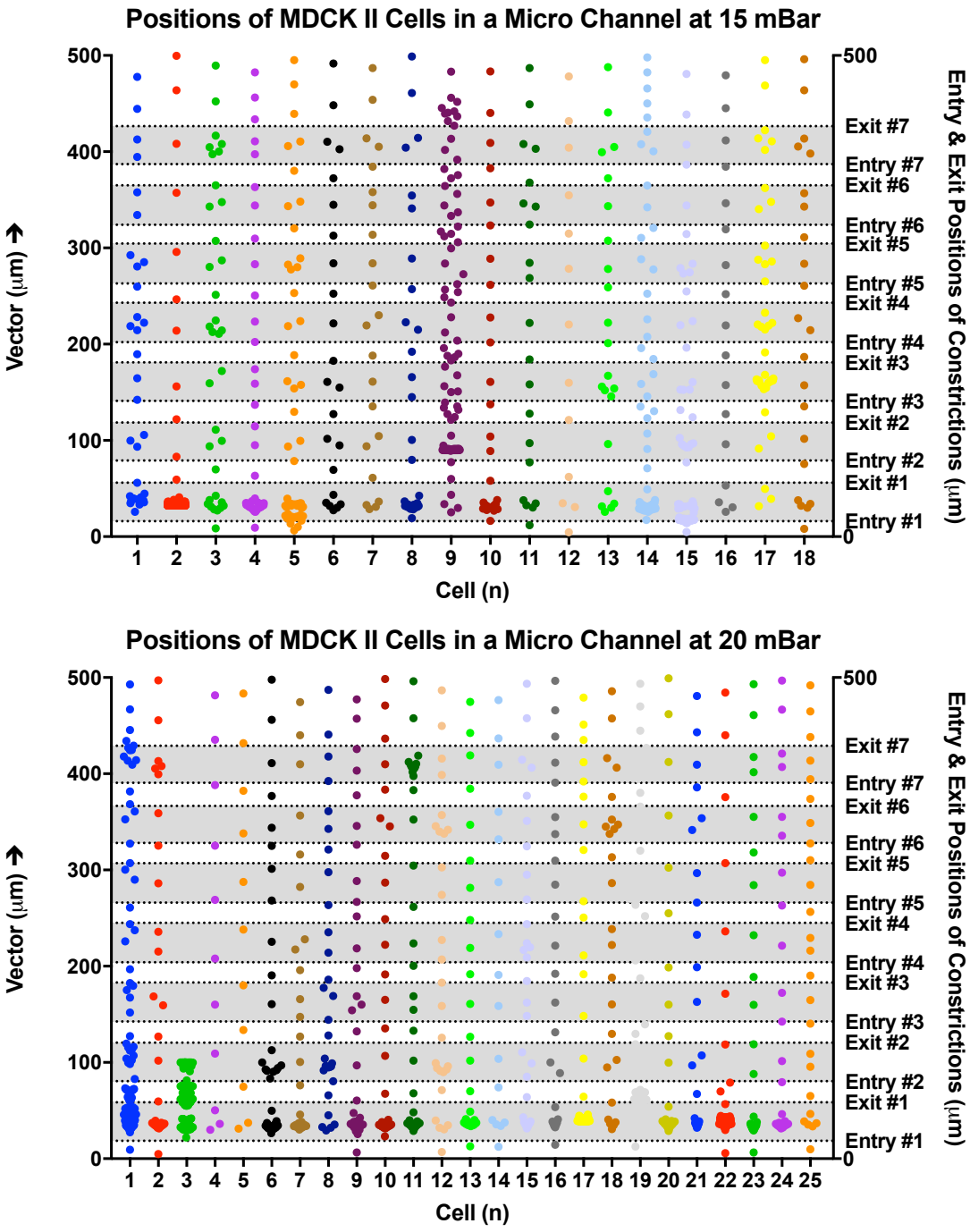

Figure 3-9. The cell positions of MDCK II cells transiting through a micro channel of 7x40µm-long constrictions at 15 mBar (top) and 20 mBar (bottom) are plotted. Each point represents the position of a cell in a micro channel. Grey regions represent area of constrictions. White regions within grey regions represent unconfined/unconstricted chambers. Image acquisitions at 50 frames per second for both applied pressure points.

Their flow-induced migration positions as a function of time were then plotted as shown in Figure 3-10 for 15 mBar and 20 mBar.

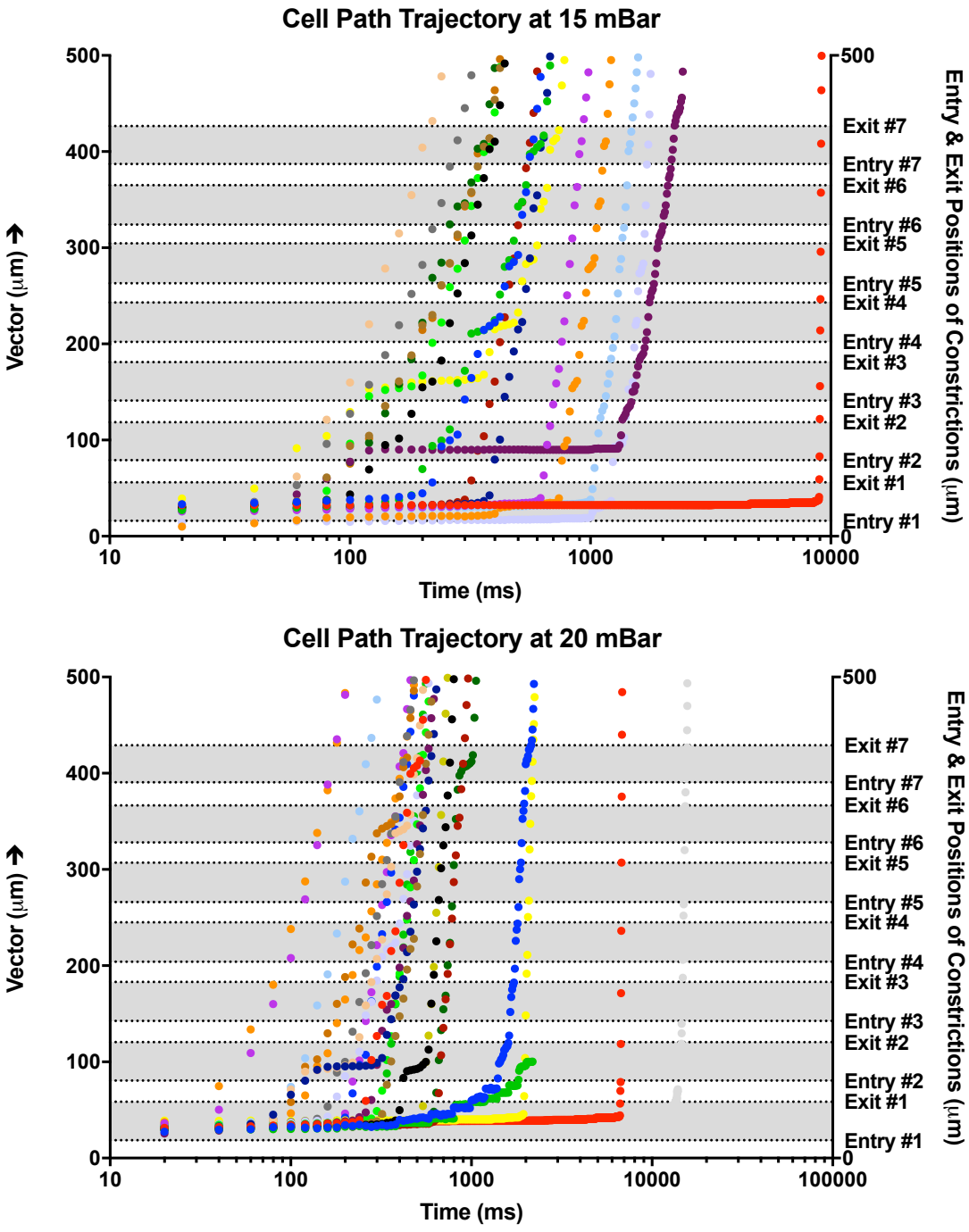

Figure 3-10. The cell positions of MDCK II cells transiting through a micro channel of 7x40µm-long constrictions at 15 mBar (top) and 20 mBar (bottom) as a function of time are plotted. Each coloured trajectory represents the positions of one cell in a micro channel. Grey regions represent area of constrictions. White regions within grey regions represent unconfined/unconstricted chambers. Image acquisitions at 50 frames per second for both applied pressure points.

From these trajectories, the velocity (Figure 3-11), global transit time (Figure 3-12), transit time during the initial cellular deformation (Figure 3-13) and residence time in the channel (Figure 3-14) were also measured.

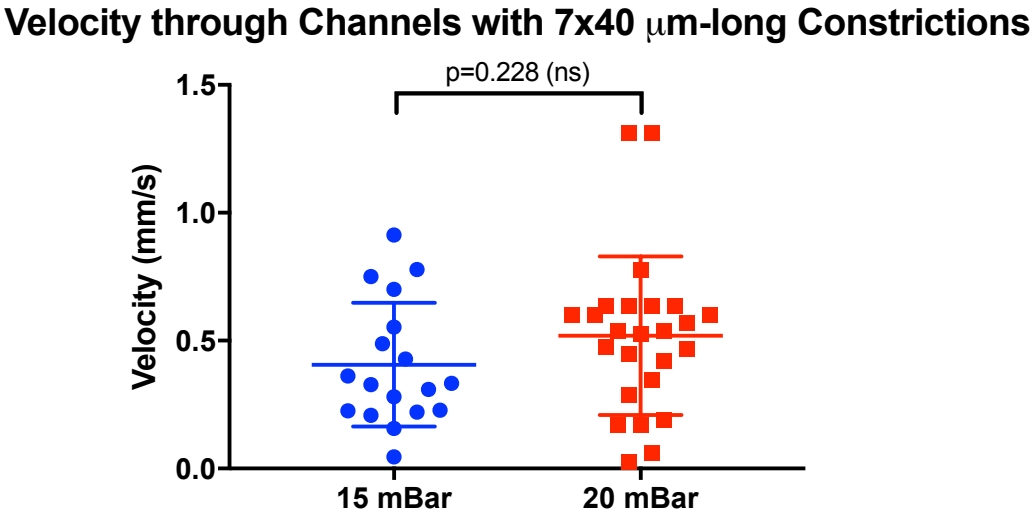

Figure 3-11. Velocity of MDCK II cells transiting through micro channels with 7x40µm-long constrictions at two different applied pressures. 15 mBar (n=18) and 20 mBar (n=25). Error bars represent standard deviation. Mann-Whitney test was used at the 5% (0.05) significance level.

The mean velocities of MDCK II cells transiting through micro channels with 7 x 40 µm-long constrictions were 0.4 mm/s and 0.52 mm/s at 15 mBar and 20 mBar respectively (ns).

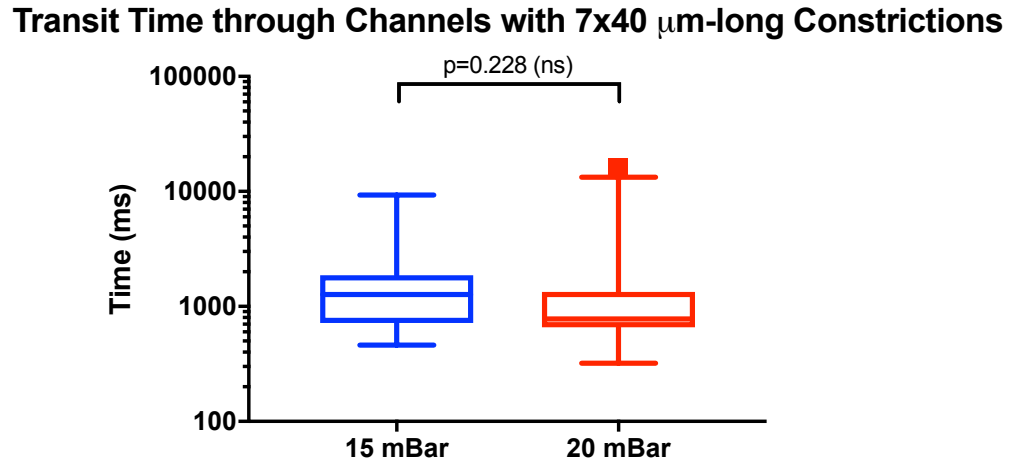

Figure 3-12. Box plots in log scale of the global transit time of MDCK II cells transiting through micro channels with 7x40µm-long constrictions at two different applied pressures. 15 mBar (n=18) and 20 mBar (n=25). Error bars represent 5-95 percentiles. Mann-Whitney test was used at the 5% (0.05) significance level.

The mean global transit times of MDCK II cells transiting through micro channels with 7 x 40 µm-long constrictions were 1.72 s and 1.82 s at 15 mBar and 20 mBar respectively (ns).

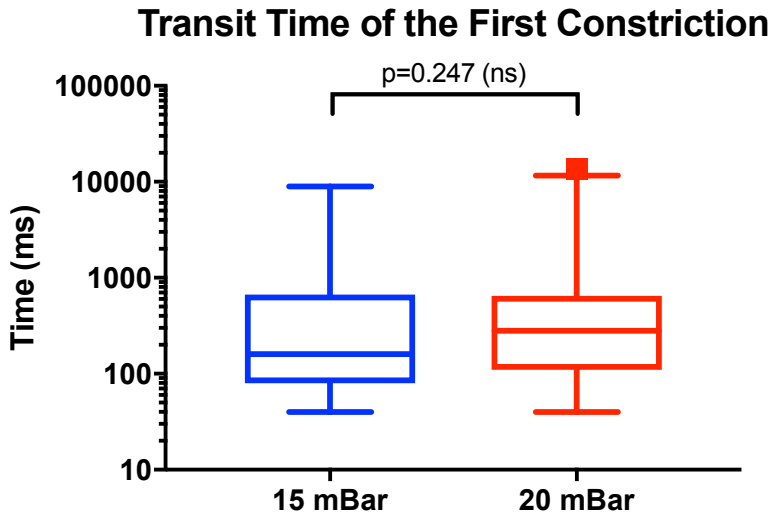

Figure 3-13. Box plots in log scale of the first constriction transit time of MDCK II cells transiting through micro channels with 7x40µm-long constrictions at two different applied pressures. 15 mBar (n=18) and 20 mBar (n=25). Error bars represent 5-95 percentiles. Mann-Whitney test was used at the 5% (0.05) significance level.

The mean transit times of the first constriction of MDCK II cells were 0.81 s and 1.21 s at 15 mBar and 20 mBar respectively (ns). The velocity (p=0.228), global transit time (p=0.228) and transit time of the first constriction (p=0.247) of MDCK II cells at 15 mBar were all insignificantly different compared to those at 20 mBar.

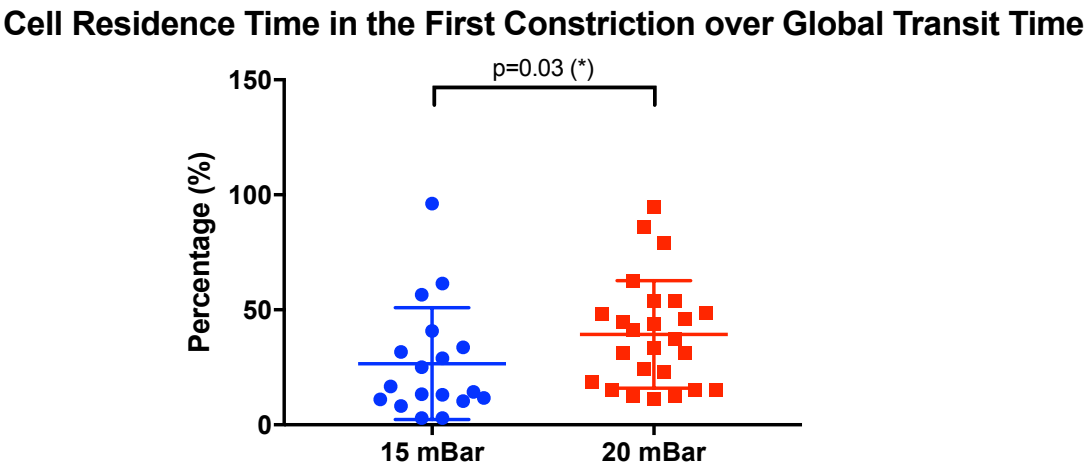

Figure 3-14. A categorical scatter plot of the percentage of cell residence time of MDCK II cells in the first constriction over the global transit time at two different applied pressures. 15 mBar (n=18) and 20 mBar (n=25). Error bars represent 5-95 percentiles. Mann-Whitney test was used at the 5% (0.05) significance level.

However, the percentage of cell residence time in the first constriction over the global transit time at 20 mBar was significantly increased (p=0.03), as compared to that at 15 mBar. The mean percentages of cell residence time in the first constriction over the global transit time were 26.6% and 39.3% at 15 mBar and 20 mBar respectively.

Additionally, the projected surface area of MDCK II cells was measured before, during and after exiting the constrictions and these data are presented in Figure 3-15 for 15 mBar and 20 mBar.

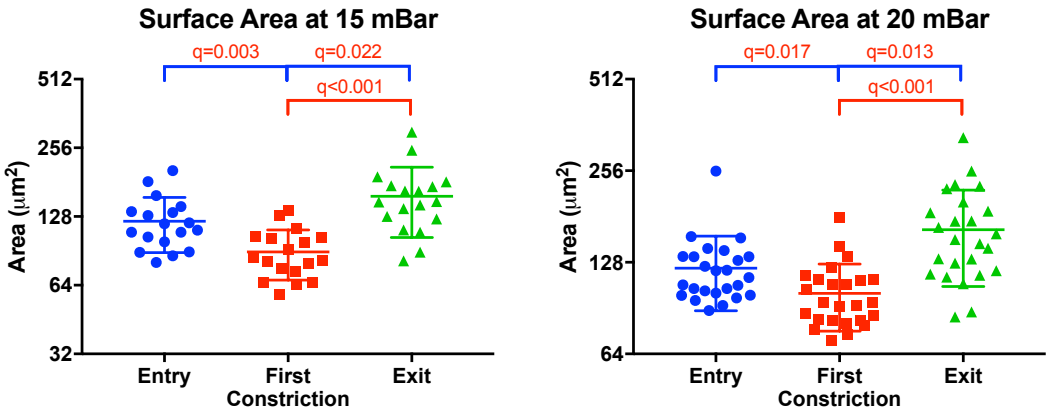

Figure 3-15. A categorical scatter plot in log scale of the surface area of MDCK II cells before, while and after transiting through micro channels with 7x40μm-long constrictions at 15 mBar (left) and 20 mBar (right). 15 mBar (n=18) and 20 mBar (n=25). Error bars represent standard deviation. Q values from Kruskal-Wallis test with multiple hypothesis correction (two-stage linear step-up procedure of Benjamini, Krieger and Yekutieli), and significance and confidence level at 0.05. Q values in red denote significant values.

The mean projected surface areas of MDCK II cells before, during and after exiting the constrictions at 15 mBar were 122 μm^2, 89.5 μm^2 and 157 μm^2 respectively. While the mean projected surface areas of MDCK II cells before, during and after exiting the constrictions at 20 mBar were 122 μm^2, 101 μm^2 and 164 μm^2 respectively. Therefore, the projected surface area of MDCK II cells significantly decreased during the initial constriction and significantly increased after exiting the last constriction for both 15 mBar and 20 mBar when compared to the surface area of MDCK II cells before entering the initial constriction.

In order to test the effects of different geometric mechanical constrictions on the flow-induced migration of single tumour cells, five types of geometric microfluidic models as described in Chapter Two were fabricated. All of these microfluidic designs were calculated for their flow resistance based on Newtonian fluid in order to estimate their flow rate at a constant applied pressure (Figure 3-16).

Hydrodynamics of Different Types of Geometry (4 Channels in Parallel)

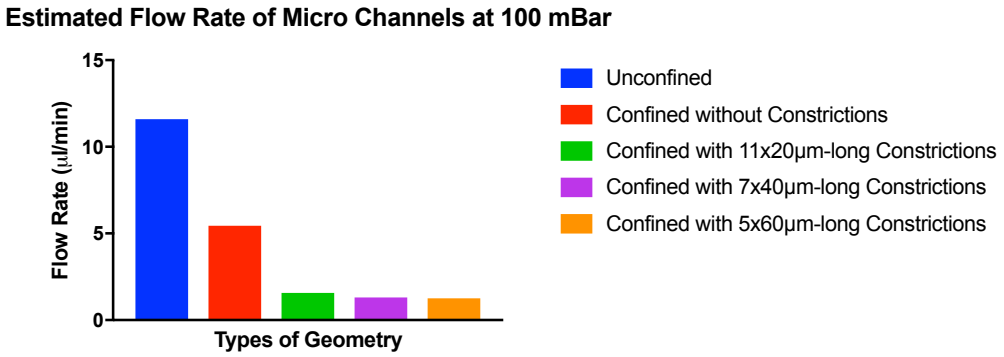

Figure 3-16. The estimated flow rate of the microfluidic device with 4 channels arranged in parallel for different types of geometry at a constant applied pressure of 100 mBar (10 kPa). Unconfined: 20µm height, confined without constrictions: 15µm height, confined with 11x20µm-long constrictions: 15µm height, confined with 7x40µm-long constrictions: 15µm height and confined with 5x60µm-long constrictions: 15µm height.

100 mBar was chosen as the optimal constant pressure applied on these microfluidic models with 4 channels in parallel in order to match the estimated flow rate of the geometry with the highest flow resistance (confined with 5 x 60 µm-long constrictions) with the range of estimated flow rates of the microfluidic model with 10 channels in parallel. Furthermore, this applied pressure reduced chip clogging and maintained the integrity of transiting cells.

Two types of breast cancer cell lines – SK-BR-3 and MDA-MB-231 – were selected and delivered into all of these five types of geometric microfluidic models for single cell mechanical phenotyping by flow-induced migration. This experimental design remains as the default for follow-up tests and analyses as will be unveiled in the following chapters of this thesis.

SK-BR-3 breast cancer cells were loaded into all five types of geometric microfluidic devices at 100 mBar through a flow control system. The velocity of these cells through the micro channels was measured (Figure 3-17).

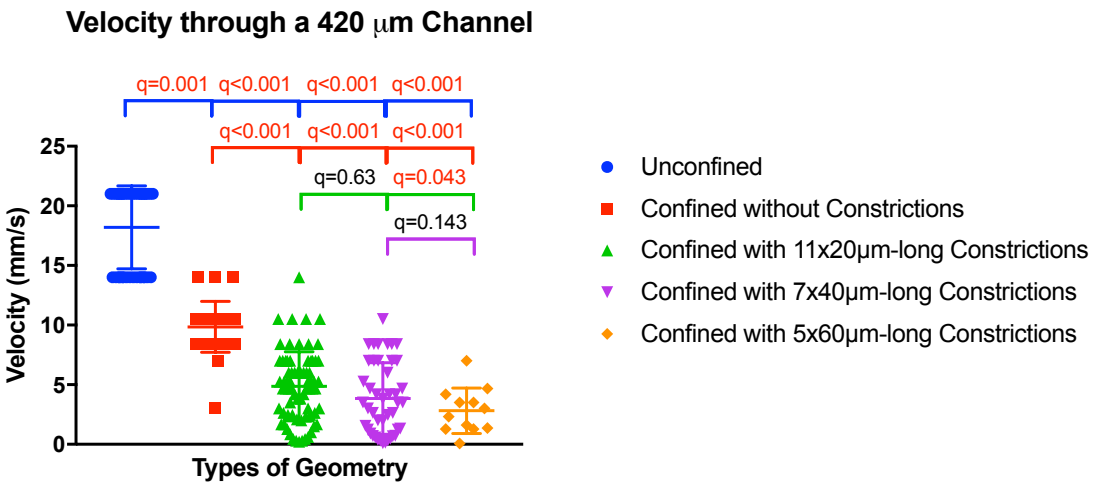

Figure 3-17. Velocity of SK-BR-3 cells transiting through micro channels with a constant applied pressure of 100 mBar (10 kPa). Unconfined: 20μm height (n=40), confined without constrictions: 15μm height (n=30), confined with 11x20μm-long constrictions: 15μm height (n=73), confined with 7x40μm-long constrictions: 15μm height (n=44) and confined with 5x60μm-long constrictions: 15μm height (n=12). Error bars represent standard deviation. Q values from Kruskal-Wallis test with multiple hypothesis correction (two-stage linear step-up procedure of Benjamini, Krieger and Yekutieli), and significance and confidence level at 0.05. Q values in red denote significant values.

When compared to the unconfined geometry (channels with a height of 20 μm without constrictions), the velocity of SK-BR-3 cells through all the rest of the microfluidic designs were significantly decreased ($q<0.001$). When compared to the confined without constrictions geometry (channels with a height of 15 μm without constrictions), the velocity of SK-BR-3 cells through all of the microfluidic designs with constrictions were significantly decreased as well ($q<0.001$). The mean velocities of SK-BR-3 cells transiting through micro channels at 100 mBar were 18.2 mm/s for unconfined, 9.85 mm/s for confined without constrictions, 4.86 mm/s for confined with 11 x 20 μm-long constrictions, 3.84 mm/s for confined with 7 x 40 μm-long constrictions and 2.82 mm/s for confined with 5 x 60 μm-long constrictions. However, amongst the microfluidic designs with constrictions, statistical analysis from Kruskal-Wallis test with multiple hypothesis correction (two-stage linear step-up procedure of Benjamini, Krieger and Yekutieli) identified as significant only the decrease of velocity in the confined with 5 x 60 μm-long constrictions as compared to confined with 11 x 20 μm-long constrictions ($q=0.043$). Only the channels with constrictions were analysed

for global transit time, transit time during the initial cellular deformation (Figure 3-18) and residence time in the channel (Figure 3-19).

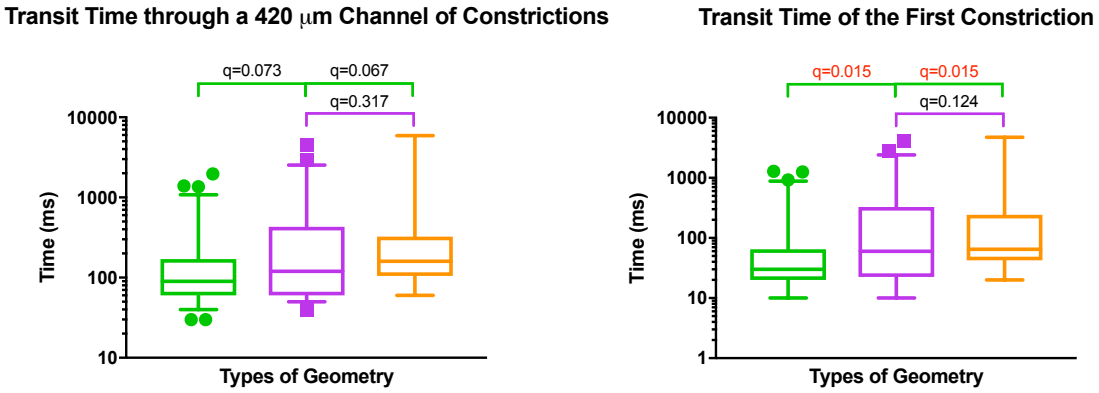

Figure 3-18. Box plots on log scale of the global transit time (left) and the first constriction transit time (right) of SK-BR-3 cells. Confined with 11x20μm-long constrictions: 15μm height (n=73), confined with 7x40μm-long constrictions: 15μm height (n=44) and confined with 5x60μm-long constrictions: 15μm height (n=12). Error bars represent 5-95 percentiles. Q values from Kruskal-Wallis test with multiple hypothesis correction (two-stage linear step-up procedure of Benjamini, Krieger and Yekutieli), and significance and confidence level at 0.05. Q values in red denote significant values.

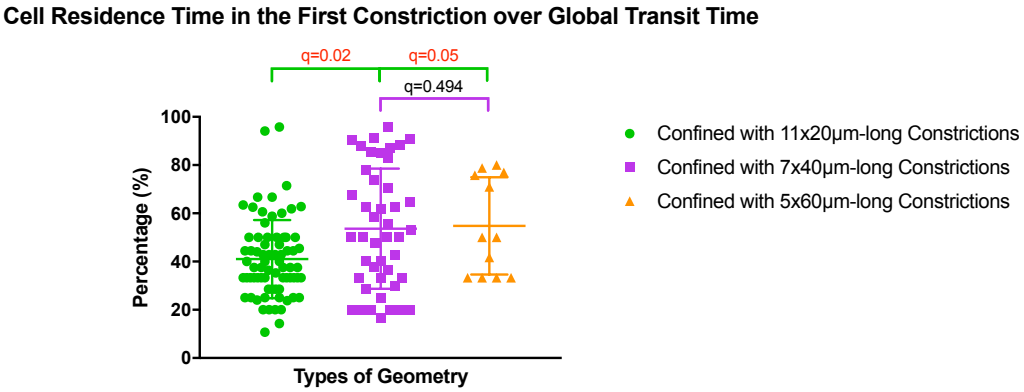

Figure 3-19. A categorical scatter plot of the percentage of cell residence time of SK-BR-3 cells in the first constriction over the global transit time. Confined with 11x20μm-long constrictions: 15μm height (n=73), confined with 7x40μm-long constrictions: 15μm height (n=44) and confined with 5x60μm-long constrictions: 15μm height (n=12). Error bars represent standard deviation. Q values from Kruskal-Wallis test with multiple hypothesis correction (two-stage linear step-up procedure of Benjamini, Krieger and Yekutieli), and significance and confidence level at 0.05. Q values in red denote significant values.

The global transit time was insignificantly different amongst the three types of channels with constrictions. Nonetheless, the q values of the global transit times comparing confined with 11 x 20 μm-long constrictions with confined with 7 x 40 μm-long constrictions (q=0.073) and comparing confined with 11 x 20 μm-long constrictions with confined with 5 x 60 μm-long constrictions (q=0.067) are not very far from significance. The mean global transit times of

SK-BR-3 cells transiting through micro channels at 100 mBar were 204 ms for confined with 11 x 20 µm-long constrictions, 438 ms for confined with 7 x 40 µm-long constrictions and 662 ms for confined with 5 x 60 µm-long constrictions. However, statistical significance is seen in the transit times of the first constriction of the confined with 7 x 40 µm-long constrictions (q=0.015) and the confined with 5 x 60 µm-long constrictions (q=0.015) when compared to the confined with 11 x 20 µm-long constrictions. The mean transit times of the first constriction of SK-BR-3 cells were 116 ms for confined with 11 x 20 µm-long constrictions, 358 ms for confined with 7 x 40 µm-long constrictions and 498 ms for confined with 5 x 60 µm-long constrictions. Similarly, statistical significance is seen in the percentages of cell residence time in the first constriction over the global transit time of the confined with 7 x 40 µm-long constrictions (q=0.02) and the confined with 5 x 60 µm-long constrictions (q=0.05) when compared to the confined with 11 x 20 µm-long constrictions. The percentages of cell residence time in the first constriction over the global transit time were 41% for confined with 11 x 20 µm-long constrictions, 54% for confined with 7 x 40 µm-long constrictions and 55% for confined with 5 x 60 µm-long constrictions.

Another type of tumour cells were treated and analysed similarly to SK-BR-3 cells. MDA-MB-231 breast cancer cells were also loaded into all five types of geometric microfluidic devices at 100 mBar through a flow control system. The velocity of these cells through the micro channels was measured (Figure 3-20).

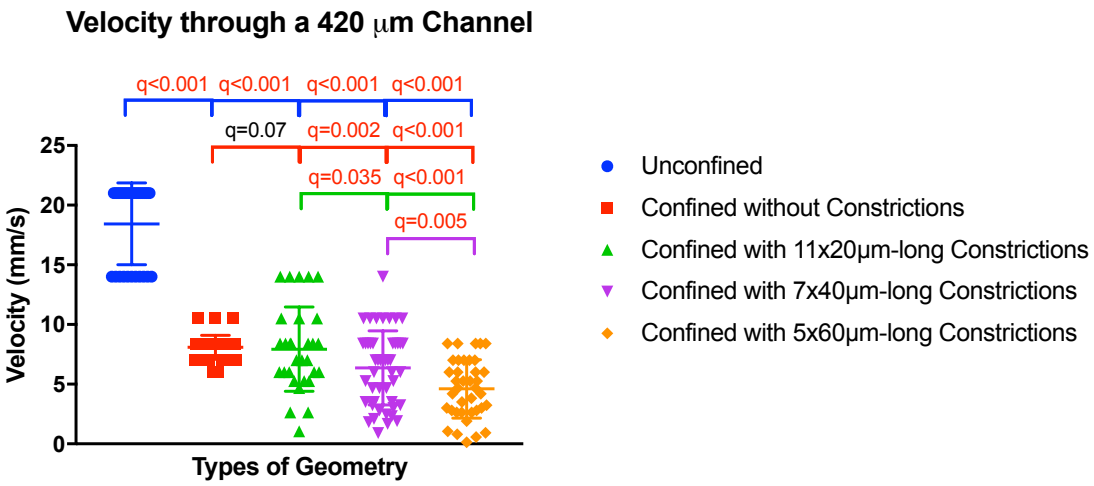

Figure 3-20. Velocity of MDA-MB-231 cells transiting through micro channels with a constant applied pressure of 100 mBar (10 kPa). Unconfined: 20μm height (n=30), confined without constrictions: 15μm height (n=42), confined with 11x20μm-long constrictions: 15μm height (n=30), confined with 7x40μm-long constrictions: 15μm height (n=47) and confined with 5x60μm-long constrictions: 15μm height (n=38). Error bars represent standard deviation. Q values from Kruskal-Wallis test with multiple hypothesis correction (two-stage linear step-up procedure of Benjamini, Krieger and Yekutieli), and significance and confidence level at 0.05. Q values in red denote significant values.

When compared to the unconfined geometry (channels with a height of 20 μm without constrictions), the velocity of MDA-MB-231 cells through all the rest of the microfluidic designs were significantly decreased (q<0.001). When compared to the confined without constrictions geometry (channels with a height of 15 μm without constrictions), the velocity of MDA-MB-231 cells in confined with 11 x 20 μm-long constrictions was insignificantly different (q=0.07) but were significantly decreased in confined with 7 x 40 μm-long constrictions (q=0.002) and confined with 5 x 60 μm-long constrictions (q<0.001). The mean velocities of MDA-MB-231 cells transiting through micro channels at 100 mBar were 18.4 mm/s for unconfined, 8.1 mm/s for confined without constrictions, 7.93 mm/s for confined with 11 x 20 μm-long constrictions, 6.36 mm/s for confined with 7 x 40 μm-long constrictions and 4.61 mm/s for confined with 5 x 60 μm-long constrictions. Indeed for MDA-MB-231 cells, statistical analysis from Kruskal-Wallis test with multiple hypothesis correction (two-stage linear step-up procedure of Benjamini, Krieger and Yekutieli) identified significant decrease of velocities amongst the microfluidic designs with

constrictions when compared to each other. Only the channels with constrictions were analysed for global transit time, transit time during the initial cellular deformation (Figure 3-21) and residence time in the channel (Figure 3-22).

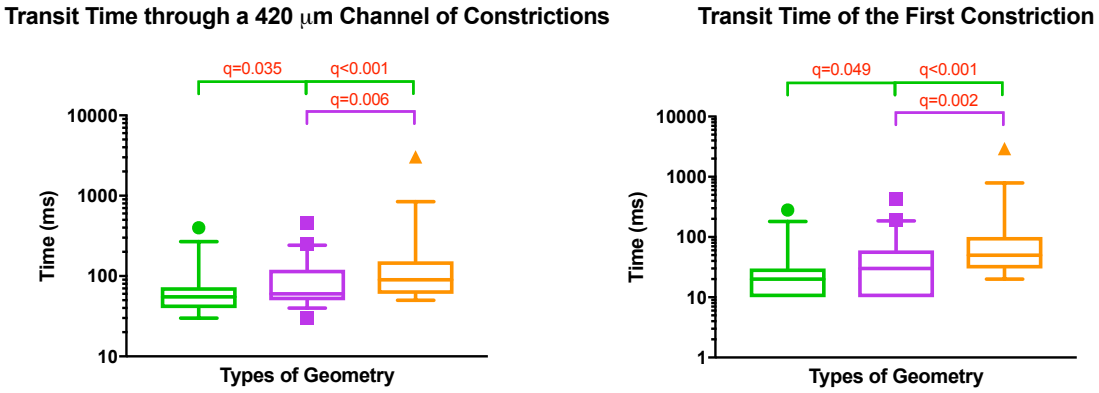

Figure 3-21. Box plots on log scale of the global transit time (left) and the first constriction transit time (right) of MDA-MB-231 cells. Confined with 11x20μm-long constrictions: 15μm height (n=30), confined with 7x40μm-long constrictions: 15μm height (n=47) and confined with 5x60μm-long constrictions: 15μm height (n=38). Error bars represent 5-95 percentiles. Q values from Kruskal-Wallis test with multiple hypothesis correction (two-stage linear step-up procedure of Benjamini, Krieger and Yekutieli), and significance and confidence level at 0.05. Q values in red denote significant values.

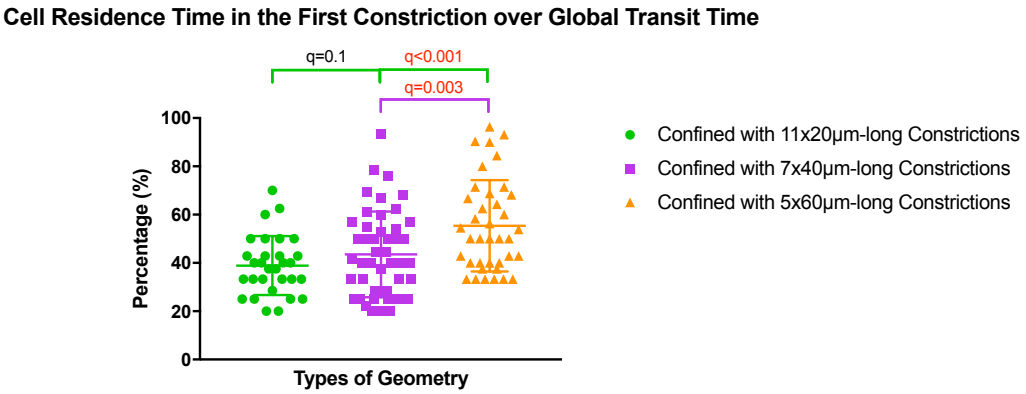

Figure 3-22. A categorical scatter plot of the percentage of cell residence time of MDA-MB-231 cells in the first constriction over the global transit time. Confined with 11x20μm-long constrictions: 15μm height (n=30), confined with 7x40μm-long constrictions: 15μm height (n=47) and confined with 5x60μm-long constrictions: 15μm height (n=38). Error bars represent standard deviation. Q values from Kruskal-Wallis test with multiple hypothesis correction (two-stage linear step-up procedure of Benjamini, Krieger and Yekutieli), and significance and confidence level at 0.05. Q values in red denote significant values.

The global transit time of MDA-MB-231 cells was significantly different when compared to each other amongst the three types of channels with constrictions. The mean global transit times of MDA-MB-231 cells transiting through micro channels at 100 mBar were 73.3 ms for confined with 11 x 20 μm-long constrictions, 95.5 ms for confined with 7 x 40 μm-long

constrictions and 219 ms for confined with 5 x 60 µm-long constrictions. The transit time of the first constriction of MDA-MB-231 cells was significantly different too when compared to each other amongst the three types of channels with constrictions. The mean transit times of the first constriction of MDA-MB-231 cells were 33.7 ms for confined with 11 x 20 µm-long constrictions, 52.3 ms for confined with 7 x 40 µm-long constrictions and 172 ms for confined with 5 x 60 µm-long constrictions. The percentage of cell residence time in the first constriction over the global transit time in the confined with 5 x 60 µm-long constrictions was significantly increased compared to confined with 11 x 20 µm-long constrictions ($q<0.001$) and confined with 7 x 40 µm-long constrictions ($q=0.003$). The percentages of cell residence time in the first constriction over the global transit time were 38.9% for confined with 11 x 20 µm-long constrictions, 43.6% for confined with 7 x 40 µm-long constrictions and 55.4% for confined with 5 x 60 µm-long constrictions.

3.4 Discussion

Flow-Induced Migration Behaviour of Normal and Cancer Epithelial Cells in Micro Constrictions at Different Applied Pressures

In the initial optimisation and characterisation of the microfluidic system, two different pressures were applied on SK-BR-3 and MDCK II cells. The aim was to observe if there was a relation between the two different applied pressures on the flow-induced migration of each type of cells in micro constrictions. Another aim was also to compare acquired results between two types of epithelial cells of cancer and normal origins.

Indeed, for breast cancer SK-BR-3 cells, the mean velocity of cells at 15 mBar (1.78 mm/s) was significantly increased ($p<0.001$) as compared to the mean velocity of cells at 10 mBar (0.05 mm/s) as shown in the above Figure 3-5. Similarly, the mean global transit time (Figure 3-6) and the mean transit time across the first constriction (Figure 3-7) at 15 mbar (1.42 s and 1.37 s respectively) were significantly decreased ($p<0.001$) as compared to the mean values obtained at 10 mbar (29.8 s and 26.2 s respectively). This intuitively means that this pressure range falls within the dynamic range of the force-deformation response of SK-BR-3 cells. However, the mean percentages of cell residence time in the first constriction over the mean global transit time (Figure 3-8) between 10 mBar (80.6%) and 15 mBar (79.3%) was insignificantly different ($p=0.397$). Despite of the difference in applied pressures, one thing that remains stark is the high residence time of cells, particularly in the first constriction before they accelerate out of the channel (Figure 3-3B and Figure 3-4). High residence times in the first constriction could mean that the cells needed time to deform in order to conform to the mechanical constraint of the constriction and to exit the constriction. Once deformed

by the mechanical constraint of the first constriction, the cells did not require the same time to cross the subsequent constrictions. This could mean that SK-BR-3 cells are deformable, but also plastic, and display a characteristic time of morphological recovery after deformation higher than the time needed to cross the path between two successive constrictions.

The following Figure 3-23 and Figure 3-24 is a time-lapse of a SK-BR-3 cell and a MDCK II cell crossing an unconfined channel (20 µm height) with 7 x 40 µm-long constrictions at 15 mBar respectively.

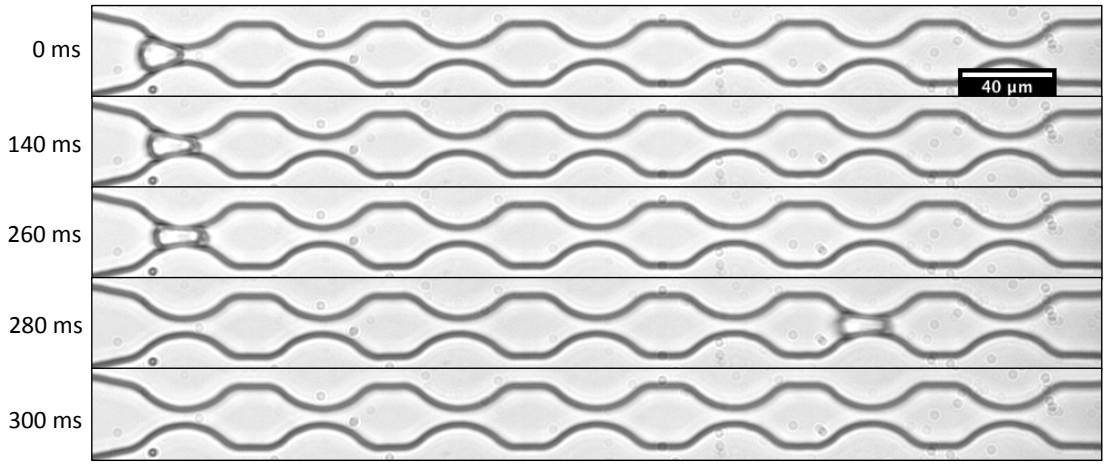

Figure 3-23. A time-lapse of a SK-BR-3 cell crossing an unconfined channel with 7x40µm-long constrictions at 15 mBar. Channel has a height of 15µm. Image acquisition at 50 frames per second.

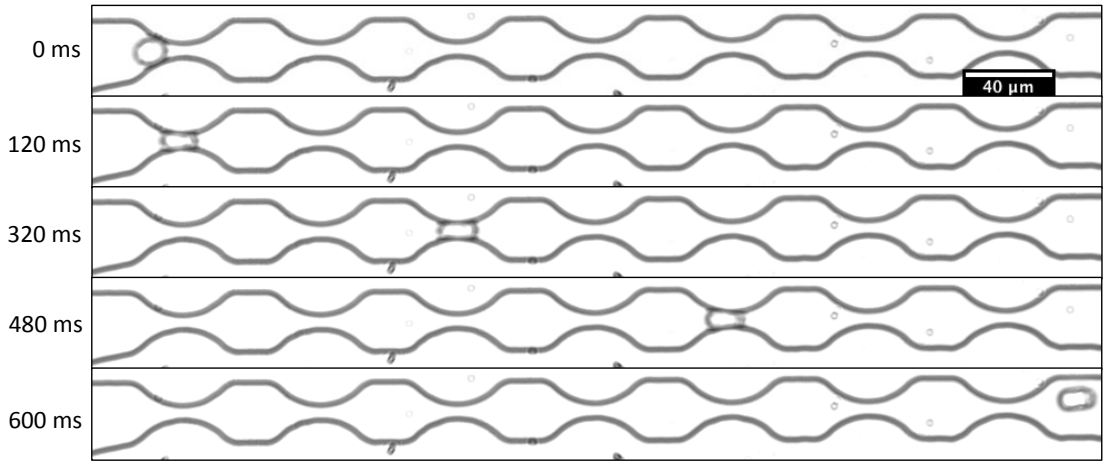

Figure 3-24. A time-lapse of a MDCK II cell crossing an unconfined channel with 7x40µm-long constrictions at 15 mBar. Channel has a height of 15µm. Image acquisition at 50 frames per second.

On the contrary, MDCK II normal kidney tubule cells, behaved quite the reverse. The velocity (Figure 3-11), global transit time (Figure 3-12) and transit time across the first constriction (Figure 3-13) of MDCK II cells at 15 mBar (0.4 mm/s, 1.72 s and 0.81 s respectively) were all insignificantly different as compared to those at 20 mBar (0.52 mm/s, 1.82 s and 1.21 s). In other terms, these results show that the difference in applied pressures is insufficient for MDCK II cells to experience any significant changes in their flow-induced migration behaviour. However, the percentage of cell residence time in the first constriction over the global transit time (Figure 3-14) at 20 mBar (39.3%) was significantly increased ($p=0.03$) compared to that at 15 mBar (26.6%). This could mean that the transit time across the first constriction for MDCK II cells is dependent of the pressures that have been applied. Even though considerably high values of residence time in the first constriction relative to the global transit times were reported at 15 mBar and 20 mBar (Figure 3-14), MDCK II cells (Figure 3-25) were slowed down by the next constrictions, unlike SKBR3 cells (Figure 3-24). MDCK II mean velocities were 0.4 mm/s and 0.52 mm/s at 15 mBar and 20 mBar respectively, as compared to SK-BR-3 mean velocities reported as 0.05 mm/s and 1.78 mm/s at 10 mBar and 15 mBar respectively. This suggests that MDCK II cells recover their shape faster than SKBR3, and thus have less plastic deformation. It was reported using atomic force microscopy that normal kidney cells are much stiffer than their cancer counterparts.[112] Hence, this also suggests that MDCK II cells are more rigid and less accommodating to mechanical constraint of the constrictions than SK-BR-3 cells.

Additionally, the projected surface area of MDCK II cells was measured before, during and after exiting the constrictions. The projected surface areas of MDCK II cells significantly decreased during the initial constriction and significantly increased after exiting the last

constriction for both 15 mBar and 20 mBar when compared to the projected surface area of MDCK II cells before entering the initial constriction (Figure 3-15). The microfluidic model used for the analysis of the projected surface area of MDCK II cells were unconfined channels with a 20 μm height. As the cells range in size from 15 to 20 μm, they were only confined in one dimension, which was from the width of the constrictions but not the height. It is understandable that the surface area decreased during the constriction as the cells were confined. Furthermore, the surface area is only a two-dimensional measurement. A three-dimensional measurement would be a more accurate method to ascertain the amount of space the cell actual took up during the constriction. Hence, even if there was an increase in projected surface area after exiting the constrictions, it could mean that the cells were flattened from the mechanical constraint in one dimension. As the height of the channels was not exactly confining the cells, this could allow the cells to orientate randomly. Therefore, it could be possible that the orientation of the cells in the channels could affect the measured projected surface area. Nonetheless, assuming that the cells had regained full shape recovery after the constrictions, the measured increase in projected surface area could be significant. If such were the case, it would mean that the increase in projected surface area was due to a morphological and swelling behaviour. Once again, this could only be ascertained with the volumetric measurements of the cells before, during and after exiting the constrictions, which were missing here but should be addressed in the perspectives of this thesis. Moreover, from these current experiments, the high velocity of cells transiting through the channels makes the measuring of cell-shape recovery challenging. A different kind of system has to be fabricated and optimise in order to trap and monitor the cells before, during and after constrictions for the precise measurements of full cell-shape recovery. This current limitation was primarily the reason why the projected surface area of SK-BR-3 was not presented. This is due to the

fact that it could not be measured precisely because the cells transited out of the channels and away from the measurable field-of-view too rapidly for image acquisition.

Flow-Induced Migration Behaviour of Two Types of Breast Cancer Cells in Micro Constrictions of Different Types of Geometry at Constant Applied Pressure

Five types of geometric microfluidic devices were fabricated. Two of these types served as controls. The unconfined (20 μm height) channel without constrictions served as a control for circulation and the confined (15 μm height) channel without constrictions served as a control for circulation as well as mechanical constraint from one-dimensional confinement. The other three types of geometric microfluidic devices contain varying lengths of 6 μm-wide constrictions however, all of the channels are all confined (15 μm height) the same. All of these microfluidic designs were calculated for their flow resistance based on Newtonian fluid in order to estimate their flow rate at a constant applied pressure (Figure 3-16). These estimations provided an idea that the longer the constriction, the higher the flow resistance and thus, the lower the flow rate.

The following Figure 3-25 depicts SK-BR-3 and MDA-MB-231 cells in three types of geometric microfluidic devices with constrictions. The migration of all tumour cells was flow-induced at 100 mBar.

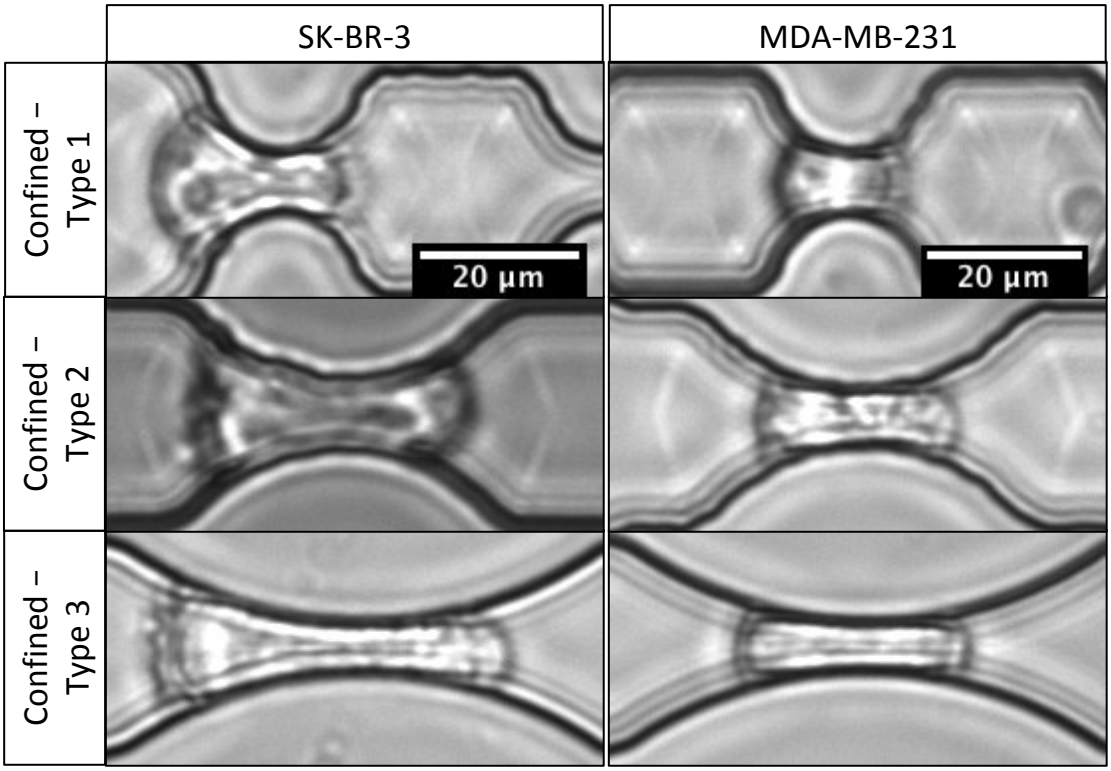

Figure 3-25. Images of SK-BR-3 (left) and MDA-MB-231 (right) cells in the constriction of different lengths of micro constrictions. Confined – type 1: with 11x20µm-long constrictions, confined – type 2: with 7x40µm-long constrictions and confined – type 3: with 5x60µm-long constrictions. All channels have a height of 15µm.

For SK-BR-3 cells, their velocity was significantly higher in both control designs when compared to all three types of channels with constrictions (Figure 3-17). Amongst the microfluidic designs with constrictions, there is only a significant decrease of velocity in the confined – type 3: with 5 x 60 µm-long constrictions compared to confined – type 1: with 11 x 20 µm-long constrictions (q=0.043). The mean velocities of SK-BR-3 cells transiting through micro channels at 100 mBar were 4.86 mm/s for confined – type 1: with 11 x 20 µm-long constrictions, 3.84 mm/s for confined – type 2: with 7 x 40 µm-long constrictions and 2.82 mm/s for confined – type 3: with 5 x 60 µm-long constrictions. Regardless of borderline statistical insignificance, the global visual observation of the data suggests a more general trend, in which a longer constriction tends to systematically induce a lower mean velocity. It could also mean that for SK-BR-3 cells, the geometry of confined – type 3 is sufficient to significantly slow down the speed of the flow-induced migrating cells. At the same time, the

global transit time was insignificantly different amongst the three types of channels with constrictions. Likewise, the q values of the global transit times amongst the three types of channels with constrictions border along the statistical significance threshold. However, the mean transit times across the first constriction of the confined – type 2: with 7 x 40 μm-long constrictions (358 ms) and of the confined – type 3: with 5 x 60 μm-long constrictions (498 ms) were significantly increased (q=0.015) when compared to that of confined – type 1: with 11 x 20 μm-long constrictions (116 ms). Similarly, the mean percentages of cell residence time in the first constriction over the global transit time in the confined – type 2: with 7 x 40 μm-long constrictions (54%) and confined – type 3: with 5 x 60 μm-long constrictions (55%) were significantly increased (q=0.02 and q=0.05 respectively) when compared to that of confined with 11 x 20 μm-long constrictions (41%). This showed that the time required for cells to deform and conform to mechanical constraint of constrictions is longer in constrictions with longer lengths. Simultaneously, it is clear in Figure 3-25 that the spatial confinement of SK-BR-3 cells is much more profound in the constrictions with longer lengths. Furthermore, initial deformation and morphological conformation are crucial in the first constriction as was earlier discussed.

For MDA-MB-231 cells, their mean velocity was significantly higher in the unconfined (20 μm height) without constrictions (18.4 mm/s) when compared to confined (15 μm height) without constrictions (8.1 mm/s) and all three types of confined channels with constrictions (7.93 mm/s, 6.36 mm/s and 4.61 mm/s for type 1, type 2 and type 3 respectively). As was previously discussed, having MDA-MB-231 cells migrating faster in the unconfined channels without confinement and constrictions compared to the other types of designs is not a surprise. Furthermore, as with SK-BR-3 data, global visual observation of MDA-MB-231 data suggests a more general trend, in which a longer constriction tends to systematically

induce a lower mean velocity. Indeed amongst the microfluidic designs with different types of constrictions, the velocity of MDA-MB-231 cells was significantly different when compared to each other (Figure 3-20). Similarly, the mean global transit times of MDA-MB-231 cells were significantly different when compared amongst the three types of channels with constrictions (73.3 ms, 95.5 ms and 219 ms for type 1, type 2 and type 3 respectively). The mean transit times across the first constriction of MDA-MB-231 cells were significantly different too when compared amongst the three types of channels with constrictions (33.7 ms, 52.3 ms and 172 ms for type 1, type 2 and type 3 respectively). The percentage of cell residence time in the first constriction over the global transit time in the confined – type 3: with 5 x 60 µm-long constrictions (55.4%) was significantly increased ($q<0.001$ and $q=0.003$) compared to confined – type 1: with 11 x 20 µm-long constrictions (38.9%) and confined – type 2: with 7 x 40 µm-long constrictions respectively (43.6%). All the data show that MDA-MB-231 cells seem to follow a general trend, in which a longer constriction tends to systematically induce a lower mean velocity and thus, higher mean global transit time as well as higher mean transit time across the first constriction. As aforementioned, the spatial confinement of MDA-MB-231 cells is much more profound in the constrictions with longer lengths (Figure 3-25). Hence, the ratio of residence time to the global transit time of MDA-MB-231 cells is understandably higher in confined – type 3: with 5 x 60 µm-long constrictions. As SK-BR-3, MDA-MB-231 cells could also be deformable, plastic and can retain some form of memory during the transit time between two successive constrictions.

3.5 Conclusion

Generally, higher applied pressures lead to higher velocities of cells transiting across a channel with micro constrictions. However, this is dependable on various factors. They are mainly including but not limited to: 1) the range of pressure applied, 2) the flow resistance of the microfluidic device, 3) the length of micro constrictions, 4) types of cells, 5) sizes of cells, and 6) the interaction with other cells.

Data from MDCK II normal kidney tubule cells showed that their flow-induced migration behaviour seemed independent of the range of pressure applied (Table 3-1) while data from SK-BR-3 breast cancer cells showed that their flow-induced migration behaviour was dependent on the range of pressure applied (Table 3-2). However, further tests with a wider range of applied pressures would be necessary to ascertain such claims.

Parameters	15 mBar	20 mBar	Significance
Velocity (mm/s)	0.4	0.52	p=0.228 (ns)
Global Transit Time (s)	1.72	1.82	p=0.228 (ns)
Transit Time across the First Constriction (s)	0.81	1.21	p=0.247 (ns)
Transit Time (1st Constriction) / Transit Time (Global) (%)	26.6	39.3	p=0.03 (*)

Table 3-1 | Summary of MDCK II Data from One Type of Microfluidic Geometry (Unconfined with 10-parallel Channels of 7x40µm-long Constrictions).

Parameters	10 mBar	15 mBar	Significance
Velocity (mm/s)	0.05	1.78	p<0.001 (***)
Global Transit Time (s)	29.8	1.42	p<0.001 (***)
Transit Time across the First Constriction (s)	26.2	1.37	p<0.001 (***)
Transit Time (1st Constriction) / Transit Time (Global) (%)	80.6	79.3	p=0.397 (ns)

Table 3-2 | Summary of SK-BR-3 Data from One Type of Microfluidic Geometry (Unconfined with 10-parallel Channels of 7x40µm-long Constrictions).

The major difference between the data of MDCK II and SK-BR-3 is the higher percentages of cell residence time in the first constriction over the global transit time for SK-BR-3 than for MDCK II. Such higher difference for SK-BR-3 cells suggest that they require more time to deform in order to conform to the mechanical constraint of the constriction and to exit the constriction. In addition, due to a characteristic relaxation time higher than the time required to reach the next constriction, the deformed shapes of the cells allow them to encounter all the subsequent constrictions without arrest, or with only a minor slowing down. This could mean that SK-BR-3 cells are deformable, plastic and can retain some form of morphological memory. On the other hand, MDCK II cells appear more rigid and less accommodating to mechanical constraint of the constrictions. Therefore, they get slowed down much more frequently than SK-BR-3 in the subsequent constrictions. This could mean that normal MDCK II cells compared to cancerous SK-BR-3 cells are less deformable and less plastic.

Here, data from SK-BR-3 (Table 3-3) and MDA-MB-231 (Table 3-4) breast cancer cells suggests a general trend, in which a longer constriction tends to systematically induce a lower mean velocity.

Parameters	11x20µm-long Constrictions	7x40µm-long Constrictions	5x60µm-long Constrictions	Kruskal-Wallis Test
Velocity (mm/s)	4.86	3.84	2.82	p<0.001 (***)
Global Transit Time (ms)	204	438	662	p=0.023 (*)
Transit Time across the First Constriction (ms)	116	358	498	p=0.017 (*)
Transit Time (1st Constriction) / Transit Time (Global) (%)	41	54	55	p=0.013 (*)

Table 3-3 | Summary of SK-BR-3 Data from Three Types of Microfluidic Geometry (Confined with 4-parallel Channels of Varying Lengths of Constrictions) at a constant applied pressure of 100 mBar.

Parameters	11x20µm-long Constrictions	7x40µm-long Constrictions	5x60µm-long Constrictions	Kruskal-Wallis Test
Velocity (mm/s)	7.93	6.36	4.61	p<0.001 (***)
Global Transit Time (ms)	73.3	95.5	219	p<0.001 (***)
Transit Time across the First Constriction (ms)	33.7	52.2	172	p<0.001 (***)
Transit Time (1st Constriction) / Transit Time (Global) (%)	38.9	43.6	55.4	p<0.001 (***)

Table 3-4 | Summary of MDA-MB-231 Data from Three Types of Microfluidic Geometry (Confined with 4-parallel Channels of Varying Lengths of Constrictions) at a constant applied pressure of 100 mBar.

The major observation here is that the time required for two types of breast cancer cells to deform and conform to mechanical constraints and constrictions is much greater in longer constrictions due to a much more profound spatial confinement. Furthermore, the initial deformation and morphological conformation are crucial during the crossing of the first constriction, which then allows smooth crossing of subsequent constrictions with minimal

arrest. From this, MDA-MB-231 cells seem to exhibit more pronounced effects than SK-BR-3 cells.

In summary, cells undergoing flow-induced migration under 3D confinement with multiple constrictions generally undergo a significant arrest at the first encounter of a constriction. Subsequently, they use up a significant amount of time to cross this first encounter. Once relieved from the first constriction, their subsequent crossings of constrictions of the same type are significantly faster. This suggests a capacity to store the information of the deformation on timescales comparable to the transit time between constrictions, which in turn suggests cell plasticity. Amongst the model cells used, this effect is more pronounced for cancer-derived cell lines (SK-BR-3 and MDA-MB-231) than for the non-cancer cell line (MDCK II). Amongst the cancer-derived group, MDA-MB-231 cells seem more affected than SK-BR-3 cells. Both cell types are of epithelial breast cancer origins, but MDA-MB-231 cells exhibit a mesenchymal-like morphology while SK-BR-3 cells do not. This suggests that the epithelial-mesenchymal state of cells contribute to the difference in the flow-induced migration behaviour of cells under 3D confinement. Furthermore, these differences suggest that the flow across constrictions may be used as an additional functional assay for the status of cancer cells.

The mechanical phenotype of cells is emerging as a potential biomarker for cell types ranging from pluripotent stem cells to cancer cells. Many studies have reported the usage of microfluidic devices to measure the mechanical phenotypes of cells including transit time, entry time, cell size, elastic modulus and cell fluidity.[83,113–115] This could be applied to dissociated cells from tumours while keeping in line with previously proposed deformation assays[116,117]. Hence, this could be particularly interesting with CTCs as they indeed undergo

in vivo constraints similar to those applied in the microfluidic *in vitro* system that has been presented here. Nonetheless, to become fully operational, this approach will require the upfront coupling with a method for sorting CTCs that provides a high state of purity and integrity.[24] Yet, this still remains an experimental challenge. Moreover, transit times for instance can span several orders of magnitude and vary from day to day within a population of single cells, which makes it challenging to characterise different cell samples based on transit time data.[118] Experimental factors may also affect the width of transit time distributions. For example, the entry velocity of cells into micron-scale patterns depends on channel surface properties as well as the pressure drop across a cell. Therefore, diligent experimental planning and compromises have to be made in studying single cell mechanical phenotyping using microfluidic devices as tools until the technology gets more advanced in addressing these types of experimental purposes.

Apart from their potential as a new biomarker for cancer cell characterisation, these types of studies also bear a potential for improving our understanding of the metastatic process. The mechanical geometries applied here are reminiscent of those encountered by CTCs during circulation in the blood micro capillaries, which can be used to address the question of the role of such mechanical constraints and constrictions in the metastatic invasiveness of CTCs.

First, mechanical constraints and constrictions were shown to induce arrest or deceleration of cells, in a manner that is dependent on the geometry of the constriction and on the cell type. It is reasonable to expect that the extravasation process requires some time, and that cells arrested at a constriction would have more chances to explore mechanical and biochemical routes across the endothelium of the micro vessels. This is somewhat different from the

general proposed view for cancer invasion and intravasation, in which a high deformability stemming from a transition to a mesenchymal state is supposed to favour invasion.[73,119,120]

Second, even at the simplest level of cell shape, the observation that cancer cells crossing constrictions retain a memory of this event, which also seems to depend on their initial cell type, raises the question of the transformations that such crossing may induce changes in cells at the molecular level. As aforementioned in Chapter One, one may question the potential effects of these changes on the long-term phenotype of these cells, notably the possibility to alter their epithelial-to-mesenchymal state, and more generally, on their ability to cross epithelial barriers, nest in tissues, evade immune responses, and proliferate.

To address these questions, the phenotyping investigation of the cells at the molecular levels, during and after crossing of mechanical constraints and constrictions will be proposed in the following chapters.

CHAPTER FOUR: INDIRECT IMMUNOFLUORESCENCE CHARACTERISATION OF TUMOUR CELLS AFTER FLOW-INDUCED MIGRATION IN MICRO CONSTRICTIONS

4.1 Introduction

The survival of CTCs in the microcirculation is a predisposing factor for metastatic dissemination.[45] Following the progress of technologies for CTC enrichment during the last two decades, CTC counts are used as predictive markers of metastatic potential and prognostic markers of survival in cancer patients.[121,122] Furthermore, the relationship between the level of CTC counts and patients' therapeutic response has been established in clinical settings.[18,123] Nonetheless, little is known about how CTCs surviving mechanisms develop while in the blood microcirculation to form distant metastases.

As previously discussed, the "mechanical" hypothesis explains how the lodgement and trapping of CTCs in the first capillary bed encountered is based on the anatomical structure and flow pattern of the microcirculation.[14,60] An *in vivo* study using a zebrafish embryo model has also shown the occurrence of CTC arrest and extravasation through the manipulations of blood flow forces.[61] However, an in depth mechanical characterisation of CTCs is still lacking. Many studies have characterised the mechanical features of cells through spontaneous migration using micro channels.[99,124,125] Not neglected but still impoverished is the mechanical characterisation of cells through flow-induced migration in micro constrictions that mimics the anatomical environment of CTCs in the microcirculation.

With more concern, it has been documented that enhanced capability of DNA damage repair in CTCs of spontaneous migration not only result in genomic instability and tumour progression[126] but also leads to tumour resistance to DNA-damaging therapies.[127,128] These findings might explain one of the surviving mechanisms of CTCs in the microcirculation. In breast cancer, DNA-damaging agents are commonly used as chemotherapeutic drugs.[129,130] As CTCs have been shown to be capable of enhancing DNA damage repair, they pose a

significant obstacle for these drugs to efficiently eradicate them and disseminated tumour cells.[131] Therefore, the need to understand DNA damage repair in CTCs rises and that it is important to verify if similar events occur in flow-induced migration.

Here, data presented examined the nuclear and cellular morphologies of breast tumour cells that have been circulated by calculated flow induction in micro channels consisting of different geometries of mechanical constraints. Further data examining their DNA damage repair capability are also presented.

4.2 Aims

The objective of this experiment is to characterise the morphological features of tumour cells immediately after being subjected to circulation, confinement and constrictions within the microfluidic system. SK-BR-3 and MDA-MB-231 breast tumour cells are isolated from the microfluidic system and techniques of immunofluorescence are applied on them.

1) To test the effects of fluid shear stress from circulation, tumour cells are circulated in a microfluidic model with channels that do not contain any confinement and constrictions in order to establish baseline readouts. Each channel is 420 μm in total length with a height of 20 μm and a width of 26 μm.

2) To test the combined effects of fluid shear stress from circulation and the effects of mechanical constraint from one-dimensional confinement in the vertical direction, tumour cells are circulated in a microfluidic model with channels that do not contain any constrictions. Each channel is 420 μm in total length with a height of 15 μm and a width of 26 μm.

3) To test the combined effects of fluid shear stress from circulation and the effects of mechanical constraint from two-dimensional confinement in the vertical and horizontal directions, tumour cells are circulated in a microfluidic model with channels that contain both confinement and constrictions. Each channel is 420 μm in total length with a height of 15 μm and multiple 6 μm-wide constrictions spaced apart by 26 μm-wide chambers that are 20 μm in length.

4) To test the combined effects of fluid shear stress from circulation and the prolonged effects of mechanical constraint from two-dimensional confinement in the vertical and horizontal directions, three types of microfluidic models with increasing length of 6 μm-wide constrictions are utilised. Type one contains 11 x 20 μm-long constrictions. Type two contains 7 x 40 μm-long constrictions. Type three contains 5 x 60 μm-long constrictions.

5) To measure the possible extents of DNA damage response to fluid shear stress alone and the combination of fluid shear stress and mechanical constraints, tumour cells from all of the above are stained and enumerated for γ-H2AX.

4.3 Results

As previously discussed, CTCs are cells shedding from primary tumours into the circulation.[23] EMT is the phenomenon proposed in which these cells acquire to migrate through tissues, escape the endothelium and invade the bloodstream.[44] Therefore, it is reasonable to expect that CTCs have had undergone EMT or are still continuously undergoing the transition while in the circulation.[132]

As positive controls, SK-BR-3 and MDA-MB-231 breast tumour cells were treated with 10 ng/ml of TGFβ1 for 24 hours to induce or boost EMT. The negative controls for TGFβ1 were untreated cells. These two groups of cells comprised the uncirculated group that functioned as controls for cells that were circulated in the microfluidic system. The circulated group comprised two sub groups of cells that were circulated in the microfluidic system with varying channel heights: 1) unconfined and 2) confined. Both the uncirculated and circulated groups of cells were stained with DAPI in order to characterise their nuclear morphologies. Their nucleus area (Figure 4-1A and Figure 4-4A), nucleus length (Figure 4-2A and Figure 4-5A) and nuclear to cytoplasmic (NC) ratio (Figure 4-3A and Figure 4-6A) are presented respectively for SK-BR-3 and MDA-MB-231 cells.

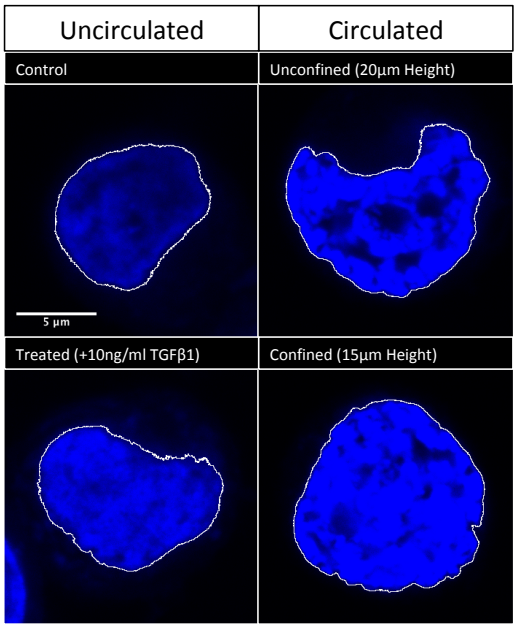

Figure 4-1A. DAPI staining of SK-BR-3 cells uncirculated (without fluid shear stress) and circulated (with fluid shear stress) outlined with the nucleus' region of interest.

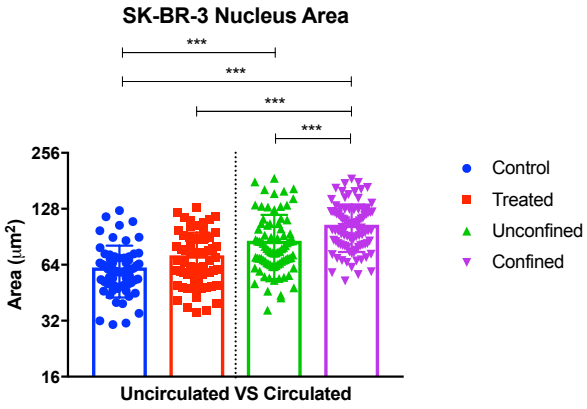

Figure 4-1B. Nucleus area of SK-BR-3 cells in $\log_2$ scale. Control (blue, n=65), post-EMT-induction by TGFβ1 treatment (red, n=65), post-circulation in an unconfined micro channel (green, n=84), and post-circulation in a confined micro channel (purple, n=92). Error bars represent standard deviation. Kruskal-Wallis test ($p<0.001$) and Dunn's multiple comparisons post hoc test.

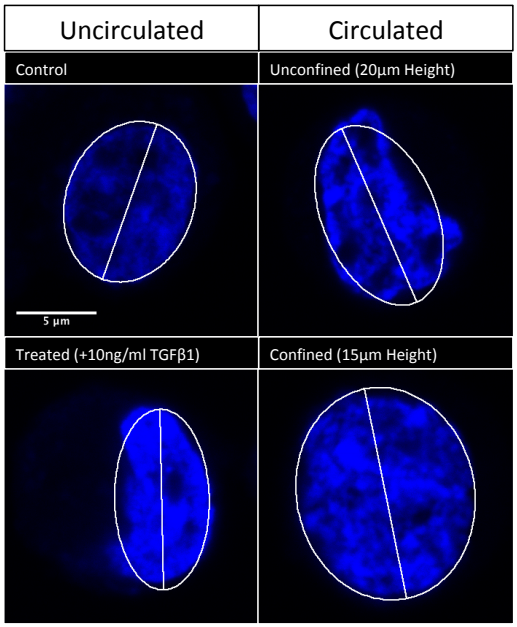

Figure 4-2A. DAPI staining of SK-BR-3 cells uncirculated (without fluid shear stress) and circulated (with fluid shear stress). Superimposed on the nucleus is the longer axis of a fitted ellipse.

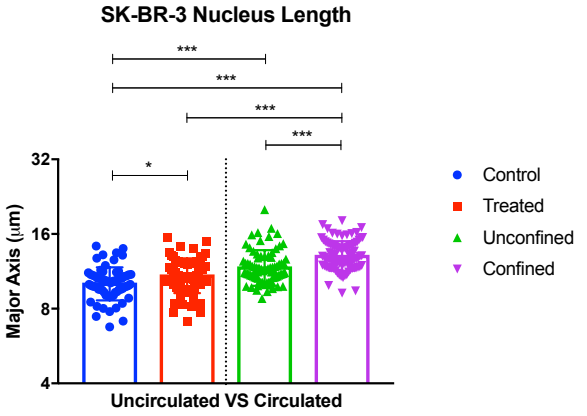

Figure 4-2B. Nucleus length of SK-BR-3 cells in $\log_2$ scale. Control (blue, n=65), post-EMT-induction by TGFβ1 treatment (red, n=65), post-circulation in an unconfined micro channel (green, n=84), and post-circulation in a confined micro channel (purple, n=92). Error bars represent standard deviation. Kruskal-Wallis test ($p<0.001$) and Dunn's multiple comparisons post hoc test.

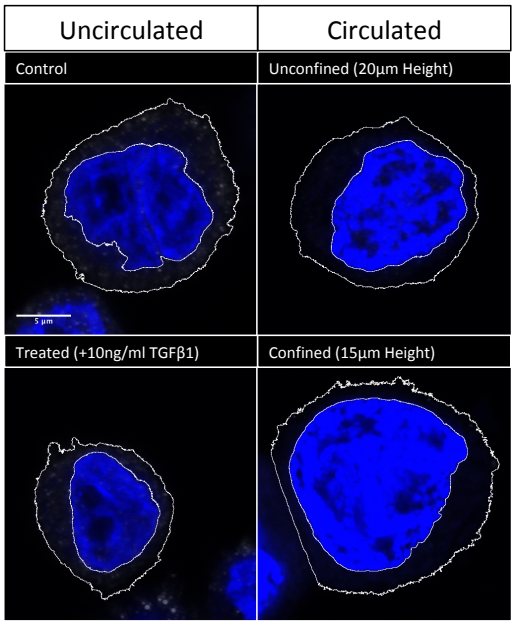

Figure 4-3A. DAPI staining of SK-BR-3 cells uncirculated (without fluid shear stress) and circulated (with fluid shear stress) outlined with the nucleus' and cell's region of interest.

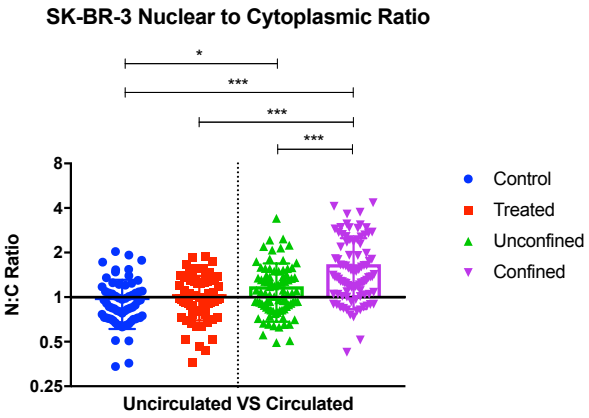

Figure 4-3B. Nuclear to cytoplasmic ratio of SK-BR-3 cells in log_2 scale. Control (blue, n=65), post-EMT-induction by TGFβ1 treatment (red, n=65), post-circulation in an unconfined micro channel (green, n=84), and post-circulation in a confined micro channel (purple, n=92). Error bars represent standard deviation. Kruskal-Wallis test ($p<0.001$) and Dunn's multiple comparisons post hoc test.

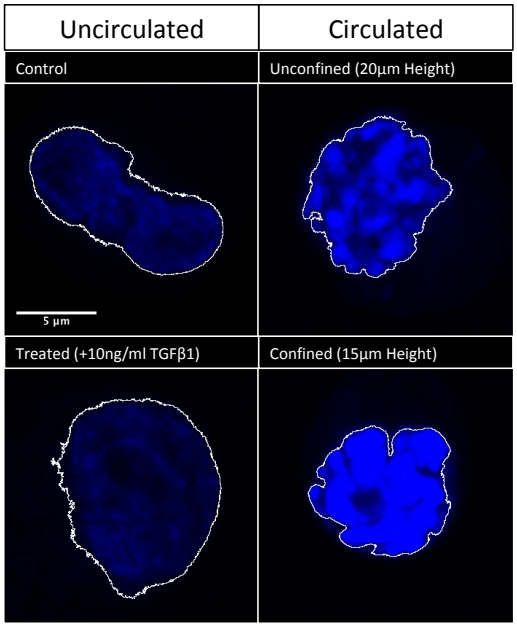

Figure 4-4A. DAPI staining of MDA-MB-231 cells uncirculated (without fluid shear stress) and circulated (with fluid shear stress) outlined with the nucleus' region of interest.

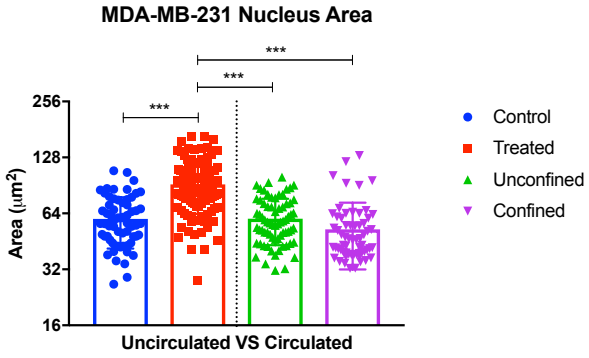

Figure 4-4B. Nucleus area of MDA-MB-231 cells in log_2 scale. Control (blue, n=63), post-EMT-induction by TGFβ1 treatment (red, n=121), post-circulation in an unconfined micro channel (green, n=70), and post-circulation in a confined micro channel (purple, n=62). Error bars represent standard deviation. Kruskal-Wallis test ($p<0.001$) and Dunn's multiple comparisons post hoc test.

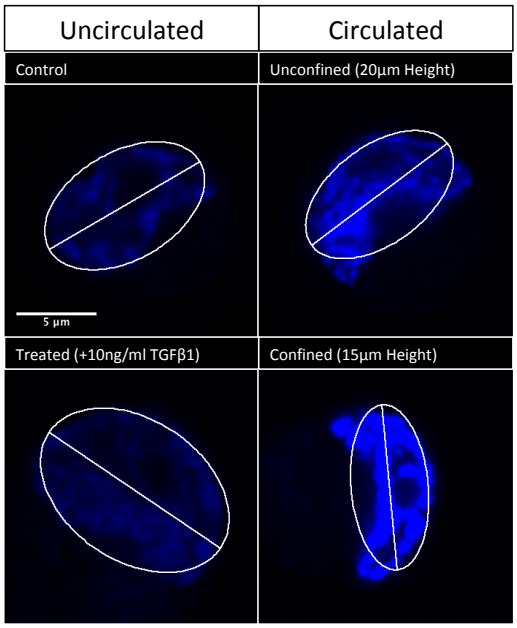

Figure 4-5A. DAPI staining of MDA-MB-231 cells uncirculated (without fluid shear stress) and circulated (with fluid shear stress). Superimposed on the nucleus is the longer axis of a fitted ellipse.

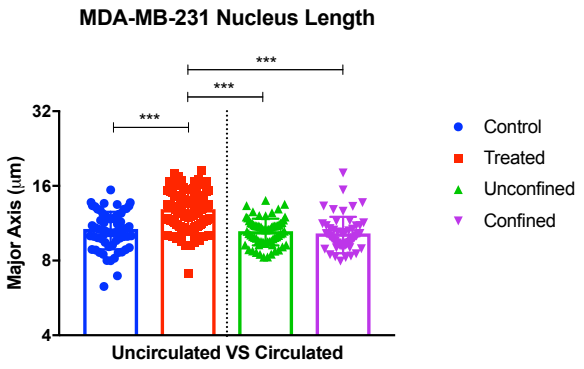

Figure 4-5B. Nucleus length of MDA-MB-231 cells in $\log_2$ scale. Control (blue, n=63), post-EMT-induction by TGFβ1 treatment (red, n=121), post-circulation in an unconfined micro channel (green, n=70), and post-circulation in a confined micro channel (purple, n=62). Error bars represent standard deviation. Kruskal-Wallis test ($p<0.001$) and Dunn's multiple comparisons post hoc test.

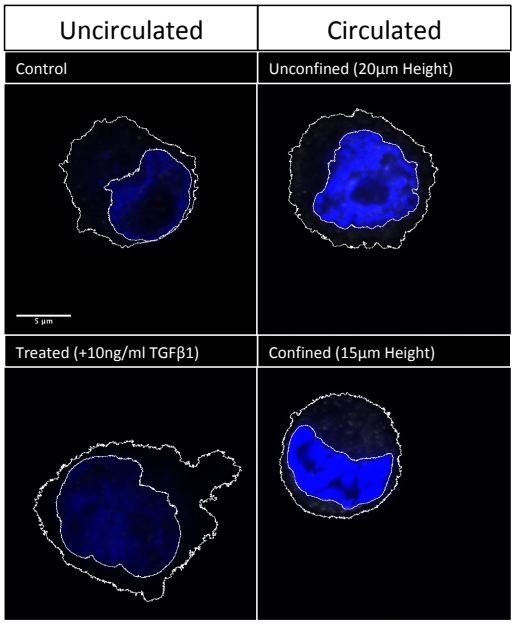

Figure 4-6A. DAPI staining of MDA-MB-231 cells uncirculated (without fluid shear stress) and circulated (with fluid shear stress) outlined with the nucleus' and cell's region of interest.

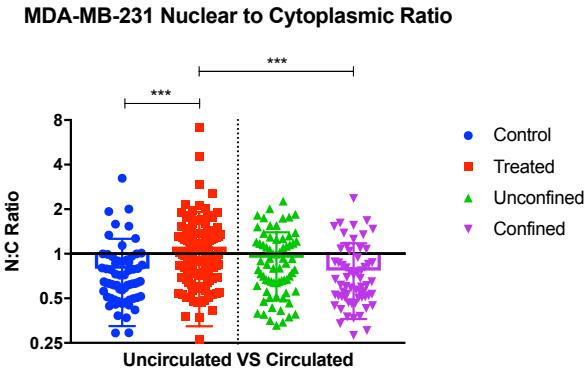

Figure 4-6B. Nuclear to cytoplasmic ratio of MDA-MB-231 cells in $\log_2$ scale. Control (blue, n=63), post-EMT-induction by TGFβ1 treatment (red, n=121), post-circulation in an unconfined micro channel (green, n=70), and post-circulation in a confined micro channel (purple, n=62). Error bars represent standard deviation. Kruskal-Wallis test ($p<0.001$) and Dunn's multiple comparisons post hoc test.

Once baseline readouts of nuclear morphologies were established from the uncirculated and circulated groups, SK-BR-3 and MDA-MB-231 cells were then circulated in the microfluidic system consisting of mechanical constraints from two-dimensional confinement in the

vertical and horizontal directions. The confinement in the vertical direction came from the channel height of 15 µm. The confinement in the horizontal direction came from the constriction width of 6 µm. The effect of confinement of cells in both directions while in circulation was investigated using several lengths of constrictions. These cells were also stained with DAPI in order to characterise their nuclear morphologies. Their nucleus area (Figure 4-7A and Figure 4-10A), nucleus length (Figure 4-8A and Figure 4-11A) and nuclear to cytoplasmic (NC) ratio (Figure 4-9A and Figure 4-12A) are presented respectively for SK-BR-3 and MDA-MB-231 cells.

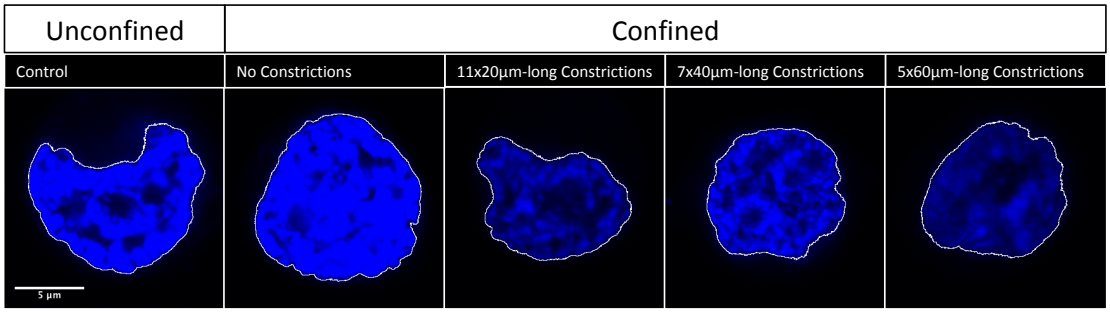

Figure 4-7A. DAPI staining of SK-BR-3 cells circulated (with fluid shear stress) in unconfined and confined environments. The outline is the nucleus' region of interest.

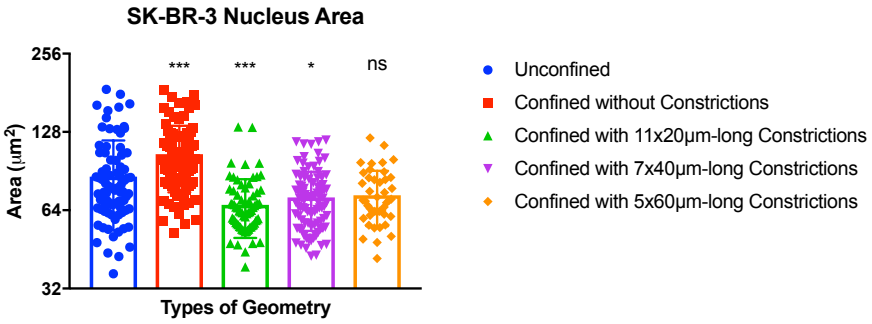

Figure 4-7B. Nucleus area of SK-BR-3 cells in $\log_2$ scale. Unconfined/control (blue, n=84), confined without constrictions (red, n=92), confined with 11x20µm-long constrictions (green, n=71), confined with 7x40µm-long constrictions (purple, n=94), and confined with 5x60µm-long constrictions (orange, n=44). Error bars represent standard deviation. Kruskal-Wallis test ($p<0.001$) and Dunn's multiple comparisons post hoc test.

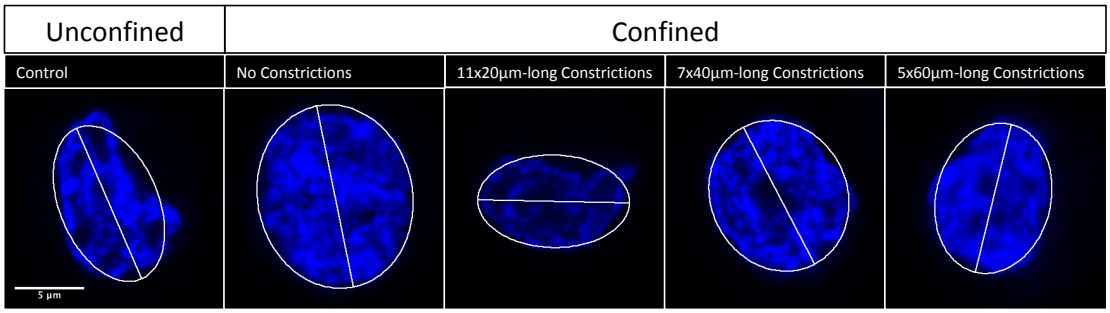

Figure 4-8A. DAPI staining of SK-BR-3 cells circulated (with fluid shear stress) in unconfined and confined environments. Superimposed on the nucleus is the longer axis of a fitted ellipse.

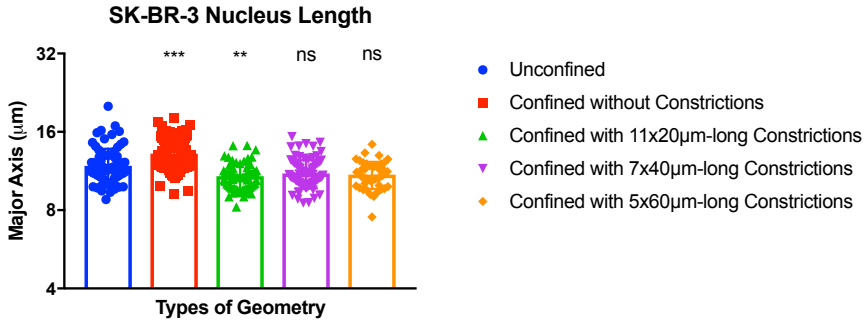

Figure 4-8B. Nucleus length of SK-BR-3 cells in $\log_2$ scale. Unconfined/control (blue, n=84), confined without constrictions (red, n=92), confined with 11x20µm-long constrictions (green, n=71), confined with 7x40µm-long constrictions (purple, n=94), and confined with 5x60µm-long constrictions (orange, n=44). Error bars represent standard deviation. Kruskal-Wallis test (p<0.001) and Dunn's multiple comparisons post hoc test.

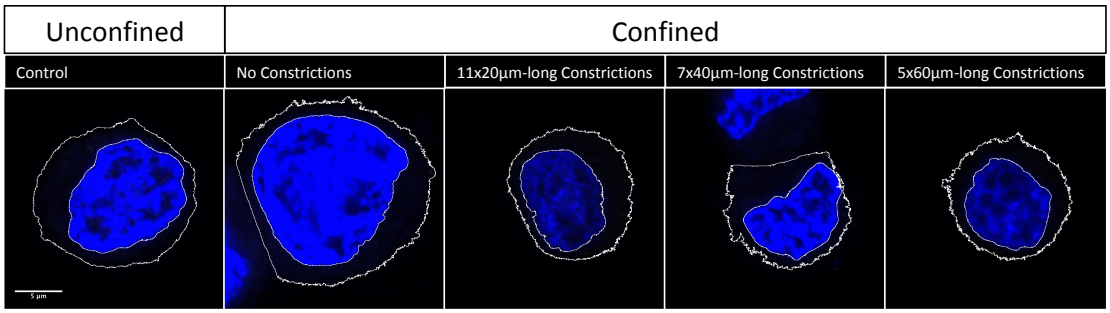

Figure 4-9A. DAPI staining of SK-BR-3 cells circulated (with fluid shear stress) in unconfined and confined environments. The outline is the nucleus' and cell's region of interest.

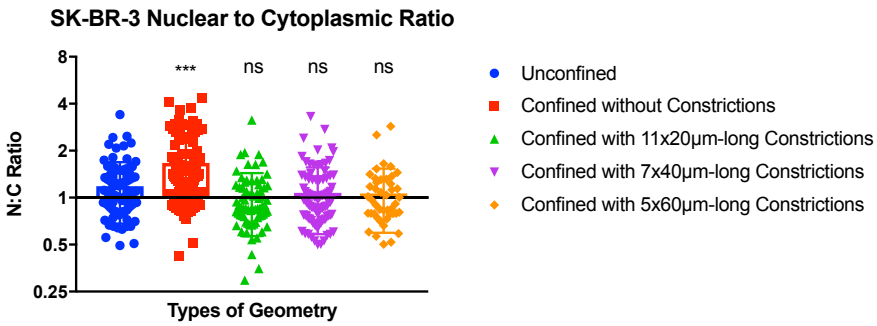

Figure 4-9B. Nuclear to cytoplasmic ratio of SK-BR-3 cells in $\log_2$ scale. Unconfined/control (blue, n=84), confined without constrictions (red, n=92), confined with 11x20µm-long constrictions (green, n=71), confined with 7x40µm-long constrictions (purple, n=94), and confined with 5x60µm-long constrictions (orange, n=44). Error bars represent standard deviation. Kruskal-Wallis test (p<0.001) and Dunn's multiple comparisons post hoc test.

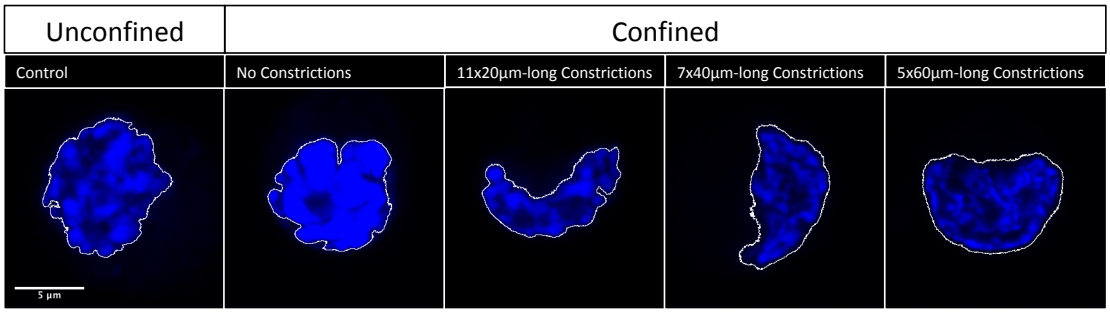

Figure 4-10A. DAPI staining of MDA-MB-231 cells circulated (with fluid shear stress) in unconfined and confined environments. The outline is the nucleus' region of interest.

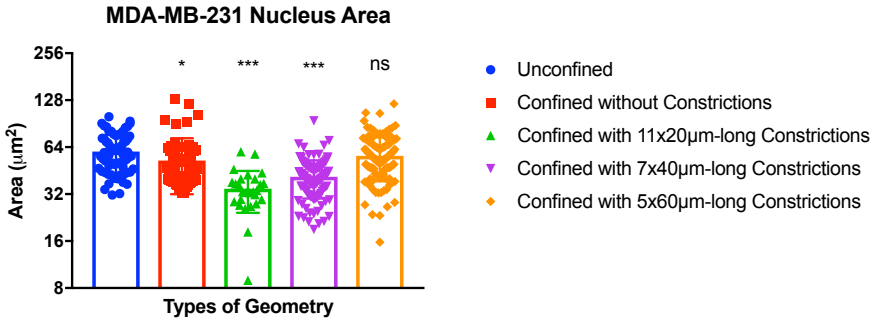

Figure 4-10B. Nucleus area of MDA-MB-231 cells in $\log_2$ scale. Unconfined/control (blue, n=70), confined without constrictions (red, n=62), confined with 11x20µm-long constrictions (green, n=27), confined with 7x40µm-long constrictions (purple, n=123), and confined with 5x60µm-long constrictions (orange, n=124). Error bars represent standard deviation. Kruskal-Wallis test ($p<0.001$) and Dunn's multiple comparisons post hoc test.

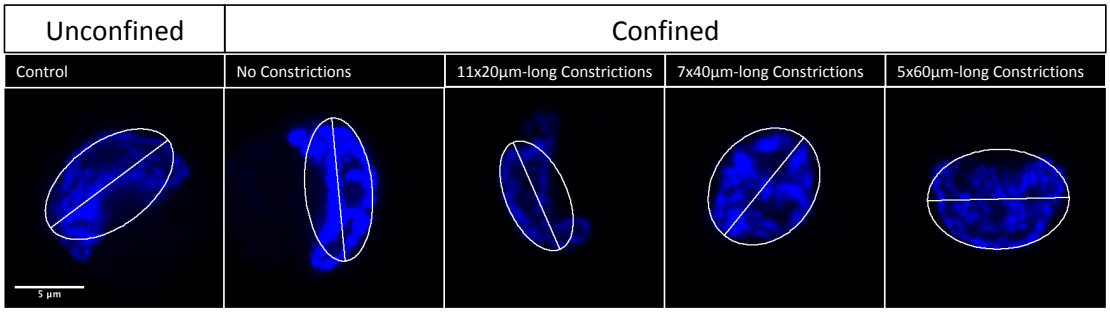

Figure 4-11A. DAPI staining of MDA-MB-231 cells circulated (with fluid shear stress) in unconfined and confined environments. Superimposed on the nucleus is the longer axis of a fitted ellipse.

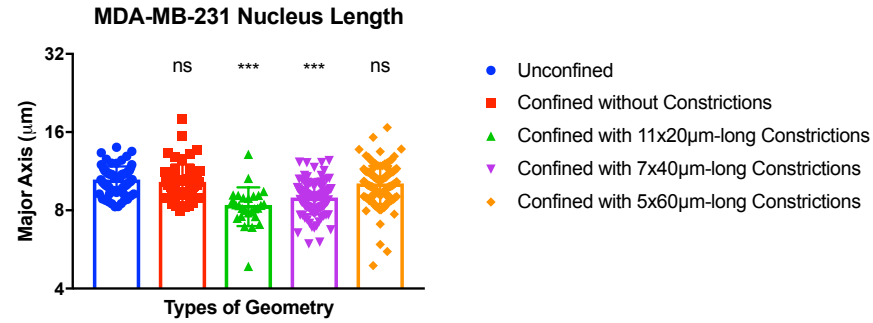

Figure 4-11B. Nucleus length of MDA-MB-231 cells in $\log_2$ scale. Unconfined/control (blue, n=70), confined without constrictions (red, n=62), confined with 11x20µm-long constrictions (green, n=27), confined with 7x40µm-long constrictions (purple, n=123), and confined with 5x60µm-long constrictions (orange, n=124). Error bars represent standard deviation. Kruskal-Wallis test ($p<0.001$) and Dunn's multiple comparisons post hoc test.

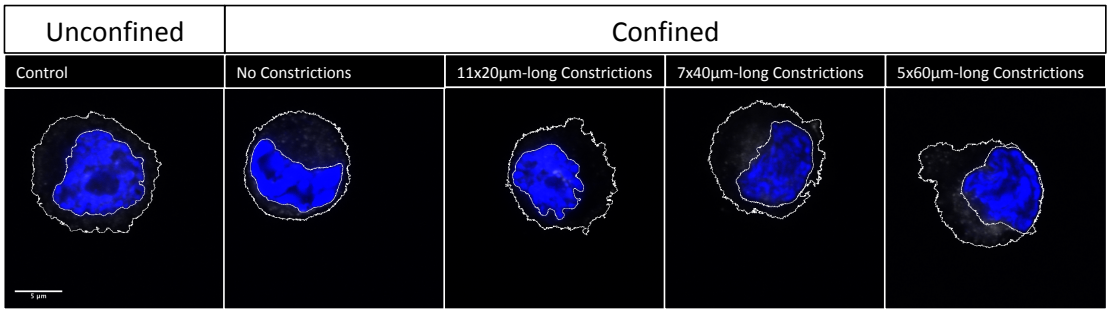

Figure 4-12A. DAPI staining of MDA-MB-231 cells circulated (with fluid shear stress) in unconfined and confined environments. The outline is the nucleus' and cell's region of interest.

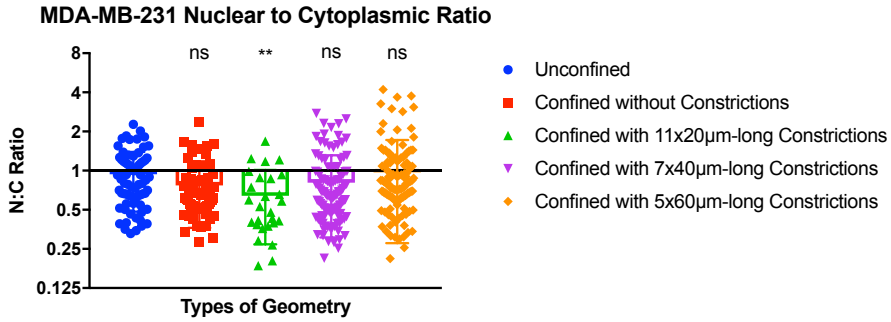

Figure 4-12B. Nuclear to cytoplasmic ratio of MDA-MB-231 in $\log_2$ scale. Unconfined/control (blue, n=70), confined without constrictions (red, n=62), confined with 11x20µm-long constrictions (green, n=27), confined with 7x40µm-long constrictions (purple, n=123), and confined with 5x60µm-long constrictions (orange, n=124). Error bars represent standard deviation. Kruskal-Wallis test ($p<0.001$) and Dunn's multiple comparisons post hoc test.

Additionally, all cells were stained using γH2AX antibody, which is a marker of DNA damage response. The γH2AX expressions detected by immunofluorescence are presented in Figure 4-13A and Figure 4-14A respectively for SK-BR-3 and MDA-MB-231 cells. The possible extents of DNA damage response were measured by comparing the immunostaining intensities between the nucleus and cytoplasm as are presented in Figure 4-13B and Figure 4-14B respectively for SK-BR-3 and MDA-MB-231 cells.

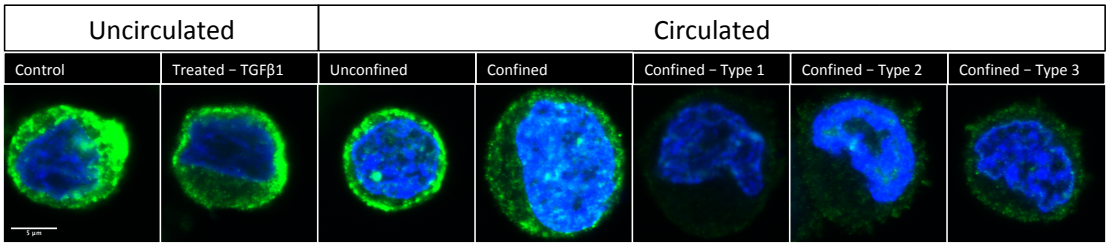

Figure 4-13A. Immunofluorescence staining of γH2AX in SK-BR-3 cells uncirculated (without fluid shear stress) and circulated (with fluid shear stress).

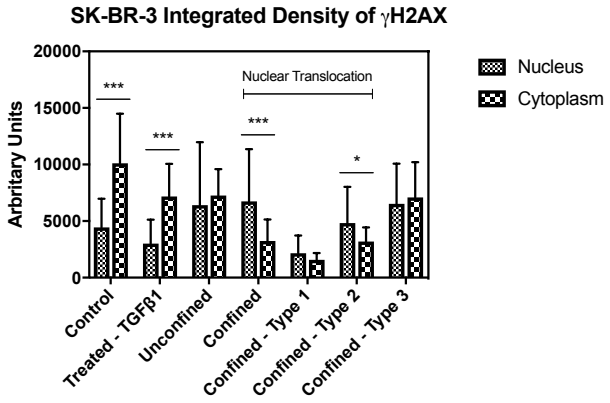

Figure 4-13B. Nuclear and cytoplasmic intensities of γH2AX immunostaining in SK-BR-3 cells uncirculated (without fluid shear stress) and circulated (with fluid shear stress). Control (n=34), treated – TGFβ1: 10ng/ml (n=34), unconfined (n=50), confined: without constrictions (n=60), confined – type 1: with 11x20µm-long constrictions (n=40), confined – type 2: with 7x40µm-long constrictions (n=61), and confined – type 3: with 5x60µm-long constrictions (n=19). Error bars represent standard deviation. Two-way ANOVA test and Sidak's multiple comparisons post hoc test.

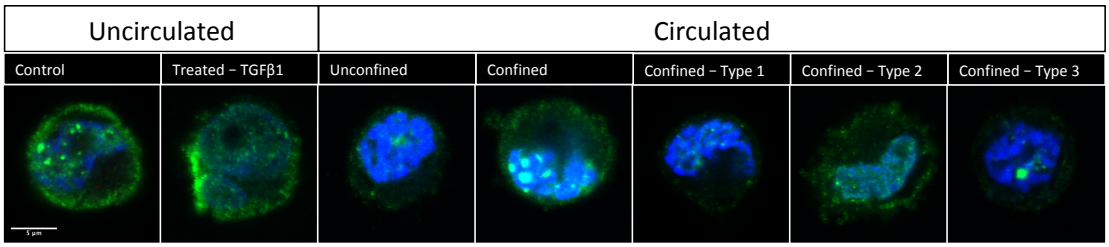

Figure 4-14A. Immunofluorescence staining of γH2AX in MDA-MB-231 cells uncirculated (without fluid shear stress) and circulated (with fluid shear stress).

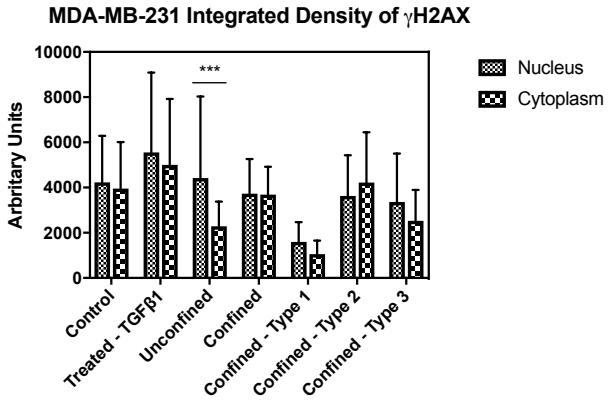

Figure 4-14B. Nuclear and cytoplasmic intensities of γH2AX immunostaining in MDA-MB-231 cells uncirculated (without fluid shear stress) and circulated (with fluid shear stress). Control (n=30), treated – TGFβ1: 10ng/ml (n=60), unconfined (n=35), confined: without constrictions (n=30), confined – type 1: with 11x20µm-long constrictions (n=24), confined – type 2: with 7x40µm-long constrictions (n=62), and confined – type 3: with 5x60µm-long constrictions (n=62). Error bars represent standard deviation. Two-way ANOVA test and Sidak's multiple comparisons post hoc test.

4.4 Discussion

TGFβ1 Treatment

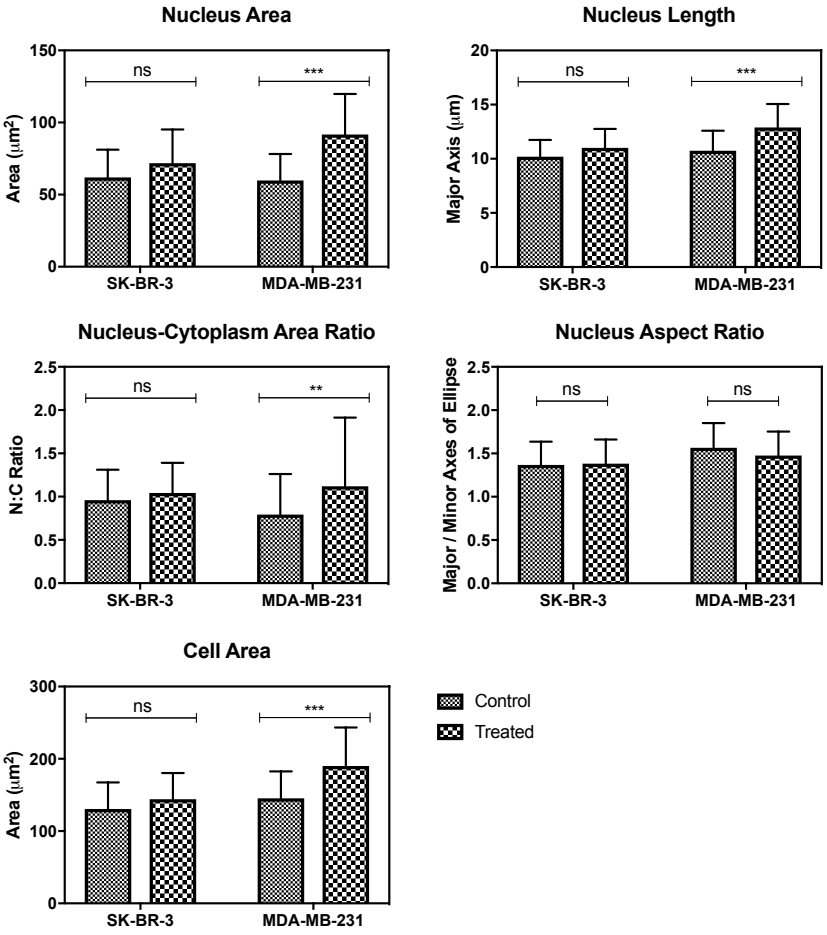

Figure 4-15. Bar charts comparing the morphology of SK-BR-3 and MDA-MB-231 post-EMT-induction by TGFβ1 treatment. SK-BR-3 control (n=65), SK-BR-3 treated (n=65), MDA-MB-231 control (n=63) and MDA-MB-231 treated (n=121). Error bars represent standard deviation. Two-way ANOVA test and Tukey's multiple comparisons post hoc test.

MDA-MB-231 cells are more responsive to TGFβ1 treatment than SK-BR-3 cells (Figure 4-15). The nucleus area ($p<0.001$), nucleus length ($p<0.001$), NC ratio ($p=0.002$) and cell area ($p<0.001$) are all significantly higher in treated versus control MDA-MB-231 cells. In contrary, the nucleus area ($p=0.082$), nucleus length ($p=0.075$), NC ratio ($p=0.848$) and cell

area ($p=0.305$) are all insignificantly different between control and treated SK-BR-3 cells. Finally, the nucleus aspect ratio between control and treated for both types of cells are insignificantly different. As collective cells in monolayer, SK-BR-3 had been shown to have major alterations in morphology with larger areas and more elongated structures in response to TGFβ1 treatment.[133] However, these results are not in agreement with the presented observations here. To understand this discrepancy, it should be re-pointed out that these cells were treated with TGFβ1 in monolayer cultures and then re-suspended after treatment as single cells before DAPI staining. This transition toward a "single cell in solution" situation might have measurable morphological consequences.

Fluid Shear Stress from Circulation

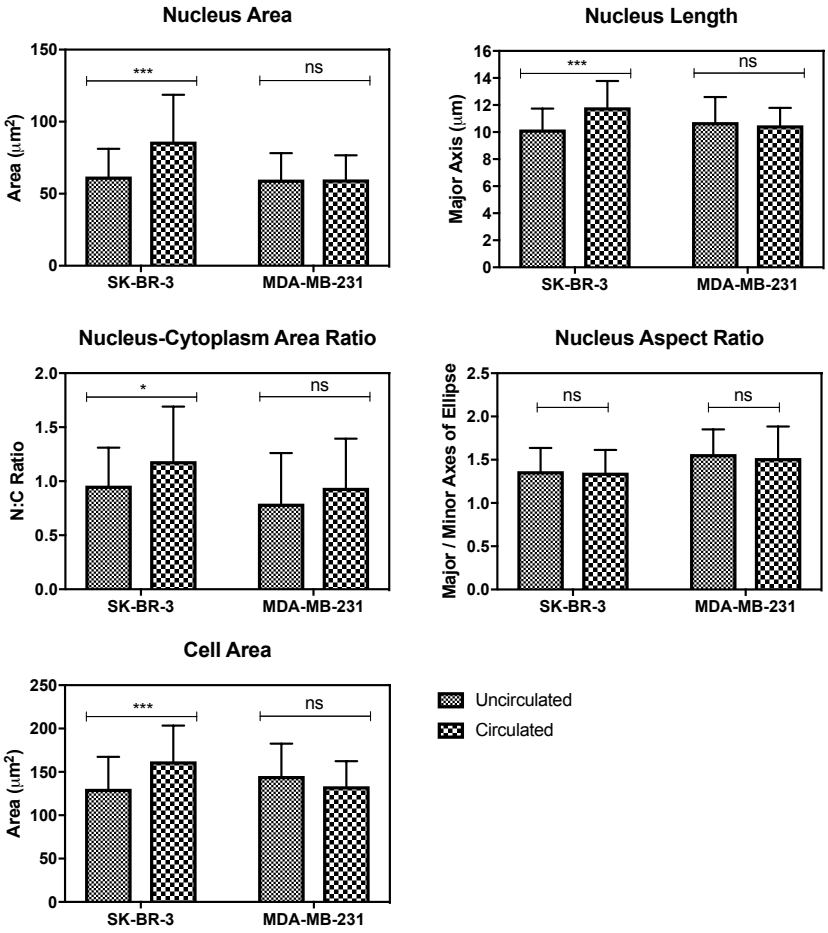

Figure 4-16. Bar charts comparing the morphology of SK-BR-3 and MDA-MB-231 post-circulation in micro channels of 20µm height. SK-BR-3 uncirculated (n=65), SK-BR-3 circulated (n=84), MDA-MB-231 uncirculated (n=63) and MDA-MB-231 circulated (n=70). Error bars represent standard deviation. Two-way ANOVA test and Tukey's multiple comparisons post hoc test.

Data on nuclear morphologies from the effect of circulation alone were established as baseline readouts. As opposed to TGFβ1 treatment, SK-BR-3 cells are more responsive to fluid shear stress than MDA-MB-231 cells (Figure 4-16). The nucleus area ($p<0.001$), nucleus length ($p<0.001$), NC ratio ($p=0.014$) and cell area ($p<0.001$) are all significantly higher between uncirculated and circulated SK-BR-3 cells. In contrary, the nucleus area ($p>0.999$), nucleus length ($p=0.846$), NC ratio ($p=0.249$) and cell area ($p=0.236$) are all

insignificantly different between uncirculated and circulated MDA-MB-231 cells. It should be noted that the nucleus area (p=0.957), nucleus length (p=0.361), NC ratio (p=0.367) and cell area (p=0.227) between uncirculated SK-BR-3 and uncirculated MDA-MB-231 cells are all insignificantly different. This ruled out the size differential factor, in which both cell types began almost as equals before circulation. While MDA-MB-231 cells seemed deformable in circulation, SK-BR-3 cells seemed to be plastic under the influence of circulation.

Mechanical Constraint from One-Dimensional Confinement

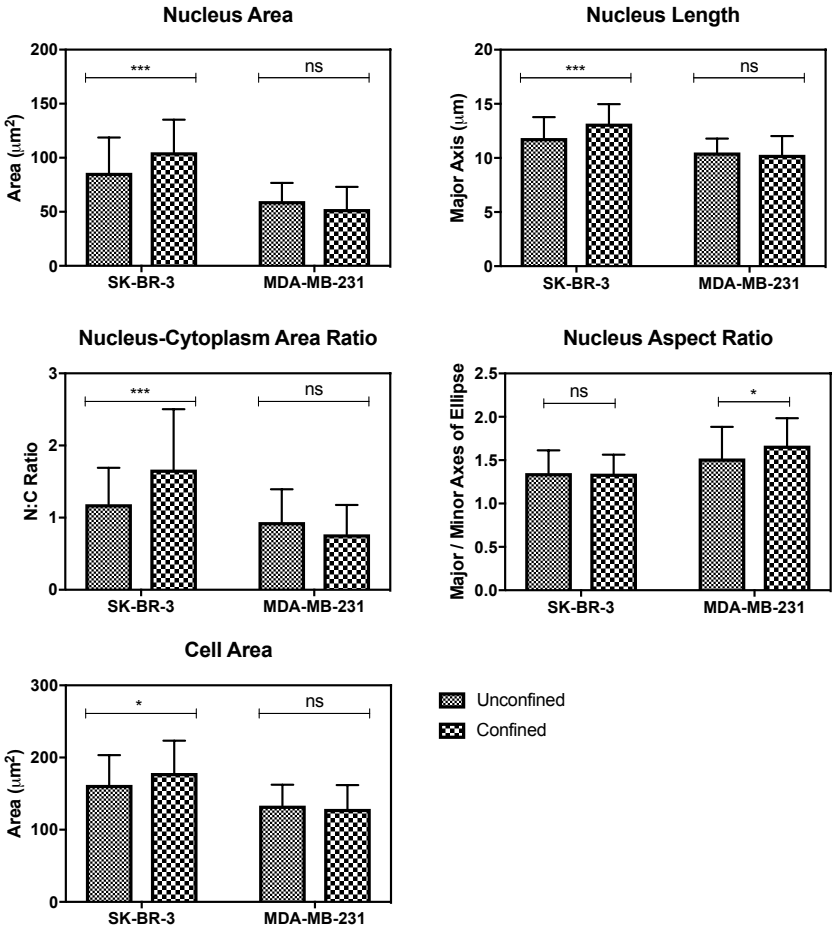

Figure 4-17. Bar charts comparing the morphology of SK-BR-3 and MDA-MB-231 post-circulation in micro channels of 20µm height (unconfined) and of 15µm height (confined). SK-BR-3 unconfined (n=84), SK-BR-3 confined (n=92), MDA-MB-231 unconfined (n=70) and MDA-MB-231 confined (n=62). Error bars represent standard deviation. Two-way ANOVA test and Tukey's multiple comparisons post hoc test.

The effect of confinement was added to the circulation factor (Figure 4-17). It was previously shown that fluid shear stress induced significant morphological alterations in SK-BR-3 cells but not in MDA-MB-231 cells (Figure 4-16). Here, SK-BR-3 cells were continuously altered morphologically when circulated and confined simultaneously. The nucleus area ($p<0.001$), nucleus length ($p<0.001$), NC ratio ($p<0.001$) and cell area ($p=0.025$) between

circulated/unconfined and circulated/confined SK-BR-3 cells are all significantly higher. Tenaciously, MDA-MB-231 cells remained resistant and unaltered to combined fluid shear stress and mechanical confinement. The nucleus area ($p=0.378$), nucleus length ($p=0.897$), NC ratio ($p=0.372$) and cell area ($p=0.908$) between circulated/unconfined and circulated/confined MDA-MB-231 cells are all insignificantly different. Nonetheless, the nucleus aspect ratio of MDA-MB-231 cells is significantly higher between circulated/unconfined and circulated/confined ($p=0.019$). The circulated/confined SK-BR-3 cells have stronger significance levels in nucleus area, nucleus length and NC ratio but weaker significance level in cell area, when compared to circulated/unconfined SK-BR-3 cells. There have been multiple analyses on the characteristics of CTCs demonstrating their broad physical heterogeneity.[19,134,135] CTCs derived from different types of tissue, or even from the same tissue, harbour large variations in size.[136,137] While most CTCs show large overall size and a high NC ratio compared to surrounding white blood cells, some CTCs show considerable size similarity with surrounding leukocytes.[138] Therefore, the strong significance level in nucleus area coupled with the weak significance level in cell area of the circulated/confined SK-BR-3 maintained a high NC ratio, which is a strong predictor of malignancy.[138]

Mechanical Constraint from Two-Dimensional Confinement

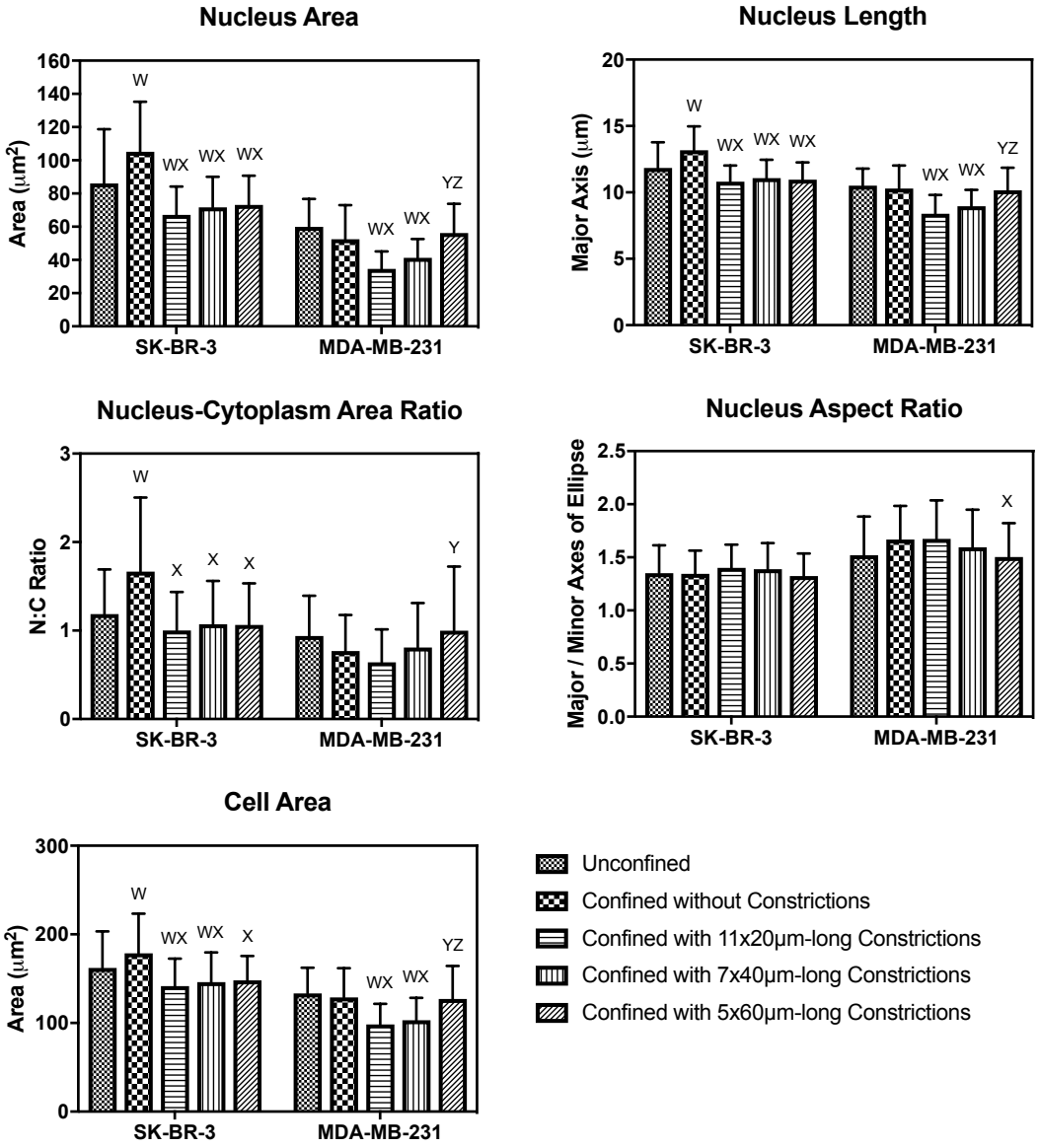

Figure 4-18. Bar charts comparing the morphology of SK-BR-3 and MDA-MB-231 post-circulation in micro channels of 20μm height (unconfined) and of 15μm height (confined) with varying types of geometry (constrictions). SK-BR-3 unconfined (n=84), SK-BR-3 confined without constrictions (n=92), SK-BR-3 confined with 11x20μm-long constrictions (n=71), SK-BR-3 confined with 7x40μm-long constrictions (n=94), SK-BR-3 confined with 5x60μm-long constrictions (n=44), MDA-MB-231 unconfined (n=70), MDA-MB-231 confined without constrictions (n=62), MDA-MB-231 confined with 11x20μm-long constrictions (n=27), MDA-MB-231 confined with 7x40μm-long constrictions (n=123), and MDA-MB-231 confined with 5x60μm-long constrictions (n=124). Error bars represent standard deviation. Two-way ANOVA test and Tukey's multiple comparisons post hoc test. (W) significantly different from unconfined, (X) significantly different from confined without constrictions, (Y) significantly different from confined with 11x20μm-long constrictions, and (Z) significantly different from confined with 7x40μm-long constrictions.

The effect of constrictions was added to both confinement and circulation factors (Figure 4-18). The nucleus area of SK-BR-3 cells that were circulated/confined with 11 x 20 μm-long constrictions ($p<0.001$, $p<0.001$), circulated/confined with 7 x 40 μm-long constrictions ($p<0.001$, $p<0.001$) and circulated/confined with 5 x 60 μm-long constrictions ($p=0.007$, $p<0.001$) are all significantly lower when compared to cells circulated/unconfined and circulated/confined without constrictions respectively. The nucleus length of SK-BR-3 cells too are significantly lower: circulated/confined with 11 x 20 μm-long constrictions ($p<0.001$, $p<0.001$), circulated/confined with 7 x 40 μm-long constrictions ($p=0.009$, $p<0.001$) and circulated/confined with 5 x 60 μm-long constrictions ($p=0.019$, $p<0.001$) are significantly lower when compared to cells circulated/unconfined and circulated/confined without constrictions respectively. However, the NC ratios of SK-BR-3 cells are insignificantly different in all three types of confined geometries with constrictions when compared to unconfined cells but are all significantly lower when compared to cells circulated/confined without constrictions: circulated/confined with 11 x 20 μm-long constrictions ($p<0.001$), circulated/confined with 7 x 40 μm-long constrictions ($p<0.001$) and circulated/confined with 5 x 60 μm-long constrictions ($p<0.001$).

Similar trend is seen in MDA-MB-231 cells, in which the readouts across all of nuclear morphologies began by decreasing in the circulated/confined with 11 x 20 μm-long constrictions before steadily increasing in the subsequent circulated/confined with 7 x 40 μm-long constrictions and circulated/confined with 5 x 60 μm-long constrictions geometries. Moreover, the nucleus aspect ratio of MDA-MB-231 cells is significantly higher only in the third type of constrictions as compared to the first type of constrictions ($p=0.013$).

The prolonged effects of constrictions might play a role in this trend. Interestingly, only MDA-MB-231 cells circulated in the most prolonged channel of constrictions (circulated/confined with 5 x 60 μm-long constrictions) showed insignificant differences in nucleus area ($p=0.757$), nucleus length ($p=0.577$), NC ratio ($p=0.952$) and cell area ($p=0.723$) when compared to cells circulated/unconfined without constrictions. The increase in distance within a constriction could be associated to faster morphological recovery of MDA-MB-231 cells. Furthermore, it could also demonstrate higher reversible deformability of MDA-MB-231 cells as compared to SK-BR-3 cells.

Extents of DNA Damage Response

DNA damage response (DDR) is a series of coordinated responses designated to remove damage incurred to the genome.[139] It is estimated that each of the approximately 10^{13} cells in the human body receives tens of thousands of DNA lesions per day.[140] These lesions can block genome replication and transcription, and they can lead to mutations or genome aberrations that may cause disease or threaten cell viability if they are not repaired or are repaired incorrectly.[141] DNA damage can occur from endogenous or exogenous agents with the vast majority incurred on the genome being endogenous.[142] The following Figure 4-19 summarises the different types of DNA damaging agents and the repair processes triggered.

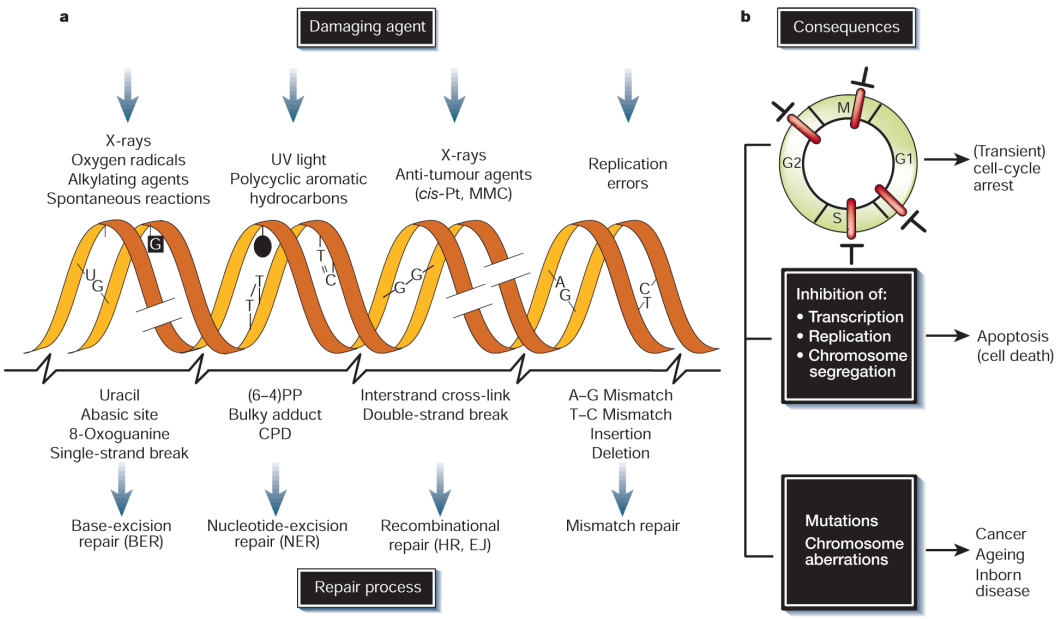

Figure 4-19 | DNA damage, repair mechanisms and consequences. a) Common DNA damaging agents (top); examples of DNA lesions induced by these agents (middle); and most relevant DNA repair mechanism responsible for the removal of the lesions (bottom). b) Acute effects of DNA damage on cell-cycle progression, leading to transient arrest in the G1, S, G2 and M phases (top), and on DNA metabolism (middle). Long-term consequences of DNA injury (bottom) include permanent changes in the DNA sequence (point mutations affecting single genes or chromosome aberrations which may involve multiple genes) and their biological effects.[143]

DNA double-strand breaks (DSBs) are considered the most damaging type of DNA damage: one single unrepaired DSB is sufficient enough to induce cell death.[143] Inaccurate repair can lead to deletions or chromosomal aberrations that are associated with the development of cancer.[144] Hence, the repair of DSBs is both critical in cell survival and maintenance of genomic stability.[144]

Certainly, studies on genotoxic stress and cancer have since mostly circled around DNA damaging agents as described in the above Figure 4-17.[145–147] Moreover, studies on the roles of mechanical stress in DDR are still scarce.[148] Nonetheless, they are slowly emerging within the last years. It was reported by Singh et al. that lamins A/C, essential nuclear envelope proteins, are required for maintaining genomic stability and that their depletion stalls DDR.[149] Later, Davidson et al. associated the role of lamins A/C and DNA damage with migration-induced nuclear deformations.[90] Several additional studies emerged, reporting the genomic

instability caused by migration-induced nuclear deformation and DNA damage has been shown to promote cancer heterogeneity.[92–94] This establishes an interesting interplay between nuclear mechanics, genome integrity and phenotypic transformation.

Here, the possible extents of DDR to the case of damage induced by fluid shear stress alone, and by the combination of fluid shear stress and mechanical constraints were measured using γH2AX antibody, a DNA damage marker.

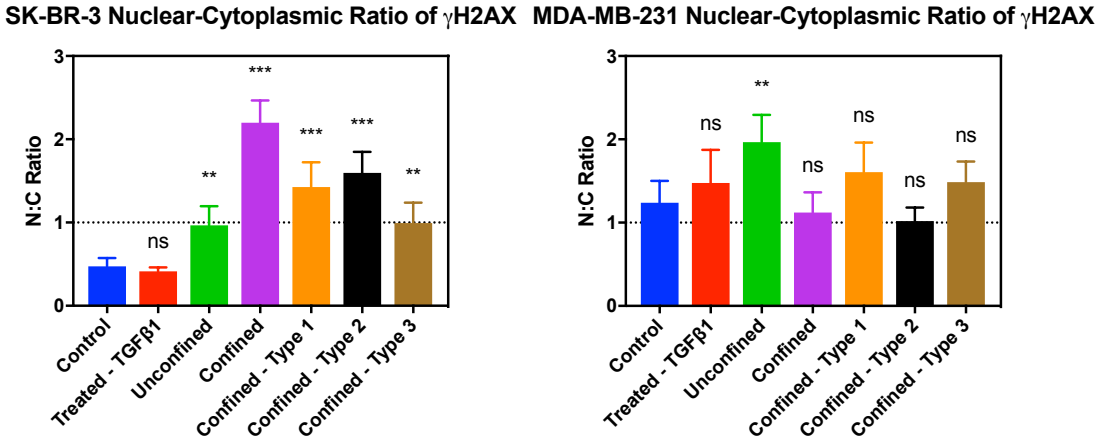

Figure 4-20A. Nuclear to cytoplasmic ratios of γH2AX immunostaining intensities in SK-BR-3 cells uncirculated (without fluid shear stress) and circulated (with fluid shear stress). Control (n=34), treated – TGFβ1: 10ng/ml (n=34), unconfined (n=50), confined: without constrictions (n=60), confined – type 1: with 11x20µm-long constrictions (n=40), confined – type 2: with 7x40µm-long constrictions (n=61), and confined – type 3: with 5x60µm-long constrictions (n=19). Error bars 95% CI. Kruskal-Wallis test (p<0.001) and Dunn's multiple comparisons post hoc test. *, significance level at 0.05; **, significance level at 0.01; ***, significance level at 0.001; ns, not significant.

Figure 4-20B. Nuclear to cytoplasmic ratios of γH2AX immunostaining intensities in MDA-MB-231 cells uncirculated (without fluid shear stress) and circulated (with fluid shear stress). Control (n=30), treated – TGFβ1: 10ng/ml (n=60), unconfined (n=35), confined: without constrictions (n=30), confined – type 1: with 11x20µm-long constrictions (n=24), confined – type 2: with 7x40µm-long constrictions (n=62), and confined – type 3: with 5x60µm-long constrictions (n=62). Error bars 95% CI. Kruskal-Wallis test (p<0.001) and Dunn's multiple comparisons post hoc test. *, significance level at 0.05; **, significance level at 0.01; ***, significance level at 0.001; ns, not significant.

For SK-BR-3, γH2AX expression in control cells showed higher localisation in the cytoplasm than in the nucleus (mean NC ratio: 0.474). SK-BR-3 cells treated with TGFβ1 maintained higher localisation in the cytoplasm than in the nucleus too and are insignificantly different to control cells (mean NC ratio: 0.413). However, unconfined SK-BR-3 cells that were exposed to fluid shear stress alone showed a significant increase in nuclear translocation of γH2AX (mean NC ratio: 0.966, p=0.002). Stark increase in nuclear translocations of γH2AX was seen

in SK-BR-3 cells that were confined (mean NC ratio: 2.2, $p<0.001$) and confined with 7 x 40 μm long constrictions (mean NC ratio: 1.6, $p=0.001$) when compared to unconfined.

MDA-MB-231 cells expressed higher localisations of γH2AX expressions in the nucleus than in the cytoplasm as compared to SK-BR-3 cells. The mean NC ratios are as follow for each condition: control (1.24), treated - TGFβ1 (1.48), unconfined (1.97), confined (1.12), confined – type 1 (1.6), confined – type 2 (1.02) and confined – type 3 (1.49). This might suggest evidence that DNA damage repair mechanisms were constantly at work in MDA-MB-231 cells, even in the control. Moreover γH2AX expressions across all conditions were more homogenous than in SK-BR-3 cells. In particular, no differences were observed in the γH2AX expressions from the various confinements, and between all confinements and the control, with the exception of the shear stress alone situation (unconfined). In the latter, a significant increase in nuclear translocation of γH2AX was measured when compared to the control ($p=0.006$).

This whole picture suggests that DNA damage response is weakly activated by physical mechanical constraints in MDA-MB-231 cells. Such a result is in line with the high deformability of these cells shown in the previous chapter. It may also highlight the property of mesenchymal cells to migrate through confinement and constrictions without inducing stark DNA damage.

Nonetheless, DDR response by γH2AX expression was significantly more apparent in SK-BR-3 than in MDA-MB-231 cells when compared to control cells. Amongst the three types of confinement geometries (types 1, 2 and 3), γH2AX expression in SK-BR-3 cells seemed to correlate positively with increased constriction length. More interestingly, visible numerous

γH2AX foci were apparent in the circulated/confined condition in both types of cells. It should be noted that the circulated/confined condition is the only condition where cells go through constant fluid shear stress from circulation and constant mechanical constraint without sudden bursts of geometrical changes, as seen in confined – types 1 to 3. This might suggest that different mechanical stressors from geometrical changes could induce different DDR mechanisms. In addition, it should not be dismissed that while nuclear translocations of γH2AX were detected considerably more in SK-BR-3 cells, non-detection of nuclear translocations of γH2AX in MDA-MB-231 cells does not equate to absence of activity. It might suggest a time-dependant regulation of γH2AX translocation that is consistent with what has been reported about DDR as a time-dependent process[150].

Up to now, elucidations of DDR mechanisms in response to mechanical stressors have been scarce. Here, multiple parameters of mechanical stressors: 1) circulation, 2) confinement, 3) constrictions and 4) prolonged constrictions; have been employed on SK-BR-3 and MDA-MB-231 mammary tumour cells. Further experiments, regarding e.g. nuclear envelope rupture and cell cycle analysis, will be interesting to elucidate the exact DDR mechanisms implicated by these mechanical stressors.

4.5 Conclusion

MDA-MB-231 cells are more responsive to a treatment to TGFβ1, a cytokine known to stimulate invasion, angiogenesis, and metastasis, and inhibit immune surveillance.[151] Although several hypotheses could be made, this differential sensitivity to TGFβ1 remains an open issue.

Combined circulation and confinement factors significantly contributed to morphological alterations of SK-BR-3 cells while MDA-MB-231 cells remained resistant and unaltered to such combined fluid shear stress and mechanical confinement. Moreover, SK-BR-3 exhibited significantly higher NC ratio, which is a strong predictor of malignancy.[138]

In confined geometries with various and increasing length of constrictions, both circulated SK-BR-3 and MDA-MB-231 cells displayed a sudden decrease in readouts across all of nuclear morphologies before steadily increasing in the subsequent constrictions with increasing lengths. The cell residence time factor due to prolonged effects of constrictions might explain why the cells might have time to recuperate and recover to baseline readouts. As discussed in the previous chapter, the global visual observation of the data amongst the different types of constrictions suggests a more general trend, in which a longer constriction tends to systematically induce a higher mean transit time. Here, based on their morphological features, SK-BR-3 cells appear to be more responsive to fluid shear stress and mechanical constraints than MDA-MB-231 cells. It might suggest that SK-BR-3 cells are more plastic than MDA-MB-231 cells, and they undergo non-reversible or delayed changes of shape in response to applied forces.

In summary, greater morphological changes are observed in SK-BR-3 than in MDA-MB-231 cells. The epithelial-mesenchymal status of these cells might contribute to the difference in response to applied mechanical stimuli between cell types. SK-BR-3 cells exhibit epithelial-like morphologies (which suggests higher rigidity) while MDA-MB-231 cells exhibit mesenchymal-like morphologies (which suggests higher deformability). This could explain why in this chapter, SK-BR-3 presented with greater observable changes than MDA-MB-231 cells. Significant increases of γH2AX expressions in SK-BR-3 than in MDA-MB-231 cells support the aforementioned reasoning, in which DNA damage repair mechanisms were much more triggered in SK-BR-3 than in MDA-MB-231 cells in response to the applied stressors. Nonetheless, MDA-MB-231 could have more enhanced or efficient DDR mechanism than SK-BR-3 cells in response to the aforementioned mechanical stressors. While different mechanical stressors from geometrical changes could induce different DDR mechanisms, it is clear that the imposed mechanical constraints have varying degree of impact on the morphologies of different types of cells. The next question to address is if this degree of impact significant enough to induce genotypic changes in cells. This shall be addressed in the following chapter.

CHAPTER FIVE: MOLECULAR DETECTION OF EMT/MET TRANSCRIPTION FACTORS IN TUMOUR CELLS AFTER FLOW-INDUCED MIGRATION IN MICRO CONSTRICTIONS

5.1 Introduction

EMT has been categorised into three distinct types.[2,3,32] Type 1 EMT is involved in implantation, embryogenesis and organ development. Successive waves of cellular transition between epithelial and mesenchymal states are required for normal embryonic patterning and organ formation. The generation of secondary epithelium from mesenchymal cells through MET is regarded as a highly regulated process. More importantly, type 1 EMT does not cause fibrosis or an invasive phenotype as seen in the following types of EMT. Type 2 EMT is responsible for wound healing, tissue regeneration and organ fibrosis. It is initiated by injury and inflammation causing the production of fibroblasts to reconstruct tissues. Such production is continuous unless the inflammation signals cease. Therefore, chronic inflammation can cause fibrosis resulting in a pathological state of excess tissue. Type 3 EMT is associated with aggressive tumour cells that acquire the potential to invade and metastasise. There have been many studies proposing the activation of an EMT programme as the mechanism through which epithelial cancer cells acquire their malignant phenotype.[37,152–154] In this chapter and the rest of this research thesis, type 3 EMT will be the main focus.

The loss of E-cadherin expression is recognised as the fundamental event in EMT.[37] The types of EMT transcription factors (EMT-TFs) that repress E-cadherin are determined by how they affect the promoter of the E-cadherin gene, *CDH1*.[152] In the following Figure 5-1, Snail (Snail1), Slug (Snail2), ZEB1, ZEB2, E47 and KLF8 factors bind to the region and directly repress the E-cadherin promoter. However, Twist, Goosecoid, E2.2 and Foxc2 repress *CDH1* transcription indirectly. This suggests that even if they are able to induce EMT and down-regulate E-cadherin, they are unable to bind to the E-cadherin promoter.[155] Direct repression of the E-cadherin promoter by EMT-TFs has also been reported to act on

numerous components of the epithelial junction complex (ZEB2)[156] and cell polarity factor genes (ZEB1).[157]

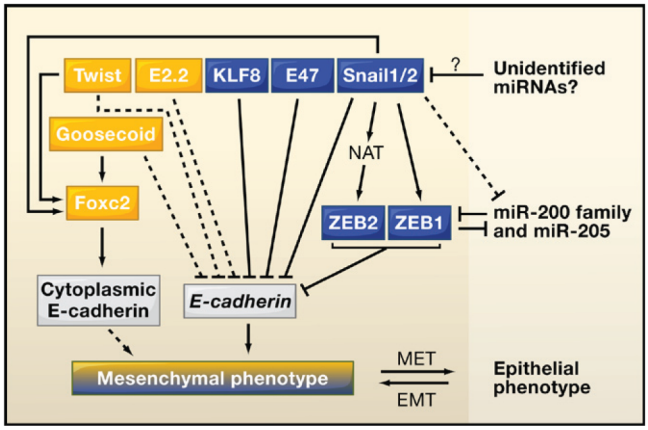

Figure 5-1 | E-cadherin Transcription in Normal and Cancer Cells. Snail1 activates the expression of the ZEB genes by different mechanisms, including the induction of a natural antisense transcript for ZEB2 (NAT). The miR-200 family and in some cases also miR-205, represses the transcription of ZEB genes preventing EMT. A loop of miRNAs and ZEB factors cross-regulation plus the cooperation of several EMT inducers reinforces the control of the EMT process. Preliminary data indicate that Snail1 may also repress the expression of the miR-200 family. Whether miRNAs can also control Snail expression awaits further investigation.[158]

In addition, several EMT-TFs such as Twist[159], Snail1[160] and Snail2[161] have also been reported to inhibit apoptosis that allows a selective advantage for cells to migrate and colonise secondary sites. Therefore, overcoming anoikis, a cell death programme induced by inappropriate or loss of cell adhesion is a pre-requisite throughout the invasion-metastasis cascade.[48] Derksen et al. showed that EMT and anoikis suppression are linked: the loss of E-cadherin in mammary carcinoma protected cells from anoikis while facilitating angiogenesis.[162] In tumourigenesis, Snail1,[154,163] Snail2[164], Twist1[119,165] and ZEB1[119] have been suggested to play key roles too.

Over and above, the plasticity of EMT in cells from aggressive tumours enables them to switch from proliferative to invasive phenotypes and vice versa.[120,166] It has been vastly observed in mouse mammary tumour models that the initiation of EMT can occur during the early stages of tumourigenesis and progress during its later stages.[167–170] This raises the

question of the status of CTCs amongst the spectrum of functional and morphological characteristics as well as epithelial and mesenchymal states. From these, the process of EMT can be considered as a hallmark-facilitating program as well as having influence on pathways linked to tumour progression and metastatic dissemination.

The ability of tumour cells to invade through the basement membrane is believed to initiate the final stages of the multistep process leading to the life-threatening, metastatic development.[72] The involvement of EMT in the progression of a benign tumour to invasive and metastatic cells has been widely studied.[33,158] However, while histological studies have not managed to report the association of mesenchymal phenotypes with EMT *in situ,* only studies *in vitro* have reported the EMT process in action.[125,171,172] This raises controversies surrounding EMT as the initiating factor of metastasis.[38,173] Subsequently, arguments for the role of EMT in cancer dissemination have been made. It was proposed that CTCs have had undergone EMT or are still continuously undergoing the transition while in the circulation.[132] Clinical studies have reported the circulating half-lives of CTCs (<24 hours)[174,175] while CTC clusters have been shown in animal models to exhibit circulating half-lives on the order of minutes.[176] This suggests a short half-life for CTCs in the blood circulation. However, the effects of mechanical stressors in the microcirculation on EMT transition are still unknown. For instance, how anatomical structures of the microcirculation, i.e. flow dynamics and mechanical constrictions, contribute to these proposed roles of EMT have yet to be elucidated. Therefore, this requires additional in-depth probing.

Here, the potential effects on phenotypic biomarkers, particularly those for EMT, of flow-induced migration of cells in micro channels consisting of different geometries of mechanical constraints will be investigated.

5.2 Aims

The objective of this experiment is to conduct a differential expression analysis of EMT/MET transcription factors' mRNA levels of tumour cells that had been subjected to circulation, confinement and constrictions within the microfluidic system. SK-BR-3 and MDA-MB-231 breast tumour cells are retrieved from the microfluidic system and these cells are subsequently prepared for highly specific amplifications with SYBR Green I dye technology.

In this chapter, results on the quantification of mRNA expression levels of EMT/MET transcription factors in response to fluid shear stress alone and the combination of fluid shear stress and mechanical constraints will be presented. A panel of candidate genes that are differentially expressed in the mechanical-treated tumour cells will be compared to control tumour cells. In particular, the following analysis will highlight the role of Twist2. Therefore, results on the localisation of Twist2 protein by an immunofluorescence assay employed on tumour cells isolated from the microfluidic system will be presented.

In the next section, raw results will be presented before discussing them in thorough in the last section of this chapter.

5.3 Results

SK-BR-3 and MDA-MB-231 cells that were 1) treated with 10 ng/ml of TGFβ1 for 24 hours, or circulated in the microfluidic channels of 2) unconfined, 3) confined, and 4-6) confined with constrictions of various lengths as described in chapter four, were isolated. Untreated and uncirculated cells were used as a negative control. The first half of the isolated cells was retrieved for the purification of total RNA. The total RNA was reversed transcribed to single-stranded cDNA for target amplifications using real-time quantitative PCR (RT-qPCR). The second half of the isolated cells was fixed for the detection of a specific protein using techniques of indirect immunofluorescence. Complete methods had been described in detail in chapter two.

A panel of candidate genes: E-cadherin, N-cadherin, Vimentin, Snail1, Snail2, Twist1, Twist2, ZEB1, ZEB2, β-catenin and MMP-9 was used as targets of interests in the quantification of the mRNA expression levels. Heat map illustrations of the panel's mRNA expression levels in SK-BR-3 and MDA-MB-231 cells are presented in the following Figure 5-2. They highlight changes in gene expression in response to circulation and confinement that will be quantitatively analysed later in the text.

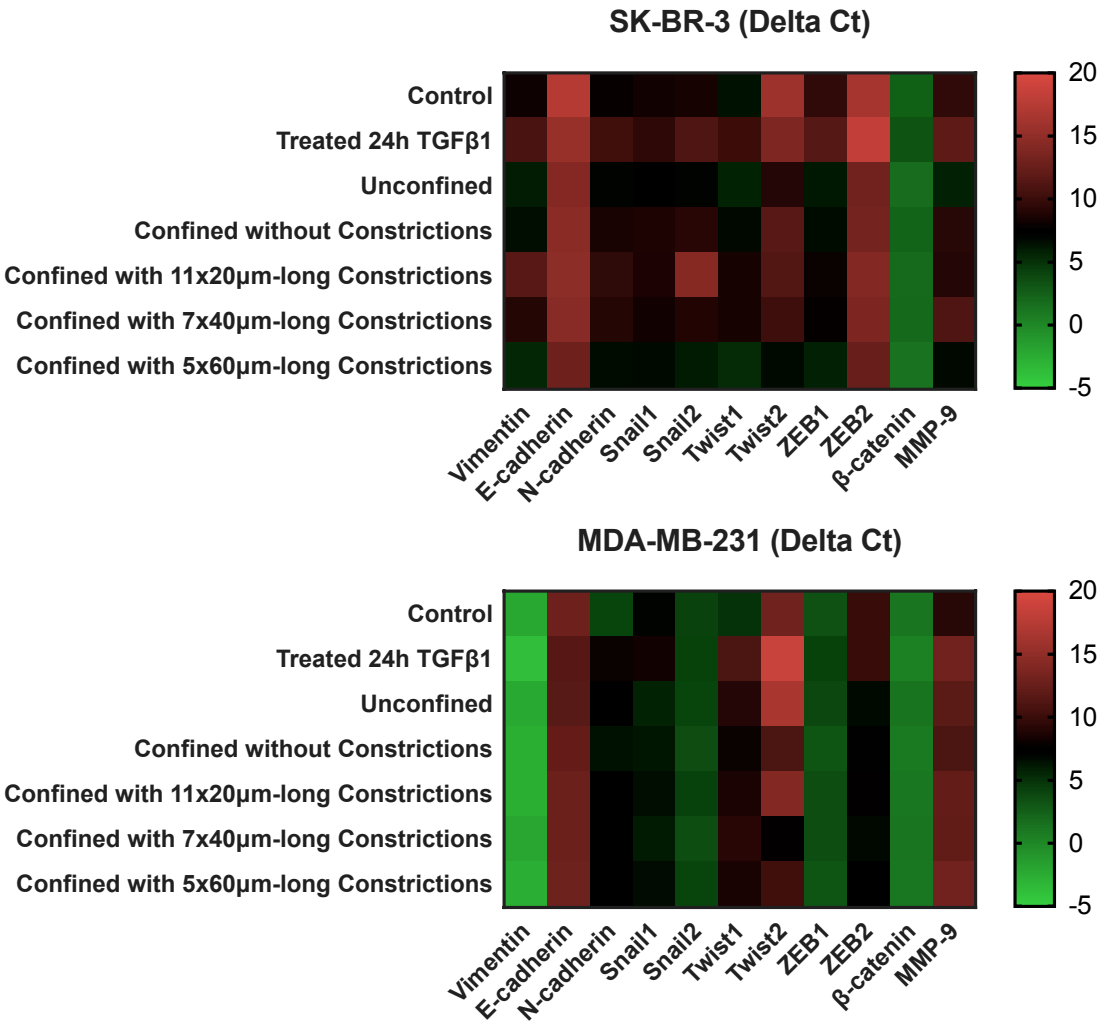

Figure 5-2. Heat map illustrations of the results of qRT-PCR for Vimentin, E-cadherin, N-cadherin, Snail1, Snail2, Twist1, Twist2, ZEB1, ZEB2, β- catenin and MMP-9 given in delta Ct (Ct target gene—Ct housekeeping gene) for each experimental group in SK-BR-3 (top) and MDA-MB-231 (bottom) cells.

The relative gene expression data for TGFβ1-treated cells, as well as circulated and unconfined (20 µm height) SK-BR-3 and MDA-MB-231 cells compared to uncirculated cells are presented in the following Figure 5-3 and Figure 5-4 respectively. Broader differentially expressed genes were observed in MDA-MB-231 compared to SK-BR-3 cells.

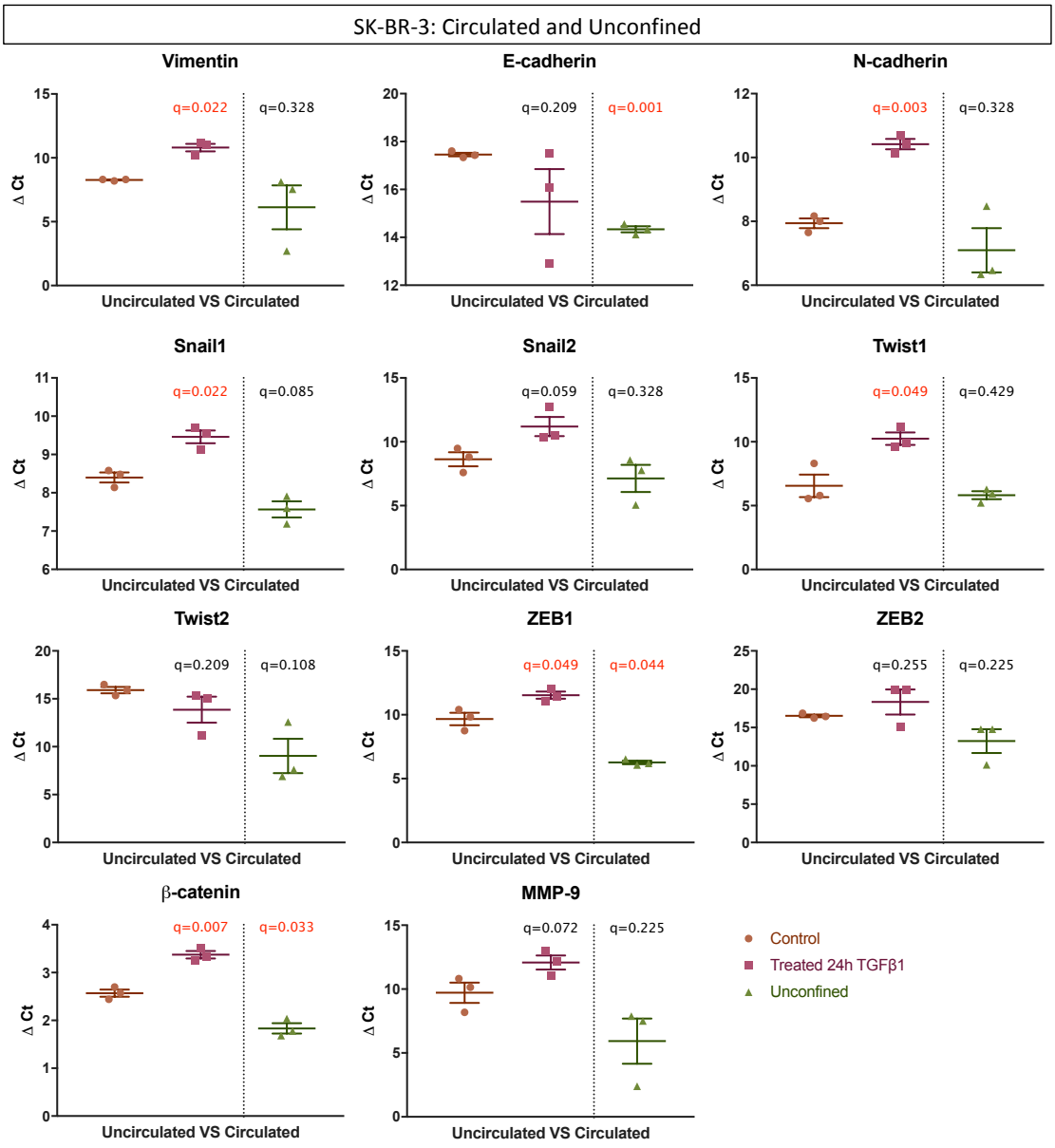

Figure 5-3. A panel of mRNA biomarker expression levels implicated in EMT/MET of SK-BR-3 cells uncirculated (without fluid shear stress) and circulated (with fluid shear stress) by qRT-PCR. Gene expression values were normalised to GAPDH. Data represent the mean ± S.E. of three independent experiments for each condition. Unpaired t-test with Welch's correction followed by the False Discovery Rate (FDR) approach to multiple comparisons (two-stage linear step-up procedure of Benjamini, Krieger and Yekutieli) and significance and confidence level at 0.05. Q values in red denote significant values.

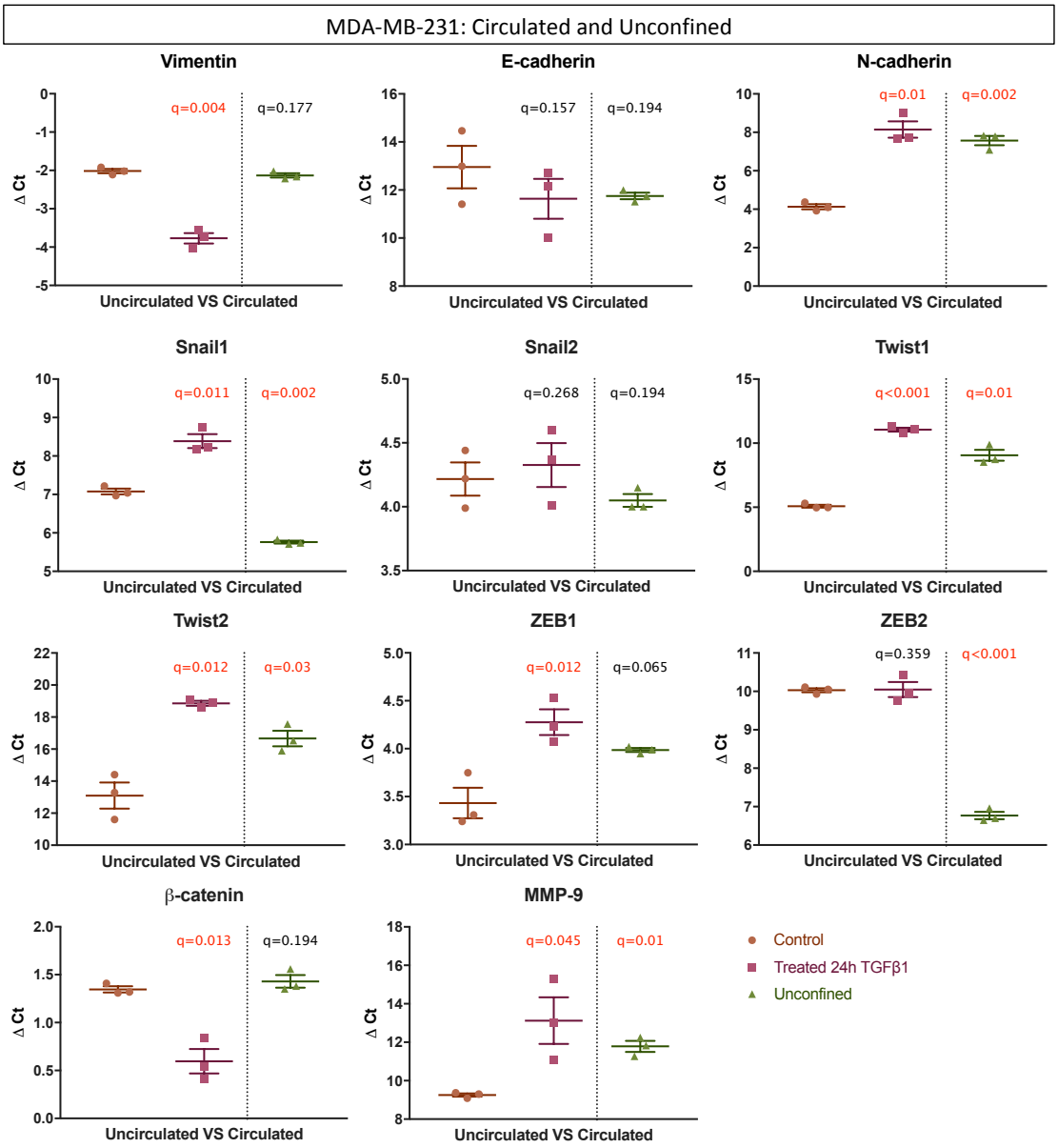

Figure 5-4. A panel of mRNA biomarker expression levels implicated in EMT/MET of MDA-MB-231 cells uncirculated (without fluid shear stress) and circulated (with fluid shear stress) by qRT-PCR. Gene expression values were normalised to GAPDH. Data represent the mean ± S.E. of three independent experiments for each condition. Unpaired t-test with Welch's correction followed by the False Discovery Rate (FDR) approach to multiple comparisons (two-stage linear step-up procedure of Benjamini, Krieger and Yekutieli) and significance and confidence level at 0.05. Q values in red denote significant values.

The relative gene expression data for circulated and confined (15 µm height) SK-BR-3 and MDA-MB-231 cells compared to circulated and unconfined (20 µm height) cells are presented in the following Figure 5-5 and Figure 5-6 respectively. In this situation, SK-BR-3 cells did not show any differentially expressed gene while MDA-MB-231 differentially expressed many genes.

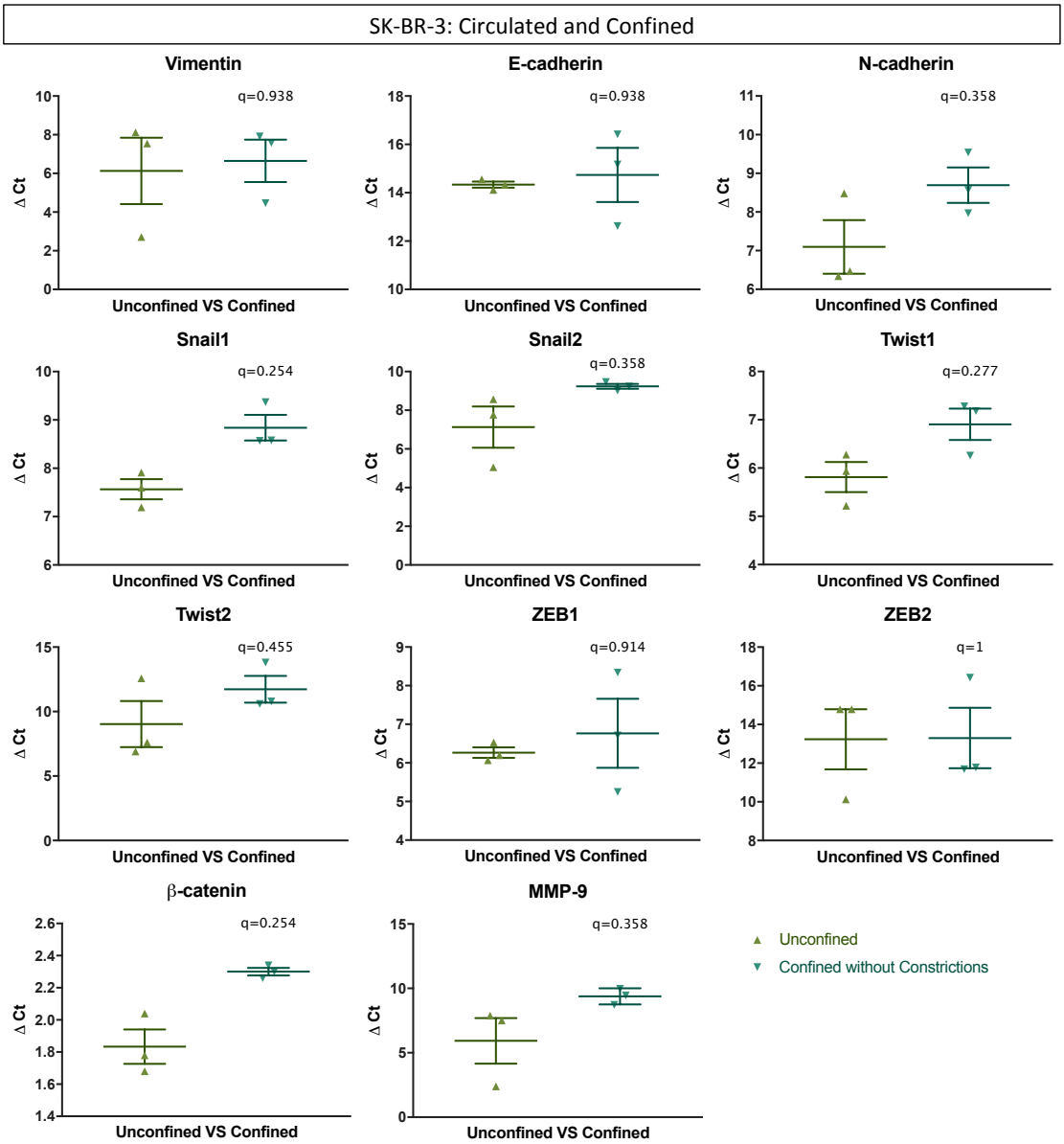

Figure 5-5. A panel of mRNA biomarker expression levels implicated in EMT/MET of SK-BR-3 cells circulated (with fluid shear stress) by qRT-PCR. Gene expression values were normalised to GAPDH. Data represent the mean ± S.E. of three independent experiments for each condition. Unpaired t-test with Welch's correction followed by the False Discovery Rate (FDR) approach to multiple comparisons (two-stage linear step-up procedure of Benjamini, Krieger and Yekutieli) and significance and confidence level at 0.05. Q values in red denote significant values.

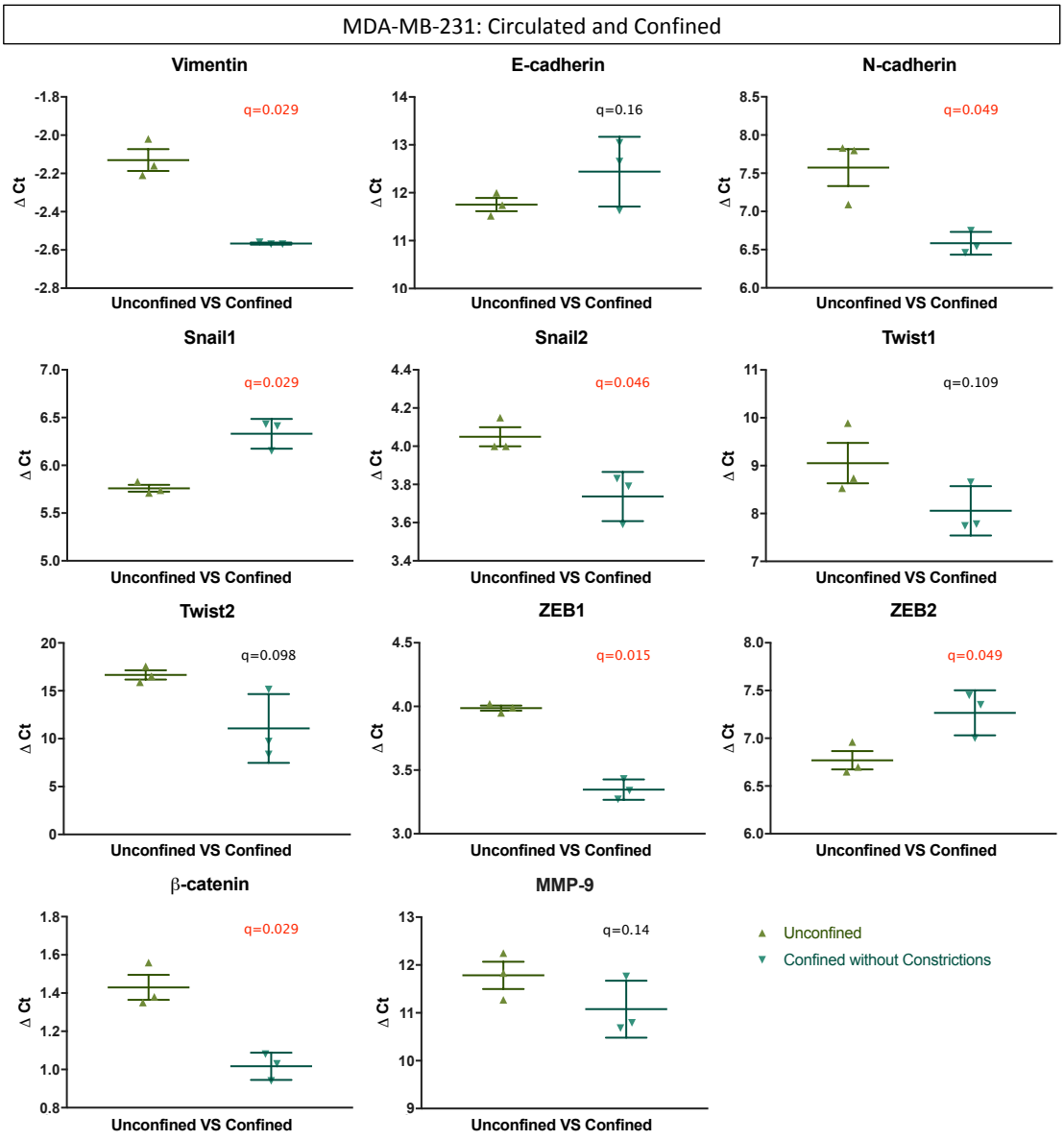

Figure 5-6. A panel of mRNA biomarker expression levels implicated in EMT/MET of MDA-MB-231 cells circulated (with fluid shear stress) by qRT-PCR. Gene expression values were normalised to GAPDH. Data represent the mean ± S.E. of three independent experiments for each condition. Unpaired t-test with Welch's correction followed by the False Discovery Rate (FDR) approach to multiple comparisons (two-stage linear step-up procedure of Benjamini, Krieger and Yekutieli) and significance and confidence level at 0.05. Q values in red denote significant values.

The relative gene expression data for circulated, confined (15 μm height) and constricted SK-BR-3 and MDA-MB-231 cells compared to circulated and unconfined (20 μm height) cells are presented in the following Figure 5-7 and Figure 5-8 respectively. Almost no response, except for significant down-regulations of Snail2 and ZEB1, was triggered by 3D confinement in SK-BR-3 cells. Interestingly, the two lowest curvatures in constrictions (7 x 40 μm- and 5 x 60 μm-long constrictions) only resulted in differentially expressed genes in MDA-MB-231 cells. Vimentin, Snail2, Twist2, ZEB1, and β-catenin were amongst the differentially expressed genes in MDA-MB-231 cells that were significantly up regulated. While Snail1 versus Snail2 and ZEB1 versus ZEB2 had inverse expression patterns in MDA-MB-231 cells, Twist2 but not Twist1 was differentially expressed. As previously mentioned, Twist1 but not Twist2 had been suggested to play key roles in tumourigenesis.[119,165] Therefore, it will be interesting to further investigate the role of Twist2 in response to 3D confinement under flow.

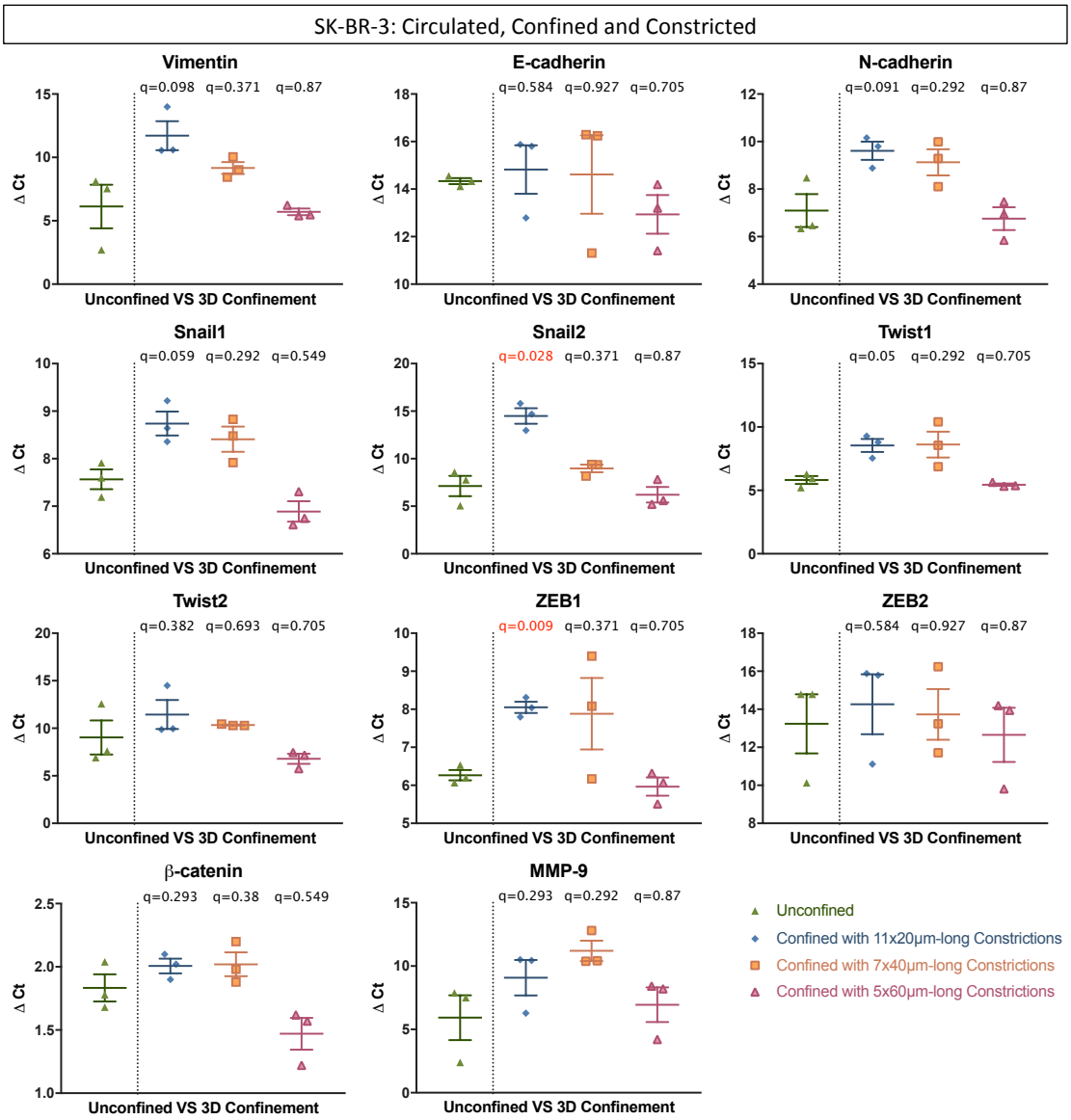

Figure 5-7. A panel of mRNA biomarker expression levels implicated in EMT/MET of SK-BR-3 cells circulated (with fluid shear stress) by qRT-PCR. Gene expression values were normalised to GAPDH. Data represent the mean ± S.E. of three independent experiments for each condition. Unpaired t-test with Welch's correction followed by the False Discovery Rate (FDR) approach to multiple comparisons (two-stage linear step-up procedure of Benjamini, Krieger and Yekutieli) and significance and confidence level at 0.05. Q values in red denote significant values.

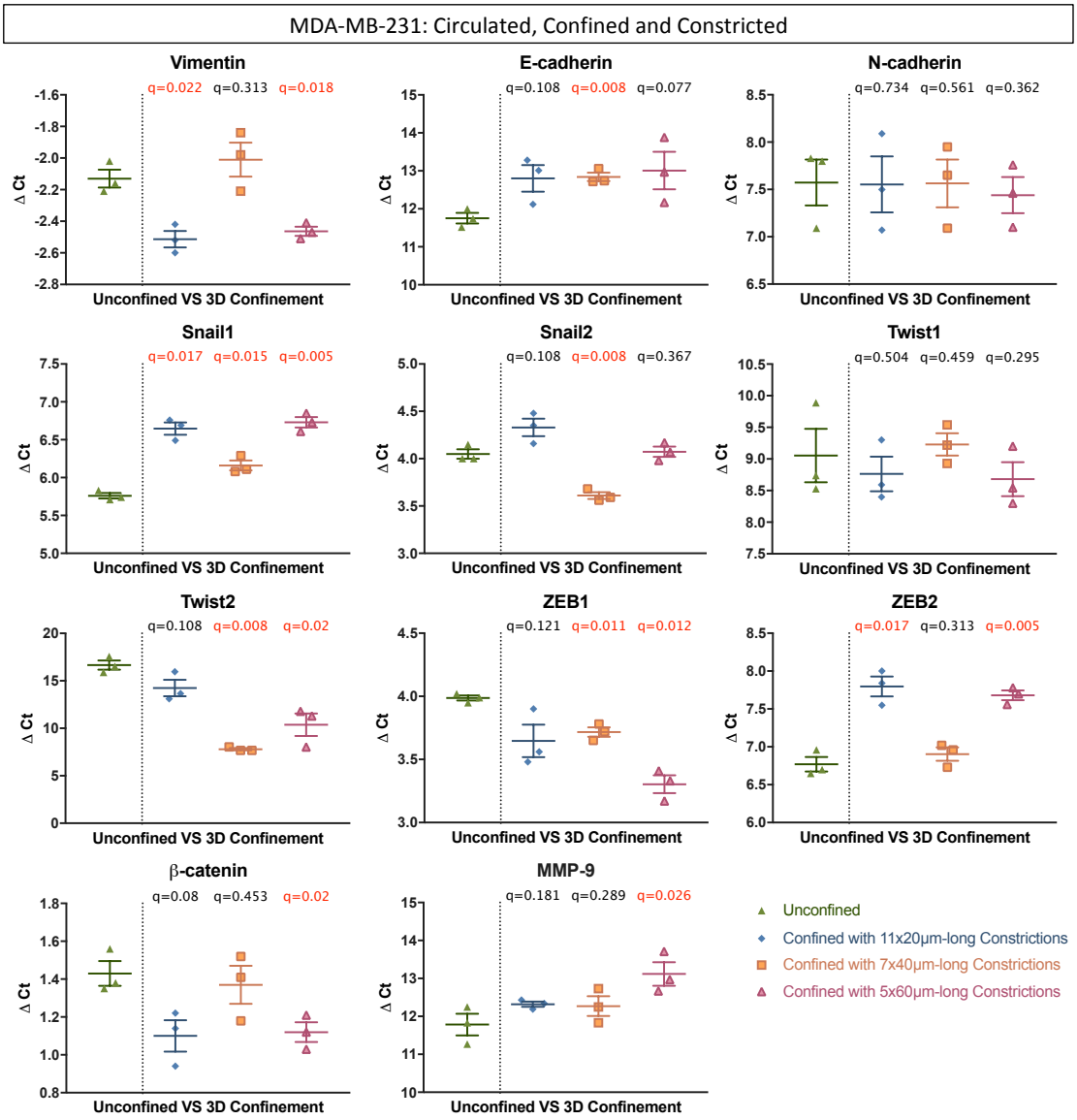

Figure 5-8. A panel of mRNA biomarker expression levels implicated in EMT/MET of MDA-MB-231 cells circulated (with fluid shear stress) by qRT-PCR. Gene expression values were normalised to GAPDH. Data represent the mean ± S.E. of three independent experiments for each condition. Unpaired t-test with Welch's correction followed by the False Discovery Rate (FDR) approach to multiple comparisons (two-stage linear step-up procedure of Benjamini, Krieger and Yekutieli) and significance and confidence level at 0.05. Q values in red denote significant values.

In parallel to isolated cells that were retrieved for the purification of total RNA, the other half of isolated cells were fixed and stained with Twist2 primary antibody. Their nuclei were counterstained with DAPI. The confocal images of immunostained cells of SK-BR-3 and MDA-MB-231 are depicted in the following Figure 5-9 and Figure 5-10 respectively.

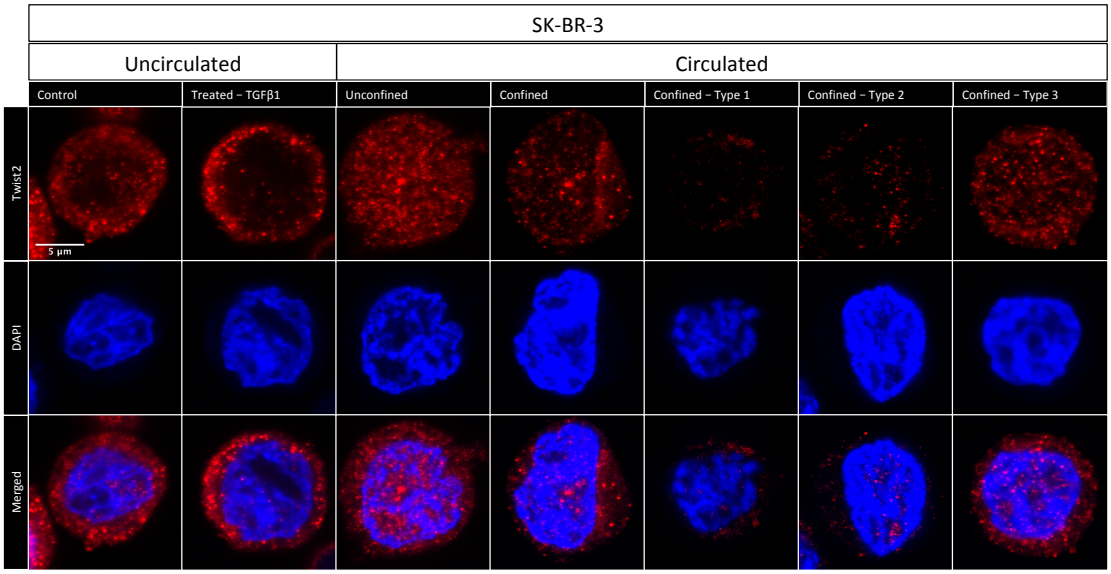

Figure 5-9. Twist2 and DAPI staining of SK-BR-3 cells uncirculated (without fluid shear stress) and circulated (with fluid shear stress). Control (n=65), treated – TGFβ1: 10ng/ml (n=65), unconfined (n=84), confined: without constrictions (n=92), confined – type 1: with 11x20µm-long constrictions (n=71), confined – type 2: with 7x40µm-long constrictions (n=94), and confined – type 3: with 5x60µm-long constrictions (n=44).

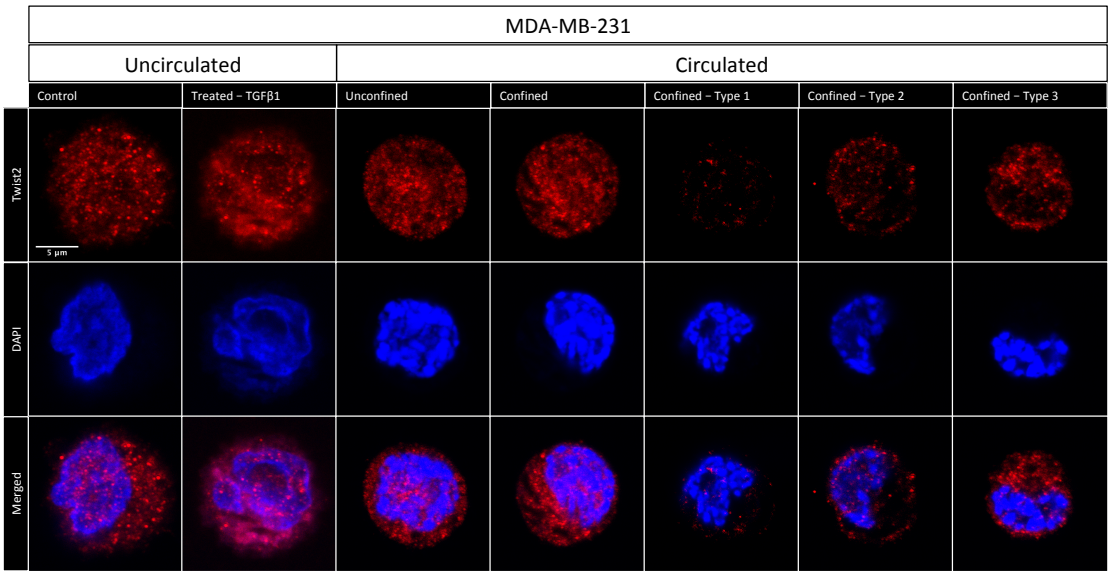

Figure 5-10. Twist2 and DAPI staining of MDA-MB-231 cells uncirculated (without fluid shear stress) and circulated (with fluid shear stress). Control (n=63), treated – TGFβ1: 10ng/ml (n=121), unconfined (n=70), confined: without constrictions (n=62), confined – type 1: with 11x20µm-long constrictions (n=27), confined – type 2: with 7x40µm-long constrictions (n=123), and confined – type 3: with 5x60µm-long constrictions (n=124).

Subsequently, the fluorescence intensity of Twist2 protein was measured within the nucleus and cytoplasm regions separately. The NC ratio between these intensities is presented in the following Figure 5-11 and Figure 5-12 for SK-BR-3 and MDA-MB-231 cells respectively.

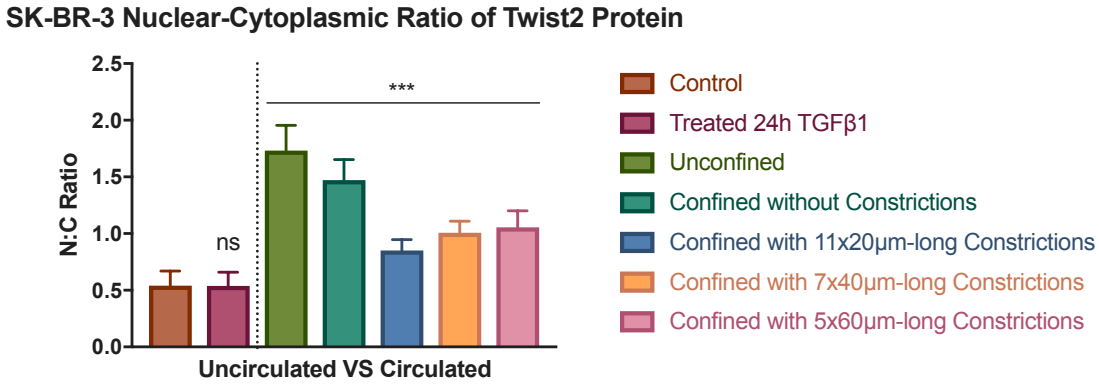

Figure 5-11. NC ratio of Twist2 protein of SK-BR-3 cells uncirculated (without fluid shear stress) and circulated (with fluid shear stress). Control (n=65), treated – TGFβ1: 10ng/ml (n=65), unconfined (n=84), confined: without constrictions (n=92), confined – type 1: with 11x20µm-long constrictions (n=71), confined – type 2: with 7x40µm-long constrictions (n=94), and confined – type 3: with 5x60µm-long constrictions (n=44). Error bars represent 95% confidence interval. Kruskal-Wallis test ($p<0.001$) and Dunn's multiple comparisons post hoc test. ***, significance level at 0.001; ns, not significant.

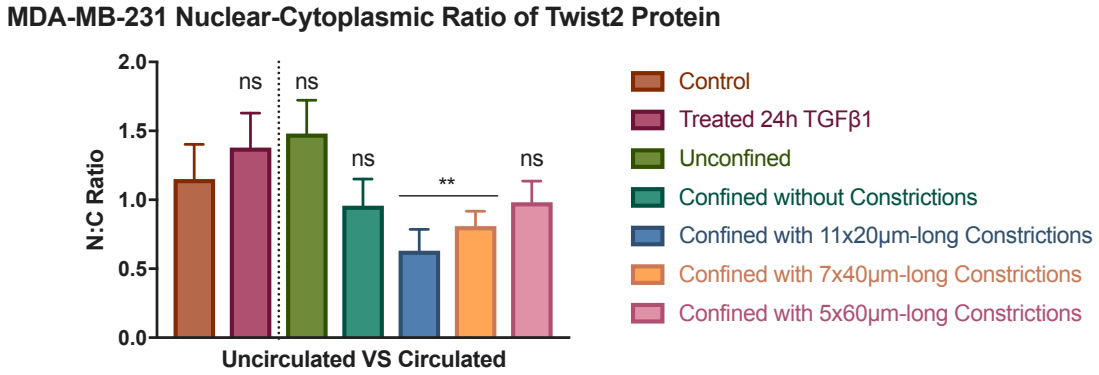

Figure 5-12. NC ratio of Twist2 protein of MDA-MB-231 cells uncirculated (without fluid shear stress) and circulated (with fluid shear stress). Control (n=63), treated – TGFβ1: 10ng/ml (n=121), unconfined (n=70), confined: without constrictions (n=62), confined – type 1: with 11x20µm-long constrictions (n=27), confined – type 2: with 7x40µm-long constrictions (n=123), and confined – type 3: with 5x60µm-long constrictions (n=124). Error bars represent 95% confidence interval. Kruskal-Wallis test ($p<0.001$) and Dunn's multiple comparisons post hoc test. **, significance level at 0.01; ns, not significant.

5.4 Discussion

In this section, the results presented earlier will be discussed, taking into account each of the stimulations that were imposed to the cells. This includes the chemical treatment by TGFβ1 of adherent cells, followed by the influence of flow dynamics on suspended cells, and finally the impact of various mechanical confinements on the circulating cells.

TGFβ1 Treatment

SK-BR-3			
	Significance	P value	Q value
Vimentin	Yes (Down)	0.012	**0.02205**
E-cadherin	No	0.284	0.20874
N-cadherin	Yes (Down)	0.00037	**0.00272**
Snail1	Yes (Down)	0.009	**0.02205**
Snail2	No	0.056	0.0588
Twist1	Yes (Down)	0.033	**0.04851**
Twist2	No	0.267	0.20874
ZEB1	Yes (Down)	0.04	**0.049**
ZEB2	No	0.381	0.25458
β-catenin	Yes (Down)	0.002	**0.00735**
MMP-9	No	0.078	0.07166
MDA-MB-231			
	Significance	P value	Q value
Vimentin	Yes (Up)	0.002	**0.0042**
E-cadherin	No	0.336	0.1568
N-cadherin	Yes (Down)	0.007	**0.0098**
Snail1	Yes (Down)	0.01	**0.0105**
Snail2	No	0.638	0.26796
Twist1	Yes (Down)	0.00001538	**0.0000646**
Twist2	Yes (Down)	0.017	**0.0119**
ZEB1	Yes (Down)	0.017	**0.0119**
ZEB2	No	0.941	0.35929091
β-catenin	Yes (Up)	0.022	**0.0132**
MMP-9	Yes (Down)	0.085	**0.044625**

Table 5-1 | Summary of statistical results of TGFβ1-treated cells versus control cells. Unpaired t-test with Welch's correction followed by the False Discovery Rate (FDR) approach to multiple comparisons (two-stage linear step-up procedure of Benjamini, Krieger and Yekutieli) and significance and confidence level at 0.05. Q values in red denote significant values.

TGFβ1 signalling has been shown to play an important role in EMT.[177] Various significant changes of gene expression in these experiments were observed. This is consistent with the known fact that the addition of TGFβ1 in culture induces EMT in various epithelial cells.[178] The results will be discussed in detail below.

β-catenin is a multifunctional protein with a central role in physiological homeostasis whose aberrant high expression leads to various diseases including cancer through the canonical or non-canonical Wnt pathway.[179] It acts both as a transcriptional co-regulator and an adaptor protein for intracellular adhesion while binding with E-cadherin.[180] Nevertheless and interestingly, Cai et al. reported on breast cancer cells that while the down-regulation of β-catenin decreases tumourigenicity, it promotes EMT.[181] When treated transiently with 10 ng/ml of TGFβ1 for 24 hours to induce or boost EMT, suspended SK-BR-3 cells showed a significant down-regulation of β-catenin mRNA transcript, while suspended MDA-MB-231 cells showed a significant up-regulation. As MDA-MB-231 cells are more mesenchymal-like in morphology than SK-BR-3 cells, it could mean that the down-regulation of β-catenin was one of the elements promoting EMT in SK-BR-3 cells.

Vimentin, a major constituent of the intermediate filament (IF) family of proteins, is ubiquitously expressed in normal mesenchymal cells and is known to maintain cellular integrity and provide resistance against stress while its increase has been reported in various epithelial cancers.[182] The expression of Vimentin has to be apprehended in a more global view including the co-expression of other EMT genes. Gilles et al. reported that β-catenin distribution is higher in invasive and migratory cells expressing vimentin than in non-invasive and less-motile vimentin-negative cell lines.[183] They also found that β-catenin up-regulates the Vimentin promoter.[183] Satelli et al. further reported that free Vimentin in the tumour microenvironment acts as a positive regulator of the β-catenin signalling pathway, which provides a basis for cancer invasive properties.[184] Snail1 and ZEB1 have been reported to up-regulate in EMT during cancer initiation and progression[155] with Snail1 directly targeting the ZEB1 gene.[34] Nonetheless, many studies have indicated that Snail1, although required for triggering EMT, is not necessary for the maintenance of the mesenchymal

phenotype.[185–188] Furthermore, reports of high concentrations of Vimentin in the blood of cancer patients[189,190] suggest to support this theory that Snail1 up-regulation is not necessary for maintaining the mesenchymal phenotype. These reports are consistent with the results obtained from MDA-MB-231 cells, with both Vimentin and β-catenin found to be significantly up-regulated while Snail1 found to be significantly down-regulated. Hence, judging from their initial mesenchymal-like morphology, MDA-MB-231 cells might have already undergone EMT. Therefore, the abundance of expression in Vimentin and β-catenin seemed to be regulating the mesenchymal properties of MDA-MB-231 cells well without the need for Snail1 to maintain the mesenchymal phenotype.

Finally, the absence of up-regulation of mesenchymal genes involved in EMT such as Vimentin, Snail1, Snail2, Twist1 and Twist2 in SK-BR-3 cells could mean that the 10 ng/ml of TGFβ1 for 24 hours used was not sufficient to induce EMT. However, cell culture images of control and treated illustrated otherwise (Figure 5-13).

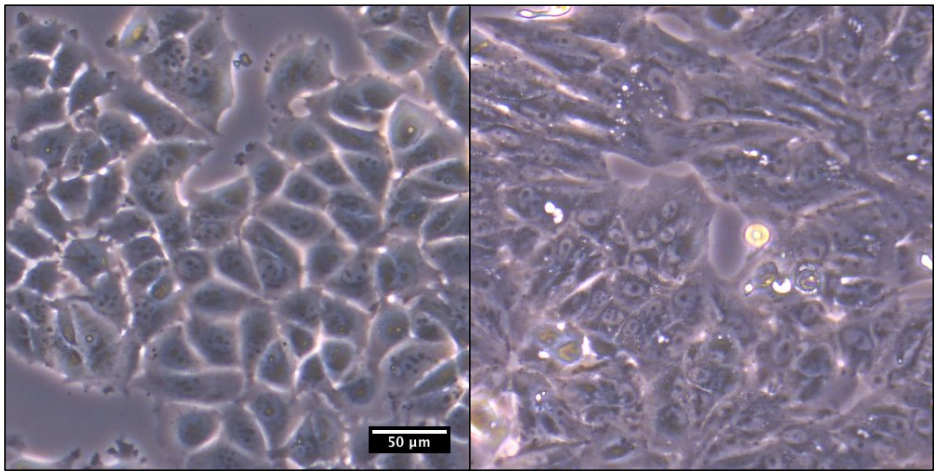

Figure 5-13. Morphological changes in SK-BR-3 cells. SK-BR-3 cells treated with 0.1% DMSO for 24 hours as control (left). SK-BR-3 cells treated with TGFβ1 (10 ng/ml) for 24 hours (right).

Fluid Shear Stress from Circulation

SK-BR-3			
	Significance	P value	Q value
Vimentin	No	0.338	0.327915
E-cadherin	Yes (Up)	0.000131	**0.001238**
N-cadherin	No	0.347	0.327915
Snail1	No	0.036	0.08505
Snail2	No	0.301	0.327915
Twist1	No	0.499	0.428686
Twist2	No	0.057	0.10773
ZEB1	Yes (Up)	0.014	**0.0441**
ZEB2	No	0.167	0.22545
β-catenin	Yes (Up)	0.007	**0.033075**
MMP-9	No	0.153	0.22545
MDA-MB-231			
	Significance	P value	Q value
Vimentin	No	0.225	0.1771875
E-cadherin	No	0.305	0.19415455
N-cadherin	Yes (Down)	0.0009671	**0.00203091**
Snail1	Yes (Up)	0.0006645	**0.00203091**
Snail2	No	0.33	0.19415455
Twist1	Yes (Down)	0.008	**0.01008**
Twist2	Yes (Down)	0.029	**0.03045**
ZEB1	No	0.072	0.0648
ZEB2	Yes (Up)	0.00006361	**0.00040074**
β-catenin	No	0.339	0.19415455
MMP-9	Yes (Down)	0.008	**0.01008**

Table 5-2 | Summary of statistical results of unconfined, circulated cells versus control cells. Unpaired t-test with Welch's correction followed by the False Discovery Rate (FDR) approach to multiple comparisons (two-stage linear step-up procedure of Benjamini, Krieger and Yekutieli) and significance and confidence level at 0.05. Q values in red denote significant values.

In response to fluid shear stresses comparable to that of normal blood microcirculation, circulated SK-BR-3 cells are positively triggered with significant increase in E-cadherin, ZEB1 and β-catenin. Circulated MDA-MB-231 cells are positively triggered with significant increase in Snail1 and ZEB2.

E-cadherin is a cell-to-cell adhesion molecule that is critical for embryonic and mammary development.[43] In the context of cancer, loss of E-cadherin and gain of mesenchymal markers have been primarily viewed during EMT.[191] Nonetheless, here its expression has been reported to be up-regulated in circulated SK-BR-3 cells. It is worth pointing out that SK-BR-3 cells harbour a genetic deletion of one allele in *CDH1*, the E-cadherin-encoding gene, resulting in absence of expression.[192,193] This suggests that fluid shear stress could trigger E-cadherin re-expression in SK-BR-3 cells. Maggiorani et al. reported that fluid shear stress altered epithelial organisation by down-regulating E-cadherin expression in human renal

tubular cells.[194] Nonetheless, when looking at the context of cancer, Chu et al. reported a paradoxical role of E-cadherin in regulating tumourigenicity and hypoxia responses of breast tumours *in vivo*.[195] Moreover, with the dual role of β-catenin as was previously discussed, mutation of E-cadherin in cancer cells may disrupt the interaction with β-catenin that subsequently promotes the nuclear translocation of β-catenin triggering the formation of transcriptional factors downstream of the Wnt pathway such as Snail1, ZEB1 and ZEB2.[157] Based on earlier results presented, this might suggest that the up-regulation of β-catenin coupled with the re-expression of E-cadherin could hypothetically trigger the up-regulation of ZEB1 in SK-BR-3 cells due to exposure to fluid shear stress. It was also expected to observe an increase in Snail1 and ZEB2 in circulated MDA-MB-231 cells. Aigner et al. further proposed that ZEB1 functions as a master regulator of epithelial plasticity in cancer cell invasion and human tumour progression *in vivo*.[157] On the other hand, Twist1[196] and Twist2[197] have been reported to induce EMT alone or cooperatively. Furthermore, the over-expression of Twist2 results in the induction of EMT and increases the generation of breast cancer cells with stem-like characteristics in the tumour microcirculation.[198] However, in circulated MDA-MB-231 cells, both Twist1 and Twist2 were significantly decreased. It could be that the mechanical stress from circulation imposed here had a reverse effect or not sufficient for a positive trigger.

While it is generally accepted that during embryonic development, the EMT programme leads to complete conversion of epithelial cells into mesenchymal cells, cancer cells in a tumour most often undergo an incomplete or partial EMT.[166,199,200] This proposal is consistent with data that have been presented in this chapter, in which EMT-TFs such as Snail1, Snail2, Twist1, Twist2, ZEB1 and ZEB2 have been identified as independently responsible for an incomplete or partial EMT. This is because EMT can be induced by multiple extracellular

cues that converge in the activation of a plethora of EMT-TFs that belong to different gene families. This is consistent with the heterogeneity observed in different tumour types and even within a single tumour. As Brabletz et al. have asserted, the absence of a specific EMT-TF cannot be taken as proof of the absence of EMT, and the use of a particular mesenchymal marker as a tool to follow EMT as a whole is not appropriate.[120]

Mechanical Constraint from 3D Confinements

Many reports of mechanical stress on EMT-TFs have surfaced. Gomez et al. reported a causal role for tissue geometry and endogenous mechanical stress in the spatial patterning of EMT.[201] Gjorevski et al. reviewed how epithelial tissues generate and respond to mechanical stress gradients, and highlighted the mechanisms by which mechanical stress affects EMT necessary for development and disease progression.[202] Ansieau et al. discussed numerous stresses, including mechanical constraints, hypoxia, nutrient depletion and therapeutic treatments in able to affect EMT and EMT-TFs.[203] Li et al. also discussed the role of mechanical forces generated by the cells during EMT.[204] Imani et al. recently carried out a meta-analysis on EMT-TFs studies reported on metastatic breast cancer and highlighted Twist1, Snail1, Snail2, and ZEB1 as key EMT-TFs that are involved in metastatic breast cancer through different signalling cascades.[205] However, none of these studies or current knowledge has attempted to elucidate the relationship between EMT-TFs and mechanical stress from fluid shear stress and mechanical constraints as present in the microcirculation – the route that CTCs take in order to disseminate.

Here, the effects of confinement and constrictions were added to the circulation factor.

SK-BR-3			
	Significance	P value	Q value
Vimentin	No	0.812	0.938
E-cadherin	No	0.755	0.938
N-cadherin	No	0.138	0.358
Snail1	No	0.022	0.254
Snail2	No	0.185	0.358
Twist1	No	0.072	0.277
Twist2	No	0.276	0.455
ZEB1	No	0.633	0.914
ZEB2	No	0.98	1
β-catenin	No	0.044	0.254
MMP-9	No	0.186	0.358
MDA-MB-231			
	Significance	P value	Q value
Vimentin	Yes (Up)	0.016	**0.029**
E-cadherin	No	0.239	0.16
N-cadherin	Yes (Up)	0.042	**0.049**
Snail1	Yes (Down)	0.014	**0.029**
Snail2	Yes (Up)	0.031	**0.046**
Twist1	No	0.134	0.109
Twist2	No	0.107	0.098
ZEB1	Yes (Up)	0.002	**0.015**
ZEB2	Yes (Down)	0.047	**0.049**
β-catenin	Yes (Up)	0.01	**0.029**
MMP-9	No	0.19	0.14

Table 5-3 | Summary of statistical results of confined, circulated cells in 15µm high channels versus unconfined, circulated cells (20µm high channels). Unpaired t-test with Welch's correction followed by the False Discovery Rate (FDR) approach to multiple comparisons (two-stage linear step-up procedure of Benjamini, Krieger and Yekutieli) and significance and confidence level at 0.05. Q values in red denote significant values.

Under confinement (15 µm height), circulated SK-BR-3 cells did not differentially express any target genes when compared to circulated cells that were unconfined (20 µm height). In the same condition, MDA-MB-231 cells however differentially expressed many of the target genes. Interestingly in this configuration (confined), MDA-MB-231 begun to significantly up-regulate several EMT-TFs such as Vimentin, N-cadherin, Snail2 and ZEB1 that were otherwise absent in an unconfined setting. Such triggering of more EMT-TFs suggests that imposing confinement on top of circulation has EMT-inducing effects in MDA-MB-231 cells.

SK-BR-3									
	Confined with 11x20µm-long Constrictions			Confined with 7x40µm-long Constrictions			Confined with 5x60µm-long Constrictions		
	Significance	P value	Q value	Significance	P value	Q value	Significance	P value	Q value
Vimentin	No	0.062	0.098	No	0.213	0.371	No	0.829	0.87
E-cadherin	No	0.68	0.584	No	0.883	0.927	No	0.226	0.705
N-cadherin	No	0.048	0.091	No	0.087	0.292	No	0.709	0.87
Snail1	No	0.025	0.059	No	0.07	0.292	No	0.086	0.549
Snail2	Yes (Down)	0.006	**0.028**	No	0.219	0.371	No	0.531	0.87
Twist1	No	0.016	0.05	No	0.101	0.292	No	0.366	0.705
Twist2	No	0.364	0.382	No	0.54	0.693	No	0.336	0.705
ZEB1	Yes (Down)	0.001	**0.009**	No	0.225	0.371	No	0.352	0.705
ZEB2	No	0.668	0.584	No	0.822	0.927	No	0.796	0.87
β-catenin	No	0.248	0.293	No	0.263	0.38	No	0.095	0.549
MMP-9	No	0.239	0.293	No	0.079	0.292	No	0.674	0.87
MDA-MB-231									
	Confined with 11x20µm-long Constrictions			Confined with 7x40µm-long Constrictions			Confined with 5x60µm-long Constrictions		
	Significance	P value	Q value	Significance	P value	Q value	Significance	P value	Q value
Vimentin	Yes (Up)	0.008	**0.022**	No	0.397	0.313	Yes (Up)	0.014	**0.018**
E-cadherin	No	0.08	0.108	Yes (Down)	0.004	**0.008**	No	0.118	0.077
N-cadherin	No	0.961	0.734	No	0.979	0.561	No	0.689	0.362
Snail1	Yes (Down)	0.003	**0.017**	Yes (Down)	0.012	**0.015**	Yes (Down)	0.001	**0.005**
Snail2	No	0.075	0.108	Yes (Up)	0.003	**0.008**	No	0.769	0.367
Twist1	No	0.6	0.504	No	0.728	0.459	No	0.505	0.295
Twist2	No	0.09	0.108	Yes (Up)	0.002	**0.008**	Yes (Up)	0.021	**0.02**
ZEB1	No	0.115	0.121	Yes (Up)	0.007	**0.011**	Yes (Up)	0.007	**0.012**
ZEB2	Yes (Down)	0.004	**0.017**	No	0.365	0.313	Yes (Down)	0.002	**0.005**
β-catenin	No	0.038	0.08	No	0.647	0.453	Yes (Up)	0.023	**0.02**
MMP-9	No	0.194	0.181	No	0.275	0.289	Yes (Down)	0.034	**0.026**

Table 5-4 | Summary of statistical results of confined, constricted, circulated cells versus unconfined, circulated cells. Unpaired t-test with Welch's correction followed by the False Discovery Rate (FDR) approach to multiple comparisons (two-stage linear step-up procedure of Benjamini, Krieger and Yekutieli) and significance and confidence level at 0.05. Q values in red denote significant values.

Under confinement (15 µm height) and constrictions, increasing numbers of differentially expressed genes were observed in circulated MDA-MB-231 cells with increasing lengths of constrictions. In the same experimental conditions, SK-BR-3 cells did not appear to differentially respond to increasing lengths of constrictions with the exception of Snail2 and ZEB1 that were significantly decreased in the highest curvature of constrictions.

Based on the mechanical phenotyping of SK-BR-3 and MDA-MB-231 cells as reported in chapter three, MDA-MB-231 exhibited more pronounced effects than SK-BR-3 cells when circulated in increasing lengths of constrictions. Here, molecular analyses seem to corroborate these findings, in which more pronounced effects of constrictions, resulted in increasing triggers of EMT-TFs in MDA-MB-231 cells. Indeed, MDA-MB-231 cells required longer time to cross the longer constrictions thereby, having higher residence times in the constrictions. While residence times were also increasing for SK-BR-3 in longer constrictions, it could mean that SK-BR-3 cells require longer circulation and confinement times for significant EMT-TFs to be induced. These results show that different types of breast tumour cells, in this case between SK-BR-3 and MDA-MB-231, respond uniquely to various

lengths of constrictions. This suggests the presence of an optimal type of geometry for each circulating cell type in sensitising specific EMT-TFs. Moreover, the plasticity of EMT in metastasis provides another level of complexity regarding the appropriate time window to target EMT in CTCs in the microcirculation.

Nonetheless, the most interesting finding is the acquisition of EMT-TFs (Vimentin, Twist2, ZEB1 and β-catenin) of circulated, confined and constricted MDA-MB-231 cells in the longest length of constrictions. While this cell line has already presented a mesenchymal-like phenotype from the beginning, the up-regulation of EMT-TFs that are associated with a mesenchymal phenotype has shown that the mechanical constraints from the lowest curvatures in 5 x 60 μm-long constrictions are optimal to further activate the EMT program in circulating MDA-MB-231 cells. Such findings could hint increased metastatic potential and tumourigenicity although follow-up experimental tests are required to ascertain such claims.

Twist2 and not Twist1, expressed differentially in these circulation experiments. Given that Twist2 was less reported than Twist1 in previous literature, Twist2 was chosen as the signature EMT-TF in response to fluid shear stress, mechanical confinement and constrictions for the following analysis on its protein localisation.

The Role of Transcription Factors Twist in Cancer Cells

Twist1 and Twist2 are two nuclear proteins playing the role of distinct tissue-restricted transcription factor members of the basic helix-loop-helix (bHLH) class B family that display high sequence similarity with each other.[206] They play a critical role in embryogenesis, particularly in the inhibition of mesenchymal cell development.[206] In adult tissues, mutations in Twist1 cause the Saethre–Chotzen syndrome, an autosomal dominant inheritance disease principally characterised by craniosynostosis (a premature closure of clavarial suture).[207] Twist2 is expressed after Twist1 in mesodermal tissues during embryogenesis.[206] Twist2 inhibits terminal differentiation of mesoderm-derived cells, such as myocytes, osteoblasts and adipocytes.[208–211] In adult tissues, mutations in Twist2 are associated with the Setleis Syndrome, an inherited developmental disorder characterised by bilateral temporal marks and other facial features.[212]

The central role of Twist1 and Twist2 in embryogenesis and mesodermal development, and their targeting of multiple genes coding for cell-fate proteins inevitably links them to cancer and oncogenesis. In cancer cells where Twist1 or Twist2 expression is increased, it has been demonstrated that they neutralize senescence and cell death through inhibition of both p53 and Rb tumor suppressor pathways.[213] They have also been implicated in metastasis formation through EMT, thereby facilitating cancer cell invasion in epithelium-based cancers.[158,196]

The action mechanism of Twist is illustrated in the following Figure 5-14.

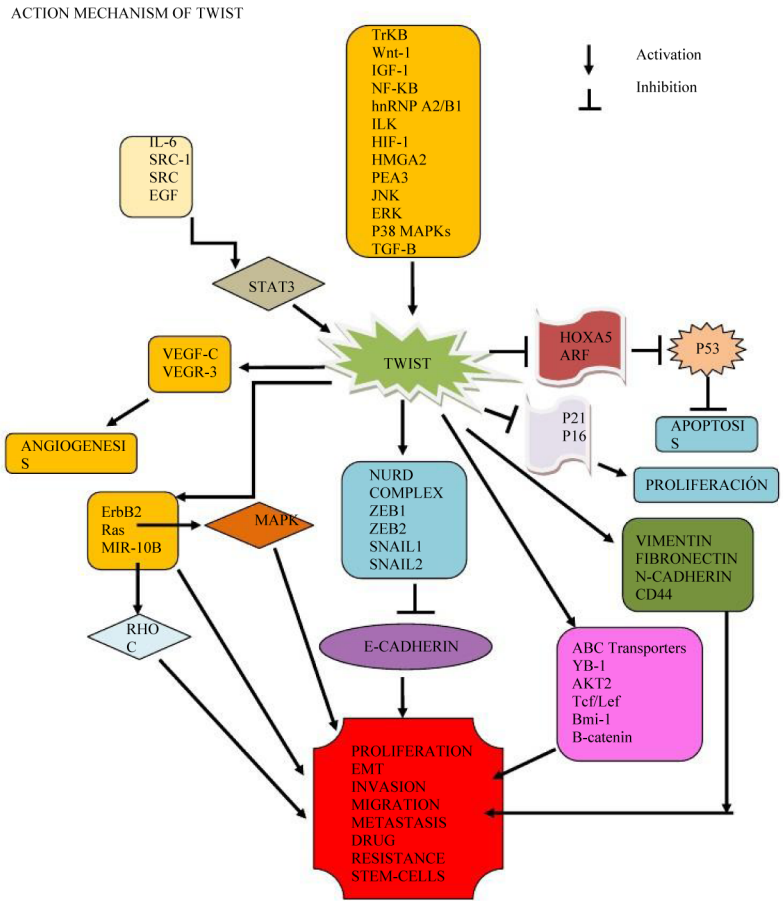

Figure 5-14 | Twist Signalling. The interaction of Twist with different proteins and mechanisms that could act in promoting several cellular reactions such as apoptosis, proliferation, EMT, invasion, migration, metastasis, drug resistance and stem-cell development.[214]

Here, the localisation of Twist2 protein was determined in SK-BR-3 and MDA-MB-231 cells in response to fluid shear stress alone, and to the combination of fluid shear stress and mechanical constraints. Their NC ratios of Twist2 protein were measured and compared in the following Figure 5-15. Circulated SK-BR-3 cells exhibited nuclear translocation of Twist2 while circulated MDA-MB-231 cells exhibited cytoplasmic translocation of Twist2. Furthermore, total Twist2 protein expression increases in longer constrictions as shown in the following Figure 5-16.

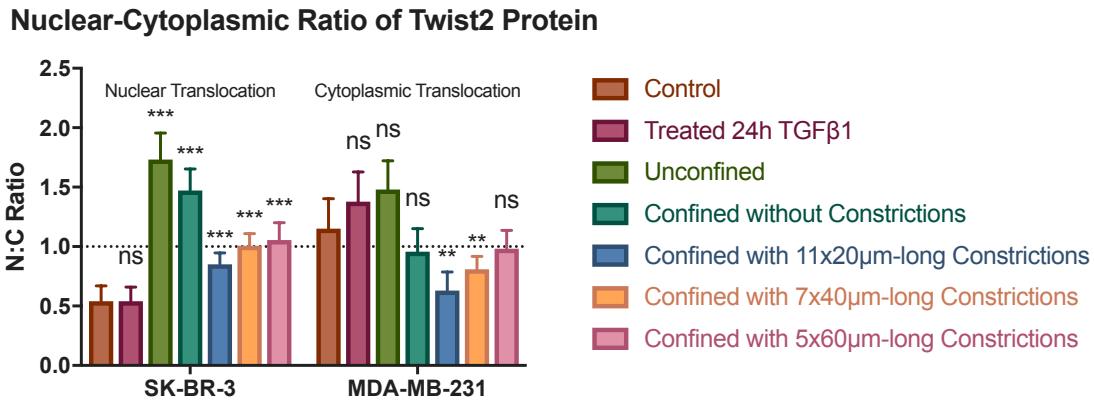

Figure 5-15. Comparison of NC ratio of Twist2 protein between SK-BR-3 and MDA-MB-231 cells uncirculated (without fluid shear stress) and circulated (with fluid shear stress). Control (n=65, 63), treated – TGFβ1: 10ng/ml (n=65, 121), unconfined (n=84, 70), confined: without constrictions (n=92, 62), confined – type 1: with 11x20µm-long constrictions (n=71, 27), confined – type 2: with 7x40µm-long constrictions (n=94, 123), and confined – type 3: with 5x60µm-long constrictions (n=44, 124) for SK-BR-3 and MDA-MB-231 cells respectively. Error bars represent 95% confidence interval. Kruskal-Wallis test ($p<0.001$) and Dunn's multiple comparisons post hoc test. **, significance level at 0.01; ***, significance level at 0.001; ns, not significant.

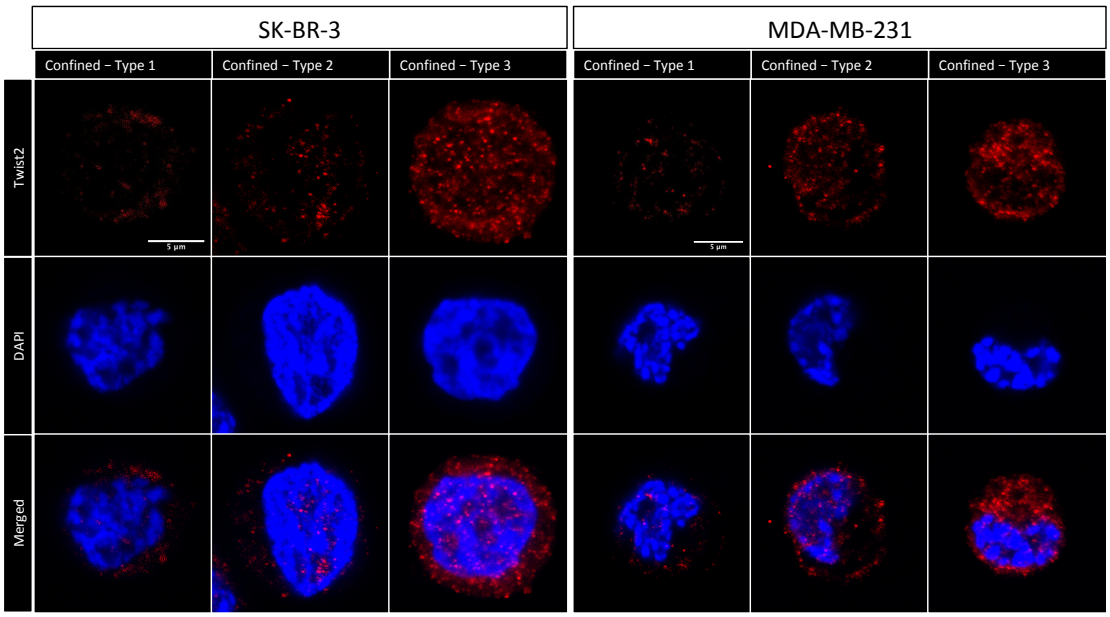

Figure 5-16. Twist2 and DAPI staining of SK-BR-3 (left panel) and MDA-MB-231 (right panel) cells post-circulation and post-constrictions. Confined – type 1: with 11x20µm-long constrictions, confined – type 2: with 7x40µm-long constrictions, and confined – type 3: with 5x60µm-long constrictions.

Circulated SK-BR-3 cells presented significant increase in NC ratio of Twist2 in all geometrical types when compared to uncirculated control cells ($p<0.001$ for all types). Higher NC ratio of Twist2 protein suggests nuclear translocation or accumulation of Twist2 protein in the nucleus. Mao et al. reported that nuclear Twist2 were detected in cancer cells located at the invasive margins of primary breast cancer.[215] This suggests a link between

nuclear Twist2 and EMT in circulating SK-BR-3 through mechanical constraints. It was also reported that the EMT program might be activated transiently through nuclear Twist2 in the tumour invasion front to facilitate cancer cell invasion and metastasis.[215] However, gene expression did not show differentially expressed Twist2 in SK-BR-3 cells from exposure to all types of constrictions. This is not consistent with the immunostaining data that showed marked Twist2 staining. It has been common practice to use mRNA concentrations as proxies for the concentrations and activities of the corresponding proteins, thereby assuming that transcript abundances are the main determinant of protein abundances. Nonetheless in general, they do not correlate strongly and it has been reported that the lack of correlation between RNA and protein concentration in single cells can be explained by the different lifetimes of the molecules.[216]

Circulated MDA-MB-231 cells however, presented an inverse pattern, in which Twist2 protein accumulates in the cytoplasm. The NC ratios of Twist2 protein are significantly decreased in the geometry of confined – type 1 channels ($p<0.01$) and confined – type 2 channels ($p<0.01$). Lower NC ratio of Twist2 protein suggests cytoplasmic translocation. Cytoplasmic Twist2 was reported at the tumour centre of primary breast carcinomas and lymph metastases that contributed to the maintenance of epithelial cancer characteristics expressing E-cadherin in a non-invasive state.[215] Hence, reports on cytoplasmic Twist2 could suggest a MET program in circulating MDA-MB-231 cells through mechanical constraints.

5.5 Conclusion

Transient TGFβ1 treatment significantly reduced β-catenin expression in SK-BR-3 cells. It was reported that the down-regulation of β-catenin decreases tumourigenicity but still promotes EMT.[181] However, MDA-MB-231 cells presented significant increase in β-catenin expression, which is consistent with more invasive and higher migratory potential phenotypes.[183] Vimentin was also significantly increased in MDA-MB-231 cells, which is consistent with the report that β-catenin up-regulates the Vimentin promoter[183] and that MDA-MB-231 cells are mesenchymal-like in morphology. In EMT process[155], Snail1 directly targets ZEB1.[34] However, MDA-MB-231 cells presented significant decrease in Snail1 expression. It was proposed that Snail1 up-regulation is not necessary to maintain a mesenchymal phenotype.[185–188] Therefore, MDA-MB-231 cells that already have abundant Vimentin expression may not require Snail1 up-regulation for EMT.

In fluid shear stress only experiments, SK-BR-3 cells significantly expressed E-cadherin even when they are thought to harbour a genetic deletion of one allele in *CDH1*, the E-cadherin-encoding gene, resulting in absence of expression.[193] This suggests that fluid shear stress can re-express E-cadherin in SK-BR-3 cells, which should be validated with immunofluorescence data in the future work. SK-BR-3 cells also significantly expressed β-catenin in response to fluid shear stress. Presence of mutant variants of E-cadherin can disrupt binding with β-catenin that leads to nuclear translocation of β-catenin triggering the formation of transcriptional factors downstream of the Wnt pathway such as Snail1, ZEB1 and ZEB2.[157] These EMT-TFs were also up-regulated in SK-BR-3 and MDA-MB-231 cells in response to fluid shear stress. In addition, ZEB1 functions as a master regulator of epithelial plasticity in

cancer cell invasion and human tumour progression *in vivo*.[157] For Twist1[196] and Twist2[197], not only that they have been reported to induce EMT alone or cooperatively, their over-expression results in the induction of EMT and increases the generation of breast cancer cells with stem-like characteristics in the tumour microcirculation.[198] However, Twist2 was only differentially expressed in MDA-MB-231 cells, which suggests unique roles for Twist1 and Twist2. It could also mean that in circulation, Twist2 could be the main EMT regulator over Twist1.

In cancer cells where Twist1 or Twist2 expression is increased, it has been demonstrated that they neutralise senescence and cell death through inhibition of both p53 and Rb tumor suppressor pathways.[213] They have also been implicated in metastasis formation through EMT, thereby facilitating cancer cell invasion in epithelium-based cancers. Nuclear Twist2 were detected in cancer cells located at the invasive margins of primary breast cancer[215]. This suggests a link between nuclear Twist2 and EMT in circulating SK-BR-3 through mechanical constraints. As SK-BR-3 cells exhibit epithelial-like morphology, it is safe to hypothesise that its next transition phase would be towards mesenchymal traits. On the other hand, cytoplasmic Twist2 was reported at the tumour centre of primary breast carcinomas and lymph metastases that contributed to the maintenance of epithelial cancer characteristics expressing E-cadherin in a non-invasive state[215]. This however, suggests a link between cytoplasmic Twist2 and MET in circulating MDA-MB-231 cells through mechanical constraints. As MDA-MB-231 cells exhibit mesenchymal-like morphology, it is then safe to hypothesise that its next transition phase would be back to epithelial traits. Furthermore, Twist2 increase was reported in MDA-MB-231 cells from longer constrictions. This trend also coincides with longer times of cell arrest, which in turn suggests a more favourable configuration for the extravasation process.

Novel insights on the implications and localisations of Twist2 in response to fluid shear stress and mechanical confinements in two different types of breast cancer cells can shed new light in understanding CTCs and dissemination in the microcirculation. Furthermore, Twist2 has shown to be a promising new target for diagnostic and/or therapeutic interventions. While incomplete or partial EMT can explain the co-expression of epithelial and mesenchymal markers, the presence or absence of a specific EMT-TF should not be explicitly used as a threshold to define if EMT is activated or not. This is because EMT can be induced by multiple extracellular cues that converge in the activation of a plethora of EMT-TFs that belong to different gene families. As seen in the earlier results, several EMT-TFs were activated coherently while others seemed to be independent of each other. Nonetheless, such results should not be taken wholly but as hints to explore other means in addressing the mechanisms of the EMT program in metastasis.

In summary, MDA-MB-231 cells are more responsive than SK-BR-3 cells to fluid shear stress and mechanical confinement and constrictions. First, mechanical constraints and constrictions were shown to trigger more differentially expressed EMT-TFs in geometries of increasing constriction length. This provides evidence that the imposed mechanical constraints from constrictions could induce changes in cells on the molecular level. Second, despite observable changes in cellular shape and deformability from the imposed mechanical constraints and constrictions, changes in cells on the molecular level depend on the type and initial state of cells. This raises the question of how the determination of cell fate is regulated in CTCs while in the microcirculation. As aforementioned, the half-life of CTCs is short and the heterogeneity of CTCs has been widely reported even within the same population of cells. Therefore, the extravasation process has to well occur or at least begin within the given

timeframe. The question is why, when, where and how. From this chapter, the next major step would be to test the invasion and migratory potentials of cells with differentially expressed EMT-TFs after crossing mechanical constraints and constrictions in order to see how they fair.

In the next and last chapter, a summary of all of the discussions from this thesis along with future perspectives will be addressed.

CHAPTER SIX: GENERAL DISCUSSION

6.1 Overview of Key Findings

Changes in Nuclear Morphology under Shear Stress and Confinement

The nucleus is the most important organelle in the cell. It contains the genetic material, the DNA, which is responsible for controlling and directing all the activities of the cell. It is the most prominent organelle as compared to other cell organelles, and accounts for at least 10% of the cell's volume. It has been reported that cells require nuclear deformation to squeeze through tissue matrices, in which 3D environments control the deformability and the mechanical properties of the nucleus.[217] Here, we reported that fluid shear stress combined with mechanical confinement, modified durably enough the nucleus area of flow-induced migrating cells to be able to see significant changes even after re-attachment and fixation of these cells (Table 6-1). Under circulation and confinement, SK-BR-3 presented a significant increase of nucleus area while MDA-MB-231 cells displayed the inverse tendency. It is noteworthy that such differences could affect the migration behaviour of cells over longer duration of circulation within constrictions, as increased volume and surface area in the first encountered constrictions (or during the first complete circulation) could in turn affect the flow resistance experienced by the cells in subsequent narrowing of blood vessels (or further circulations) through a positive feedback process. Besides, such large changes in nuclear shape or increases in nuclear volume might increase mechanical tension in the nuclear envelope. Interestingly, it has been recently shown that such mechanosensitive response was implied in cell inflammatory response through the translocation of cytosolic proteins into the nuclear membrane.[218] Therefore, any changes in the nucleus shape might have important consequences in terms of cell fate. This in turn suggests that the nucleus of CTCs may

undergo changes in the blood circulation that may play a significant role in the metastatic process, thus calls for further studies in this direction.

Deformability Affects the Residence Time of Flow-Induced Migration of Tumour Cells in Micro Constrictions

While cell and nucleus areas could affect the speed of migration, deformability characteristics of a cell greatly influence the time required for it to cross through micro constrictions. Here, we demonstrated that longer lengths of constrictions resulted in significant increase in cell residence time in a micro channel (Table 6-2 and Table 6-3). It has been reported that nuclear deformability constitutes a rate-limiting step during spontaneous cell migration in 3D environments.[90] In our own experiments under flow, MDA-MB-231 showed higher deformability characteristics as compared to SK-BR-3 cells. Moreover, it is worth noting that both cell types were of comparable sizes before circulation, yet they presented a marked physical size distinction post-circulation. Given such a contrast, it raises questions regarding the extents to which the deformability of cells affects their potential to remain in circulation, to be blocked in the microvasculature, and finally how these may affect their extravasation potential.

Revelation of the Morphological Architecture of a Shape Memory

Aside from presenting increased residence times in longer lengths of constrictions, a significant percentage of time was spent in the first constriction as compared to the rest of the constrictions in the micro channel (Table 6-2 and Table 6-3). Hence, the cells revealed a shape memory. Although very little is known about the underlying mechanisms for such

shape memory, it has been reported that in cellular mechanotransduction, cell tension modulates mechanosensitive transcription factors that contribute to the storage of a shape memory of past mechanical extracellular matrix interactions.[219] Further work will be needed to investigate if such mechanisms are at play here, or if this shape memory relies on a more physical plasticity of chromatin.

Cell Type	SK-BR-3		Two-Way ANOVA followed by Sidak's Multiple Comparisons Test		MDA-MB-231		Two-Way ANOVA followed by Sidak's Multiple Comparisons Test	
Experimental Group / Analysed Parameters	Circulated and Unconfined	Circulated and Confined	Adjusted P Values	Significance Levels	Circulated and Unconfined	Circulated and Confined	Adjusted P Values	Significance Levels
Cell Area	162.1 μm^2	178.5 μm^2	<0.001	***	133.4 μm^2	128.9 μm^2	0.506	ns
Nucleus Area	86.13 μm^2	105.1 μm^2	<0.001	***	59.95 μm^2	52.5 μm^2	0.049	*
NC Ratio (Area)	1.186	1.667	>0.999	ns	0.9388	0.7699	>0.999	ns
Nucleus AR	1.35	1.344	>0.999	ns	1.52	1.668	>0.999	ns
Velocity	18.2 mm/s	9.853 mm/s	0.653	ns	18.43 mm/s	8.102 mm/s	0.045	*
Residence Time	24 ms	46 ms	0.001	**	23.67 ms	52.62 ms	<0.001	***

Table 6-1 | The effects of confinement on the morphology and speed of breast tumour cells in the microcirculation. All results express the mean values of each condition. NC: nucleus to cytoplasm. AR: aspect ratio. *, significance level at 0.05; **, significance level at 0.01; ***, significance level at 0.001; ns, not significant.

Cell Type	SK-BR-3			Two-Way ANOVA followed by Tukey's Multiple Comparisons Test		
Constrictions (No. x Length) / Analysed Parameters	11 x 20 µm-long	7 x 40 µm-long	5 x 60 µm-long	11 x 20 µm-long vs 7 x 40 µm-long	11 x 20 µm-long vs 5 x 60 µm-long	7 x 40 µm-long vs 5 x 60 µm-long
				Adjusted P Values and Significance Levels		
Cell Area	141.6 μm^2	146 μm^2	148 μm^2	0.995 (ns)	0.993 (ns)	>0.999 (ns)
Nucleus Area	67.16 μm^2	71.66 μm^2	73.12 μm^2	0.995 (ns)	0.994 (ns)	>0.999 (ns)
NC Ratio (Area)	1.002	1.072	1.064	>0.999 (ns)	>0.999 (ns)	>0.999 (ns)
Nucleus AR	1.401	1.388	1.324	>0.999 (ns)	>0.999 (ns)	>0.999 (ns)
Velocity	4.862 mm/s	3.835 mm/s	2.816 mm/s	>0.999 (ns)	>0.999 (ns)	>0.999 (ns)
Residence Time	204 ms	438 ms	661.7 ms	<0.001 (***)	<0.001 (***)	0.055 (ns)
Residence Time (FC)	115.6 ms	357.5 ms	497.5 ms	<0.001 (***)	<0.001 (***)	0.317 (ns)
Percentage of Residence Time (FC)	41 %	53.6 %	54.79 %	0.973 (ns)	0.988 (ns)	>0.999 (ns)

Table 6-2 | The effects of constrictions on the morphology and speed of SK-BR-3 breast tumour cells in the microcirculation. All results express the mean values of each condition. NC: nucleus to cytoplasm. AR: aspect ratio. FC: first constriction. *, significance level at 0.05; **, significance level at 0.01; ***, significance level at 0.001; ns, not significant.

Cell Type	MDA-MB-231			Two-Way ANOVA followed by Tukey's Multiple Comparisons Test		
Constrictions (No. x Length) / Analysed Parameters	11 x 20 µm-long	7 x 40 µm-long	5 x 60 µm-long	11 x 20 µm-long vs 7 x 40 µm-long	11 x 20 µm-long vs 5 x 60 µm-long	7 x 40 µm-long vs 5 x 60 µm-long
				Adjusted P Values and Significance Levels		
Cell Area	98.35 μm^2	103.1 μm^2	127 μm^2	0.978 (ns)	0.439 (ns)	0.204 (ns)
Nucleus Area	34.66 μm^2	41.29 μm^2	56.25 μm^2	0.957 (ns)	0.626 (ns)	0.535 (ns)
NC Ratio (Area)	0.6417	0.8092	0.9999	>0.999 (ns)	>0.999 (ns)	>0.999 (ns)
Nucleus AR	1.674	1.594	1.504	>0.999 (ns)	>0.999 (ns)	>0.999 (ns)
Velocity	7.934 mm/s	6.362 mm/s	4.61 mm/s	0.998 (ns)	0.992 (ns)	0.997 (ns)
Residence Time	73.33 ms	95.53 ms	218.7 ms	0.664 (ns)	<0.001 (***)	<0.001 (***)
Residence Time (FC)	33.67 ms	52.34 ms	171.6 ms	0.749 (ns)	<0.001 (***)	<0.001 (***)
Percentage of Residence Time (FC)	38.92 %	43.56 %	55.37 %	0.982 (ns)	0.814 (ns)	0.875 (ns)

Table 6-3 | The effects of constrictions on the morphology and speed of MDA-MB-231 breast tumour cells in the microcirculation. All results express the mean values of each condition. NC: nucleus to cytoplasm. AR: aspect ratio. FC: first constriction. *, significance level at 0.05; **, significance level at 0.01; ***, significance level at 0.001; ns, not significant.

Activity of DNA Damage Repair Mechanism is Dependent on the Residence Time of Flow-Induced Migration of Tumour Cells in Micro Constrictions

Preservation of genome integrity is an essential process for cell homeostasis. To ensure genome stability, cells use a global signalling network, namely the DNA damage response (DDR) to sense and repair DNA damage.[220] Spontaneous migration-induced DNA damage and repair from constrictions has been reported[92,93] in cancer cell clones to cause heritable changes that affect cell shape.[94] Here, we demonstrated that while a certain dosage of fluid shear stress showed decreased activity of DNA damage repair mechanism, its increased activity depended on the residence time of flow-induced migration of cells (Table 6-4, Table 6-5 and Table 6-6). Nonetheless, having more γH2AX might mean that the cells 1) experience more damages, 2) have better damage response as in a more likely scenario, cells having less γH2AX are defective in damage detection and response[221,222], or 3) the damage signal persists longer due to inefficiency in damage repair or recovery from damage. Therefore, specific experiments will be required to distinguish these possibilities.

Cell Type	SK-BR-3		Two-Way ANOVA followed by Sidak's Multiple Comparisons Test		MDA-MB-231		Two-Way ANOVA followed by Sidak's Multiple Comparisons Test	
Experimental Group / Analysed Parameters	Circulated and Unconfined	Circulated and Confined	Adjusted P Values	Significance Levels	Circulated and Unconfined	Circulated and Confined	Adjusted P Values	Significance Levels
Nucleus Integrated Density (γH2AX)	6404	6750	0.920	ns	4417	3731	0.324	ns
Cytoplasm Integrated Density (γH2AX)	7261	3238	<0.001	***	2290	3689	0.005	**
NC Ratio (γH2AX)	0.9657	2.2	>0.999	ns	1.966	1.122	>0.999	ns

Table 6-4 | The effects of confinement on the DNA damage repair mechanism of breast tumour cells in the microcirculation. All results express the mean values of each condition. Integrated density: the product of area and mean gray value. NC: nucleus to cytoplasm. *, significance level at 0.05; **, significance level at 0.01; ***, significance level at 0.001; ns, not significant.

Cell Type	SK-BR-3			Two-Way ANOVA followed by Tukey's Multiple Comparisons Test		
Constrictions (No. x Length)	11 x 20 µm-long	7 x 40 µm-long	5 x 60 µm-long	11 x 20 µm-long vs 7 x 40 µm-long	11 x 20 µm-long vs 5 x 60 µm-long	7 x 40 µm-long vs 5 x 60 µm-long
Analysed Parameters				Adjusted P Values and Significance Levels		
Nucleus Integrated Density (γH2AX)	2165	4821	6517	<0.001 (***)	<0.001 (***)	0.002 (**)
Cytoplasm Integrated Density (γH2AX)	1583	3186	7094	<0.001 (***)	<0.001 (***)	<0.001 (***)
NC Ratio (γH2AX)	1.427	1.596	0.9926	>0.999 (ns)	>0.999 (ns)	>0.999 (ns)

Table 6-5 | The effects of constrictions on the DNA damage repair mechanism of SK-BR-3 breast tumour cells in the microcirculation. All results express the mean values of each condition. Integrated density: the product of area and mean gray value. NC: nucleus to cytoplasm. *, significance level at 0.05; **, significance level at 0.01; ***, significance level at 0.001; ns, not significant.

Cell Type	MDA-MB-231			Two-Way ANOVA followed by Tukey's Multiple Comparisons Test		
Constrictions (No. x Length)	11 x 20 µm-long	7 x 40 µm-long	5 x 60 µm-long	11 x 20 µm-long vs 7 x 40 µm-long	11 x 20 µm-long vs 5 x 60 µm-long	7 x 40 µm-long vs 5 x 60 µm-long
Analysed Parameters				Adjusted P Values and Significance Levels		
Nucleus Integrated Density (γH2AX)	1597	3627	3361	<0.001 (***)	<0.001 (***)	0.566 (ns)
Cytoplasm Integrated Density (γH2AX)	1058	4222	2529	<0.001 (***)	<0.001 (***)	<0.001 (***)
NC Ratio (γH2AX)	1.606	1.02	1.486	>0.999 (ns)	>0.999 (ns)	>0.999 (ns)

Table 6-6 | The effects of constrictions on the DNA damage repair mechanism of MDA-MB-231 breast tumour cells in the microcirculation. All results express the mean values of each condition. Integrated density: the product of area and mean gray value. NC: nucleus to cytoplasm. *, significance level at 0.05; **, significance level at 0.01; ***, significance level at 0.001; ns, not significant.

Flow-Induced Migration of Tumour Cells in Micro Constrictions Modulates Total Twist2 Protein

It has been shown that the EMT transcription factor Twist2 is overexpressed in breast cancer cells.[197] Additionally, mechanical stress induces Twist expression in Drosophila melanogaster epithelia[223] but to our knowledge, no data has yet shown how mechanical stress coupled with mechanical flow affect Twist expression in cancer cells. Here, we examined the localisation of Twist2 protein in breast tumour cells post-circulation, and we found that mechanical flow resulted in a significant decrease of nuclear Twist2 (Table 6-7). Nevertheless, nuclear and cytoplasmic Twist2 progressively and significantly increased in longer constriction lengths (Table 6-8 and Table 6-9). Furthermore, we believe that the significant increase in total Twist2 protein expression in cells experiencing higher residence time in the channels is a priming factor that is consistent with the notion of mechanical cell arrest prior to extravasation.

Cell Type	SK-BR-3		Two-Way ANOVA followed by Sidak's Multiple Comparisons Test		MDA-MB-231		Two-Way ANOVA followed by Sidak's Multiple Comparisons Test	
Experimental Group / Analysed Parameters	Circulated and Unconfined	Circulated and Confined	Adjusted P Values	Significance Levels	Circulated and Unconfined	Circulated and Confined	Adjusted P Values	Significance Levels
Nucleus Integrated Density (Twist2)	1558	626.6	<0.001	***	930.4	643.3	<0.001	***
Cytoplasm Integrated Density (Twist2)	939.3	525.2	<0.001	***	774.5	850.5	0.624	ns
NC Ratio (Twist2)	1.732	1.472	>0.999	ns	1.481	0.9574	>0.999	ns

Table 6-7 | The effects of confinement on the translation and localisation of Twist2 protein of breast tumour cells in the microcirculation. All results express the mean values of each condition. Integrated density: the product of area and mean gray value. NC: nucleus to cytoplasm. *, significance level at 0.05; **, significance level at 0.01; ***, significance level at 0.001; ns, not significant.

Cell Type	SK-BR-3			Two-Way ANOVA followed by Tukey's Multiple Comparisons Test		
Constrictions (No. x Length)	11 x 20 µm-long	7 x 40 µm-long	5 x 60 µm-long	11 x 20 µm-long vs 7 x 40 µm-long	11 x 20 µm-long vs 5 x 60 µm-long	7 x 40 µm-long vs 5 x 60 µm-long
Analysed Parameters				Adjusted P Values and Significance Levels		
Nucleus Integrated Density (Twist2)	142.9	367.6	446.6	<0.001 (***)	<0.001 (***)	0.002 (**)
Cytoplasm Integrated Density (Twist2)	194	403.8	437	<0.001 (***)	<0.001 (***)	0.315 (ns)
NC Ratio (Twist2)	0.8505	1.008	1.055	>0.999 (ns)	>0.999 (ns)	>0.999 (ns)

Table 6-8 | The effects of constrictions on the translation and localisation of Twist2 protein of SK-BR-3 breast tumour cells in the microcirculation. All results express the mean values of each condition. Integrated density: the product of area and mean gray value. NC: nucleus to cytoplasm. *, significance level at 0.05; **, significance level at 0.01; ***, significance level at 0.001; ns, not significant.

Cell Type	MDA-MB-231			Two-Way ANOVA followed by Tukey's Multiple Comparisons Test		
Constrictions (No. x Length)	11 x 20 µm-long	7 x 40 µm-long	5 x 60 µm-long	11 x 20 µm-long vs 7 x 40 µm-long	11 x 20 µm-long vs 5 x 60 µm-long	7 x 40 µm-long vs 5 x 60 µm-long
Analysed Parameters				Adjusted P Values and Significance Levels		
Nucleus Integrated Density (Twist2)	98.11	297.1	406.2	<0.001 (***)	<0.001 (***)	0.001 (**)
Cytoplasm Integrated Density (Twist2)	180.1	456.9	567.2	<0.001 (***)	<0.001 (***)	<0.001 (***)
NC Ratio (Twist2)	0.6308	0.8103	0.9829	>0.999 (ns)	>0.999 (ns)	>0.999 (ns)

Table 6-9 | The effects of constrictions on the translation and localisation of Twist2 protein of MDA-MB-231 breast tumour cells in the microcirculation. All results express the mean values of each condition. Integrated density: the product of area and mean gray value. NC: nucleus to cytoplasm. *, significance level at 0.05; **, significance level at 0.01; ***, significance level at 0.001; ns, not significant.

Fluid Shear Stress and Mechanical Constraints Induce Changes in EMT-Related Markers in Specific Tumour Cells

Here, we found that changes of EMT-related genes were more pronounced in MDA-MB-231 than in SK-BR-3 cells (Table 6-10 and Table 6-11). Despite exhibiting 1) more time to cross constrictions, 2) less deformability characteristics, and 3) higher activity of DNA damage repair mechanism than MDA-MB-231, SK-BR-3 cells seemed more resistant towards changes on the molecular level. As aforementioned, there are several possibilities of having more γH2AX and SK-BR-3 seemed to have an efficient damage response or that the imposed nuclear morphology changes into micro constrictions were not sufficient to induce EMT changes. On a different level, non-observable changes in EMT-related markers do not directly mean that cells were not induced on the molecular level but EMT-related markers might not be targets of interest in specific cells from fluid shear stress and mechanical constraints.

SK-BR-3										
Experimental Group	Circulated and Unconfined vs Uncirculated and Unconfined		Circulated and Confined vs Circulated and Unconfined		11 x 20 µm-long vs Circulated and Unconfined		7 x 40 µm-long vs Circulated and Unconfined		5 x 60 µm-long vs Circulated and Unconfined	
EMT-related Genes	P Values	Q Values	P Values	Q Values	P Values	Q Values	P Values	Q Values	P Values	Q Values
Vimentin	0.338	0.327915	0.812	0.938	0.062	0.098	0.213	0.371	0.829	0.87
E-cadherin	**0.000131**	**0.001238**	0.755	0.938	0.68	0.584	0.883	0.927	0.226	0.705
N-cadherin	0.347	0.327915	0.138	0.358	**0.048**	0.091	0.087	0.292	0.709	0.87
Snail1	**0.036**	0.08505	**0.022**	0.254	**0.025**	0.059	0.07	0.292	0.086	0.549
Snail2	0.301	0.327915	0.185	0.358	**0.006**	**0.028**	0.219	0.371	0.531	0.87
Twist1	0.499	0.428686	0.072	0.277	**0.016**	0.05	0.101	0.292	0.366	0.705
Twist2	0.057	0.10773	0.276	0.455	0.364	0.382	0.54	0.693	0.336	0.705
ZEB1	**0.014**	**0.0441**	0.633	0.914	**0.001**	**0.009**	0.225	0.371	0.352	0.705
ZEB2	0.167	0.22545	0.98	1	0.668	0.584	0.822	0.927	0.796	0.87
β-catenin	**0.007**	**0.033075**	**0.044**	0.254	0.248	0.293	0.263	0.38	0.095	0.549
MMP-9	0.153	0.22545	0.186	0.358	0.239	0.293	0.079	0.292	0.674	0.87
Mean Residence Time	24 ms		46 ms		204 ms		438 ms		661.7 ms	

Table 6-10 | The effects of circulation, confinement and constrictions on the expression of EMT-related genes of SK-BR-3 breast tumour cells. Unpaired t-test with Welch's correction followed by the False Discovery Rate (FDR) approach to multiple comparisons (two-stage linear step-up procedure of Benjamini, Krieger and Yekutieli) and significance and confidence level at 0.05. Q values coloured and underlined denote significant values: green – significant increase and red – significant decrease.

MDA-MB-231										
Experimental Group	Circulated and Unconfined vs Uncirculated and Unconfined		Circulated and Confined vs Circulated and Unconfined		11 x 20 µm-long vs Circulated and Unconfined		7 x 40 µm-long vs Circulated and Unconfined		5 x 60 µm-long vs Circulated and Unconfined	
EMT-related Genes	P Values	Q Values	P Values	Q Values	P Values	Q Values	P Values	Q Values	P Values	Q Values
Vimentin	0.225	0.1771875	**0.016**	**0.029**	**0.008**	**0.022**	0.397	0.313	**0.014**	**0.018**
E-cadherin	0.305	0.19415455	0.239	0.16	0.08	0.108	**0.004**	**0.008**	0.118	0.077
N-cadherin	**0.0009671**	**0.00203091**	**0.042**	**0.049**	0.961	0.734	0.979	0.561	0.689	0.362
Snail1	**0.0006645**	**0.00203091**	**0.014**	**0.029**	**0.003**	**0.017**	**0.012**	**0.015**	**0.001**	**0.005**
Snail2	0.33	0.19415455	**0.031**	**0.046**	0.075	0.108	**0.003**	**0.008**	0.769	0.367
Twist1	**0.008**	**0.01008**	0.134	0.109	0.6	0.504	0.728	0.459	0.505	0.295
Twist2	**0.029**	**0.03045**	0.107	0.098	0.09	0.108	**0.002**	**0.008**	**0.021**	**0.02**
ZEB1	0.072	0.0648	**0.002**	**0.015**	0.115	0.121	**0.007**	**0.011**	**0.007**	**0.012**
ZEB2	**0.00006361**	**0.00040074**	**0.047**	**0.049**	**0.004**	**0.017**	0.365	0.313	**0.002**	**0.005**
β-catenin	0.339	0.19415455	**0.01**	**0.029**	**0.038**	0.08	0.647	0.453	**0.023**	**0.02**
MMP-9	**0.008**	**0.01008**	0.19	0.14	0.194	0.181	0.275	0.289	**0.034**	**0.026**
Mean Residence Time	23.67 ms		52.62 ms		73.33 ms		95.53 ms		218.7 ms	

Table 6-11 | The effects of circulation, confinement and constrictions on the expression of EMT-related genes of MDA-MB-231 breast tumour cells. Unpaired t-test with Welch's correction followed by the False Discovery Rate (FDR) approach to multiple comparisons (two-stage linear step-up procedure of Benjamini, Krieger and Yekutieli) and significance and confidence level at 0.05. Q values coloured and underlined denote significant values: green – significant increase and red – significant decrease.

6.2 Future Directions

In conclusion, flowing cancer cells from cell lines in micro channels, in conditions tailored to mimic those encountered in the blood flow, has shown significant impacts on cellular processes that can lead to changes in morphological features and genetic expressions. More specifically, this circulation process encompasses 1) the hydrodynamic shear stress from blood flow and 2) the mechanical deformations from the geometrical constrictions of the microvasculature. Furthermore, changes in morphological features and genetic expressions from this circulation process differ from one cell type to another. Notably, two cell lines presenting an epithelial-like and mesenchymal-like state respectively have different responses to these stressors. Therefore, our work strongly suggests that the mechanical process of circulation in the blood flow may have a significant effect on cells. Since, except for dissemination through the lymphatic system, circulation in the blood is a necessary step in a large fraction of metastatic dissemination events, our results suggest that this step should not be ignored when trying to comprehend the metastatic process as a whole. Therefore, this deserves further studies.

In direct relation to the work presented here, future research efforts should involve 1) an increase in circulation duration in constrictions, 2) a more detailed study of the morphological recovery of cells post-constrictions, and 3) potential DNA damage repair processes. This raises specific experimental challenges due to the high speed of migration of cells. However, experiments performed during this research thesis, while too preliminary to be presented here, suggest that technical solutions can be found to this challenge. Further future research efforts should also involve 4) a comparison of the migratory potential of cells

before and after transformation by the circulation and constrictions, and eventually 5) the use of CTCs from patients. This latter study is also challenging, due to the rarity of CTCs. Of course, these studies should be performed in the light of and in parallel with the current evolution of the general understanding of the instability of cancer cells and CTCs, and notably the EMT and MET. This should help to achieve a more in-depth understanding of the molecular mechanisms activated or repressed in CTCs in the blood microcirculation from hydrodynamic shear stress and mechanical deformations.

REFERENCES

1. Hennings, H. *et al.* Critical aspects of initiation, promotion, and progression in multistage epidermal carcinogenesis. *Proc. Soc. Exp. Biol. Med.* **202,** 1–8 (1993).
2. Hanahan, D. & Weinberg, R. A. The hallmarks of cancer. *Cell* **100,** 57–70 (2000).
3. Hanahan, D. & Weinberg, R. A. Hallmarks of cancer: The next generation. *Cell* **144,** 646–674 (2011).
4. Nguyen, D. X., Bos, P. D. & Massagué, J. Metastasis: From dissemination to organ-specific colonization. *Nat. Rev. Cancer* **9,** 274–284 (2009).
5. Stephens, P. J. *et al.* Massive genomic rearrangement acquired in a single catastrophic event during cancer development. *Cell* **144,** 27–40 (2011).
6. Chaffer, C. L. & Weinberg, R. a. A perspective on cancer cell metastasis. *Science* **331,** 1559–64 (2011).
7. Leong, L. Clinical Relevance of Targeting Cancer Metastases. in *Madame Curie Bioscience Database* (2013).
8. Valastyan, S. & Weinberg, R. A. Tumor metastasis: Molecular insights and evolving paradigms. *Cell* **147,** 275–292 (2011).
9. Paget, S. The distribution of secondary growths in cancer of the breast. 1889. *Cancer Metastasis Rev.* **2,** 98–101 (1989).
10. Greene, H. S. N. & Harvey, E. K. The Relationship between the Dissemination of Tumor Cells and the Distribution of Metastases. *Cancer Res.* **24,** 799–811 (1964).
11. Lu, W. C., Pardon, E., Gumkowski, F., Kaminska, G. & Kaminski, M. Specificity of adhesion between murine tumor cells and capillary endothelium: An in vitro correlate of preferential metastasis in vivo. *Cancer Res.* **47,** 1492–1496 (1987).

12. Schackert, G. & Fidler, I. Site-specific Metastasis of Mouse Melanomas and a Fibrosarcoma in the Brain or Meninges of Syngeneic Animals. *Cancer Res.* **48,** 3478–3484 (1988).

13. Weiss, L. Comments on hematogenous metastatic patterns in humans as revealed by autopsy. *Clin. Exp. Metastasis* **10,** 191–199 (1992).

14. Langley, R. R. & Fidler, I. J. The seed and soil hypothesis revisited--the role of tumor-stroma interactions in metastasis to different organs. *Int. J. cancer* **128,** 2527–35 (2011).

15. Cohen, S. J. *et al.* Relationship of circulating tumor cells to tumor response, progression-free survival, and overall survival in patients with metastatic colorectal cancer. *J. Clin. Oncol.* **26,** 3213–3221 (2008).

16. Bidard, F.-C. *et al.* Assessment of circulating tumor cells and serum markers for progression-free survival prediction in metastatic breast cancer: a prospective observational study. *Breast Cancer Res.* **14,** R29 (2012).

17. De Bono, J. S. *et al.* Circulating tumor cells predict survival benefit from treatment in metastatic castration-resistant prostate cancer. *Clin. Cancer Res.* **14,** 6302–6309 (2008).

18. Cristofanilli, M. *et al.* Circulating Tumor Cells, Disease Progression, and Survival in Metastatic Breast Cancer. *N. Engl. J. Med.* **351,** 781–791 (2004).

19. Allard, W. J. *et al.* Tumor Cells Circulate in the Peripheral Blood of All Major Carcinomas but not in Healthy Subjects or Patients With Nonmalignant Diseases Tumor Cells Circulate in the Peripheral Blood of All Major Carcinomas but not in Healthy Subjects or Patients With Non. *Clin. Cancer Res.* **10,** 6897–6904 (2005).

20. Tan, S. J. *et al.* Versatile label free biochip for the detection of circulating tumor cells

from peripheral blood in cancer patients. *Biosens. Bioelectron.* **26,** 1701–1705 (2010).

21. Sajay, B. N. G. *et al.* Towards an optimal and unbiased approach for tumor cell isolation. *Biomed. Microdevices* **15,** 699–709 (2013).
22. Autebert, J. *et al.* Lab on a Chip High purity microfluidic sorting and analysis of circulating tumor cells : towards routine. *Lab Chip* **15,** 2090–2101 (2015).
23. Hou, J.-M. *et al.* Circulating Tumor Cells, Enumeration and Beyond. *Cancers (Basel).* **2,** 1236–1250 (2010).
24. Ferreira, M. M., Ramani, V. C. & Jeffrey, S. S. Circulating tumor cell technologies. *Mol. Oncol.* **10,** 374–94 (2016).
25. Shen, Z., Wu, A. & Chen, X. Current detection technologies for circulating tumor cells. *Chem. Soc. Rev.* **46,** 2038–2056 (2017).
26. Alix-Panabières, C. & Pantel, K. Clinical applications of circulating tumor cells and circulating tumor DNA as liquid biopsy. *Cancer Discov.* **6,** 479–491 (2016).
27. Hong, B. & Zu, Y. Detecting circulating tumor cells: current challenges and new trends. *Theranostics* **3,** 377–94 (2013).
28. Chen, L., Bode, A. M. & Dong, Z. Circulating Tumor Cells: Moving Biological Insights into Detection. *Theranostics* **7,** 2606–2619 (2017).
29. Aparicio, L. A. *et al.* Clinical implications of epithelial cell plasticity in cancer progression. *Cancer Lett.* **366,** 1–10 (2015).
30. Hay, E. D. An overview of epithelio-mesenchymal transformation. *Acta Anat. (Basel).* **154,** 8–20 (1995).
31. Thiery, J. P. & Chopin, D. Epithelial cell plasticity in development and tumor progression. *Cancer Metastasis Rev.* **18,** 31–42 (1999).
32. Kalluri, R. & Weinberg, R. a. Review series The basics of epithelial-mesenchymal

transition. *J. Clin. Invest.* **119,** 1420–1428 (2009).

33. Thiery, J. P. Epithelial–mesenchymal transitions in tumour progression. *Nat. Rev. Cancer* **2,** 442–454 (2002).

34. Lamouille, S., Xu, J. & Derynck, R. Molecular mechanisms of epithelial-mesenchymal transition. *Natl. Rev. Mol. Cell Biol.* **15,** 178–196 (2014).

35. Thiery, J. P. & Lim, C. T. Tumor dissemination: An EMT affair. *Cancer Cell* **23,** 272–273 (2013).

36. Au, S. H. *et al.* Clusters of circulating tumor cells traverse capillary-sized vessels. *Proc. Natl. Acad. Sci. U. S. A.* **113,** 4947–52 (2016).

37. Thiery, J. P. Epithelial-mesenchymal transitions in development and pathologies. *Curr Opin Cell Biol* **15,** 740–746 (2003).

38. Iwatsuki, M. *et al.* Epithelial-mesenchymal transition in cancer development and its clinical significance. *Cancer Sci.* **101,** 293–299 (2010).

39. Tomaskovic-Crook, E., Thompson, E. W. & Thiery, J. P. Epithelial to mesenchymal transition and breast cancer. *Breast Cancer Res.* **11,** 213 (2009).

40. Foroni, C., Broggini, M., Generali, D. & Damia, G. Epithelial-mesenchymal transition and breast cancer: Role, molecular mechanisms and clinical impact. *Cancer Treat. Rev.* **38,** 689–697 (2012).

41. Luan Khoo, B. *et al.* Short-term expansion of breast circulating cancer cells predicts response to anti-cancer therapy. *Oncotarget* **6,** 15578–15593 (2015).

42. Friedl, P. & Alexander, S. Cancer invasion and the microenvironment: Plasticity and reciprocity. *Cell* **147,** 992–1009 (2011).

43. Mallini, P., Lennard, T., Kirby, J. & Meeson, A. Epithelial-to-mesenchymal transition: What is the impact on breast cancer stem cells and drug resistance. *Cancer Treat. Rev.*

40, 341–348 (2014).

44. Kölbl, A. C., Jeschke, U. & Andergassen, U. The significance of epithelial-to-mesenchymal transition for circulating tumor cells. *Int. J. Mol. Sci.* **17,** 1–12 (2016).

45. Charpentier, M. & Martin, S. Interplay of Stem Cell Characteristics, EMT, and Microtentacles in Circulating Breast Tumor Cells. *Cancers (Basel).* **5,** 1545–65 (2013).

46. Azevedo, A. S., Follain, G., Patthabhiraman, S., Harlepp, S. & Goetz, J. G. Metastasis of circulating tumor cells: Favorable soil or suitable biomechanics, or both? *Cell Adhes. Migr.* **9,** 345–356 (2015).

47. Zhang, Z. *et al.* Expansion of CTCs from early stage lung cancer patients using a microfluidic co-culture model. *Oncotarget* **5,** 12383–12397 (2014).

48. Steeg, P. S. Tumor metastasis: Mechanistic insights and clinical challenges. *Nat. Med.* **12,** 895–904 (2006).

49. Gassmann, P. & Haier, J. The tumor cell-host organ interface in the early onset of metastatic organ colonisation. *Clin. Exp. Metastasis* **25,** 171–181 (2008).

50. Jain, R. K. Determinants of Tumor Blood Flow : A Review Determinants of Tumor Blood Flow : A Review1. *Cancer Res.* **3890,** 2641–2658 (1988).

51. Krogh, A. The Capillary Blood-Vessels. The Anatomy and Physiology of Capillaries. *Nature* **112,** 270–272 (1923).

52. Pries, A. R. & Secomb, T. W. Blood Flow in Microvascular Networks. in *Comprehensive Physiology* 3–36 (John Wiley & Sons, Inc., 2011). doi:10.1002/cphy.cp020401

53. Thiriet, M. Physiology and Pathophysiology of Microcirculation. in *PanVascular Medicine* 591–637 (Springer Berlin Heidelberg, 2015). doi:10.1007/978-3-642-37078-

6_24

54. Secomb, T. W. & Pries, A. R. The microcirculation: physiology at the mesoscale. *J. Physiol.* **589,** 1047–1052 (2011).

55. Lipowsky, H. H. Microvascular rheology and hemodynamics. *Microcirculation* **12,** 5–15 (2005).

56. Tarbell, J. M., Simon, S. I. & Curry, F.-R. E. Mechanosensing at the Vascular Interface. *Annu. Rev. Biomed. Eng.* **16,** 505–532 (2014).

57. Fletcher, D. A. & Mullins, R. D. Cell mechanics and the cytoskeleton. *Nature* **463,** 485–492 (2010).

58. Seong, J., Wang, N. & Wang, Y. Mechanotransduction at focal adhesions: From physiology to cancer development. *J. Cell. Mol. Med.* **17,** 597–604 (2013).

59. Guo, P., Cai, B., Lei, M., Liu, Y. & Fu, B. M. Differential arrest and adhesion of tumor cells and microbeads in the microvasculature. *Biomech. Model. Mechanobiol.* **13,** 537–50 (2014).

60. Wirtz, D., Konstantopoulos, K. & Searson, P. C. P. P. C. The physics of cancer: the role of physical interactions and mechanical forces in metastasis. *Nat. Rev. Cancer* **11,** 522 (2011).

61. Follain, G. *et al.* Hemodynamic Forces Tune the Arrest, Adhesion, and Extravasation of Circulating Tumor Cells. *Dev. Cell* **45,** 33–52.e12 (2018).

62. Coleman, R. E. & Rubens, R. D. The clinical course of bone metastases from breast cancer. *Br. J. Cancer* **55,** 61–6 (1987).

63. Chambers, A. F., Groom, A. C. & MacDonald, I. C. Dissemination and growth of cancer cells in metastatic sites. *Nat. Rev. Cancer* **2,** 563–72 (2002).

64. Cameron, M. D. *et al.* Temporal progression of metastasis in lung: cell survival,

dormancy, and location dependence of metastatic inefficiency. *Cancer Res.* **60,** 2541–6 (2000).

65. Ding, L. *et al.* In vivo evaluation of the early events associated with liver metastasis of circulating cancer cells. *Br. J. Cancer* **85,** 431–8 (2001).

66. McCarty, O. J., Mousa, S. A., Bray, P. F. & Konstantopoulos, K. Immobilized platelets support human colon carcinoma cell tethering, rolling, and firm adhesion under dynamic flow conditions. *Blood* **96,** 1789–97 (2000).

67. Burdick, M. M., McCaffery, J. M., Kim, Y. S., Bochner, B. S. & Konstantopoulos, K. Colon carcinoma cell glycolipids, integrins, and other glycoproteins mediate adhesion to HUVECs under flow. *Am. J. Physiol. Cell Physiol.* **284,** C977-87 (2003).

68. Tzima, E. *et al.* A mechanosensory complex that mediates the endothelial cell response to fluid shear stress. *Nature* **437,** 426–31 (2005).

69. Bao, G. & Suresh, S. Cell and molecular mechanics of biological materials. *Nat. Mater.* **2,** 715–725 (2003).

70. Muhamed, I., Chowdhury, F. & Maruthamuthu, V. Biophysical Tools to Study Cellular Mechanotransduction. *Bioeng. (Basel, Switzerland)* **4,** (2017).

71. Kam, Y., Guess, C., Estrada, L., Weidow, B. & Quaranta, V. A novel circular invasion assay mimics in vivo invasive behavior of cancer cell lines and distinguishes single-cell motility in vitro. *BMC Cancer* **8,** 198 (2008).

72. Kramer, N. *et al.* In vitro cell migration and invasion assays. *Mutat. Res.* **752,** 10–24 (2013).

73. Suresh, S. Biomechanics and biophysics of cancer cells. *Acta Biomater.* **3,** 413–38 (2007).

74. Boussommier-Calleja, A., Li, R., Chen, M. B., Wong, S. C. & Kamm, R. D.

Microfluidics: A new tool for modeling cancer-immune interactions. *Trends in cancer* **2,** 6–19 (2016).

75. Verhulsel, M. *et al.* A review of microfabrication and hydrogel engineering for micro-organs on chips. *Biomaterials* **35,** 1816–32 (2014).

76. Huh, D. *et al.* Reconstituting organ-level lung functions on a chip. *Science* **328,** 1662–8 (2010).

77. Kim, H. J., Huh, D., Hamilton, G. & Ingber, D. E. Human gut-on-a-chip inhabited by microbial flora that experiences intestinal peristalsis-like motions and flow. *Lab Chip* **12,** 2165–74 (2012).

78. Lee, P. J., Hung, P. J. & Lee, L. P. An artificial liver sinusoid with a microfluidic endothelial-like barrier for primary hepatocyte culture. *Biotechnol. Bioeng.* **97,** 1340–6 (2007).

79. Zheng, Y. *et al.* In vitro microvessels for the study of angiogenesis and thrombosis. *Proc. Natl. Acad. Sci. U. S. A.* **109,** 9342–7 (2012).

80. Chen, M. B., Whisler, J. A., Jeon, J. S. & Kamm, R. D. Mechanisms of tumor cell extravasation in an in vitro microvascular network platform. *Integr. Biol. (Camb).* **5,** 1262–71 (2013).

81. Jeon, J. S., Zervantonakis, I. K., Chung, S., Kamm, R. D. & Charest, J. L. In Vitro Model of Tumor Cell Extravasation. *PLoS One* **8,** (2013).

82. Riahi, R. *et al.* A microfluidic model for organ-specific extravasation of circulating tumor cells. *Biomicrofluidics* **8,** 024103 (2014).

83. Preira, P. *et al.* Microfluidic tools to investigate pathologies in the blood microcirculation. *Int. J. Nanotechnol.* **9,** 529 (2012).

84. Preira, P. *et al.* Passive circulating cell sorting by deformability using a microfluidic

gradual filter. *Lab Chip* **13,** 161–70 (2013).

85. Preira, P. *et al.* The leukocyte-stiffening property of plasma in early acute respiratory distress syndrome (ARDS) revealed by a microfluidic single-cell study: the role of cytokines and protection with antibodies. *Crit. Care* **20,** 8 (2016).

86. Rathod, M. L., Ahn, J., Jeon, N. L. & Lee, J. Hybrid polymer microfluidic platform to mimic varying vascular compliance and topology. *Lab Chip* **17,** 2508–2516 (2017).

87. Regmi, S., Fu, A. & Luo, K. Q. High Shear Stresses under Exercise Condition Destroy Circulating Tumor Cells in a Microfluidic System. *Sci. Rep.* **7,** 39975 (2017).

88. Chivukula, V. K., Krog, B. L., Nauseef, J. T., Henry, M. D. & Vigmostad, S. C. Alterations in cancer cell mechanical properties after fluid shear stress exposure: a micropipette aspiration study. *Cell Health Cytoskelet.* **7,** 25–35 (2015).

89. Shaw Bagnall, J. *et al.* Deformability of Tumor Cells versus Blood Cells. *Sci. Rep.* **5,** 18542 (2015).

90. Davidson, P. M., Denais, C., Bakshi, M. C. & Lammerding, J. Nuclear deformability constitutes a rate-limiting step during cell migration in 3-D environments. *Cell. Mol. Bioeng.* **7,** 293–306 (2014).

91. Thiam, H.-R. *et al.* Perinuclear Arp2/3-driven actin polymerization enables nuclear deformation to facilitate cell migration through complex environments. *Nat. Commun.* **7,** 10997 (2016).

92. Raab, M. *et al.* ESCRT III repairs nuclear envelope ruptures during cell migration to limit DNA damage and cell death. *Science* **352,** 359–62 (2016).

93. Denais, C. M. *et al.* Nuclear envelope rupture and repair during cancer cell migration. *Science* **352,** 353–8 (2016).

94. Irianto, J. *et al.* DNA Damage Follows Repair Factor Depletion and Portends Genome

Variation in Cancer Cells after Pore Migration. *Curr. Biol.* **27,** 210–223 (2017).

95. Zhang, W., Kai, K., Ueno, N. T. & Qin, L. A Brief Review of the Biophysical Hallmarks of Metastatic Cancer Cells. *Cancer Hallm.* **1,** 59–66 (2013).

96. Song, J. W. *et al.* Microfluidic endothelium for studying the intravascular adhesion of metastatic breast cancer cells. *PLoS One* **4,** e5756 (2009).

97. Rother, J., Noding, H., Mey, I. & Janshoff, A. Atomic force microscopy-based microrheology reveals significant differences in the viscoelastic response between malign and benign cell lines. *Open Biol.* **4,** 140046–140046 (2014).

98. Simi, A. K., Piotrowski, A. S. & Nelson, C. M. Mechanotransduction, Metastasis and Genomic Instability. in **20,** 139–158 (2015).

99. Liu, Y. J. *et al.* Confinement and low adhesion induce fast amoeboid migration of slow mesenchymal cells. *Cell* **160,** 659–672 (2015).

100. Schneider, D., Tarantola, M. & Janshoff, A. Dynamics of TGF-β induced epithelial-to-mesenchymal transition monitored by electric cell-substrate impedance sensing. *Biochim. Biophys. Acta* **1813,** 2099–107 (2011).

101. Lee, J., Choi, J.-H. & Joo, C.-K. TGF-β1 regulates cell fate during epithelial-mesenchymal transition by upregulating survivin. *Cell Death Dis.* **4,** e714 (2013).

102. Bustin, S. A. *et al.* The MIQE guidelines: minimum information for publication of quantitative real-time PCR experiments. *Clin. Chem.* **55,** 611–22 (2009).

103. Fay, M. P. & Proschan, M. a. Wilcoxon-Mann-Whitney or t-test? On assumptions for hypothesis tests and multiple interpretations of decision rules. *Stat. Surv.* **4,** 1–39 (2010).

104. Noble, W. S. How does multiple testing correction work? *Nat. Biotechnol.* **27,** 1135–7 (2009).

105. Storey, J. D. & Tibshirani, R. Statistical significance for genomewide studies. *Proc. Natl. Acad. Sci. U. S. A.* **100,** 9440–5 (2003).

106. Sajeesh, P., Raj, A., Doble, M. & Sen, A. K. Characterization and sorting of cells based on stiffness contrast in a microfluidic channel. *RSC Adv.* **6,** 74704–74714 (2016).

107. Alonso, J. L. & Goldmann, W. H. Feeling the forces: atomic force microscopy in cell biology. *Life Sci.* **72,** 2553–60 (2003).

108. Kirmizis, D. & Logothetidis, S. Atomic force microscopy probing in the measurement of cell mechanics. *Int. J. Nanomedicine* **5,** 137–45 (2010).

109. Zhang, H. & Liu, K.-K. Optical tweezers for single cells. *J. R. Soc. Interface* **5,** 671–90 (2008).

110. Hochmuth, R. M. Micropipette aspiration of living cells. *J. Biomech.* **33,** 15–22 (2000).

111. Shao, Y. *et al.* Uniaxial cell stretching device for live-cell imaging of mechanosensitive cellular functions. *Rev. Sci. Instrum.* **84,** 114304 (2013).

112. Lekka, M. Discrimination Between Normal and Cancerous Cells Using AFM. *Bionanoscience* **6,** 65–80 (2016).

113. Bathe, M., Shirai, A., Doerschuk, C. M. & Kamm, R. D. Neutrophil Transit Times through Pulmonary Capillaries: The Effects of Capillary Geometry and fMLP-Stimulation. *Biophys. J.* **83,** 1917–1933 (2002).

114. Nyberg, K. D. *et al.* Predicting cancer cell invasion by single-cell physical phenotyping. *Integr. Biol. (Camb).* **10,** 218–231 (2018).

115. Ye, T., Shi, H., Phan-Thien, N., Lim, C. T. & Li, Y. Relationship between transit time and mechanical properties of a cell through a stenosed microchannel. *Soft Matter* **14,**

533–545 (2018).

116. Huang, H. Cell mechanics and mechanotransduction: pathways, probes, and physiology. *AJP Cell Physiol.* **287,** C1–C11 (2004).

117. Allioux-Guérin, M. *et al.* Spatiotemporal Analysis of Cell Response to a Rigidity Gradient: A Quantitative Study Using Multiple Optical Tweezers. *Biophys. J.* **96,** 238–247 (2009).

118. Nyberg, K. D. *et al.* The physical origins of transit time measurements for rapid, single cell mechanotyping. *Lab Chip* **16,** 3330–9 (2016).

119. Morel, A.-P. *et al.* EMT inducers catalyze malignant transformation of mammary epithelial cells and drive tumorigenesis towards claudin-low tumors in transgenic mice. *PLoS Genet.* **8,** e1002723 (2012).

120. Brabletz, T., Kalluri, R., Nieto, M. A. & Weinberg, R. A. EMT in cancer. *Nat. Rev. Cancer* **18,** 128–134 (2018).

121. Giuliano, M. *et al.* Circulating tumor cells as early predictors of metastatic spread in breast cancer patients with limited metastatic dissemination. *Breast Cancer Res.* **16,** 440 (2014).

122. Rack, B. *et al.* Circulating tumor cells predict survival in early average-to-high risk breast cancer patients. *J. Natl. Cancer Inst.* **106,** 134–137 (2014).

123. Zhang, Y., Lv, Y., Niu, Y., Su, H. & Feng, A. Role of Circulating Tumor Cell (CTC) Monitoring in Evaluating Prognosis of Triple-Negative Breast Cancer Patients in China. *Med. Sci. Monit.* **23,** 3071–3079 (2017).

124. Wong, I. Y. *et al.* Collective and individual migration following the epithelial-mesenchymal transition. *Nat. Mater.* **13,** 1063–71 (2014).

125. Samatov, T. R., Shkurnikov, M. U., Tonevitskaya, S. A. & Tonevitsky, A. G.

Modelling the metastatic cascade by in vitro microfluidic platforms. *Prog. Histochem. Cytochem.* **49,** 21–29 (2015).

126. Sherman, M. H., Bassing, C. H. & Teitell, M. a. Regulation of cell differentiation by the DNA damage response. *Trends Cell Biol.* **21,** 312–9 (2011).

127. Park, Y.-Y. *et al.* FOXM1 mediates Dox resistance in breast cancer by enhancing DNA repair. *Carcinogenesis* **33,** 1843–53 (2012).

128. Tobin, L. A. *et al.* Targeting abnormal DNA repair in therapy-resistant breast cancers. *Mol. Cancer Res.* **10,** 96–107 (2012).

129. Cheung-Ong, K., Giaever, G. & Nislow, C. DNA-damaging agents in cancer chemotherapy: serendipity and chemical biology. *Chem. Biol.* **20,** 648–59 (2013).

130. Woods, D. & Turchi, J. J. Chemotherapy induced DNA damage response: convergence of drugs and pathways. *Cancer Biol. Ther.* **14,** 379–89 (2013).

131. Gong, C. *et al.* Potentiated DNA Damage Response in Circulating Breast Tumor Cells Confers Resistance to Chemotherapy. *J. Biol. Chem.* **290,** 14811–25 (2015).

132. Pasquier, J., Abu-kaoud, N., Thani, H. Al & Rafii, A. Epithelial to Mesenchymal Transition in a Clinical Perspective. **2015,** 19–21 (2015).

133. Jia, Y. *et al.* Transforming growth factor-β1 regulates epithelial-mesenchymal transition in association with cancer stem-like cells in a breast cancer cell line. *Int. J. Clin. Exp. Med.* **7,** 865–72 (2014).

134. Phillips, K. G., Kuhn, P. & McCarty, O. J. T. Physical biology in cancer. 2. The physical biology of circulating tumor cells. *Am. J. Physiol. Cell Physiol.* **306,** C80-8 (2014).

135. Sarioglu, A. F. *et al.* A microfluidic device for label-free, physical capture of circulating tumor cell clusters. *Nat. Methods* **12,** 685–691 (2015).

136. Ozkumur, E. *et al.* Inertial focusing for tumor antigen-dependent and -independent sorting of rare circulating tumor cells. *Sci. Transl. Med.* **5,** 179ra47 (2013).

137. Harouaka, R. a., Nisic, M. & Zheng, S.-Y. Circulating tumor cell enrichment based on physical properties. *J. Lab. Autom.* **18,** 455–68 (2013).

138. Malhotra, S., Kazlouskaya, V., Andres, C., Gui, J. & Elston, D. Diagnostic cellular abnormalities in neoplastic and non-neoplastic lesions of the epidermis: a morphological and statistical study. *J. Cutan. Pathol.* **40,** 371–8 (2013).

139. Jackson, S. P. & Bartek, J. The DNA-damage response in human biology and disease. *Nature* **461,** 1071–8 (2009).

140. Ciccia, A. & Elledge, S. J. The DNA damage response: making it safe to play with knives. *Mol. Cell* **40,** 179–204 (2010).

141. Giglia-Mari, G., Zotter, A. & Vermeulen, W. DNA damage response. *Cold Spring Harb. Perspect. Biol.* **3,** a000745 (2011).

142. Friedberg, E. C., McDaniel, L. D. & Schultz, R. A. The role of endogenous and exogenous DNA damage and mutagenesis. *Curr. Opin. Genet. Dev.* **14,** 5–10 (2004).

143. Hoeijmakers, J. H. Genome maintenance mechanisms for preventing cancer. *Nature* **411,** 366–74 (2001).

144. Burgess, R. C. & Misteli, T. Not All DDRs Are Created Equal: Non-Canonical DNA Damage Responses. *Cell* **162,** 944–7 (2015).

145. Moreno-Smith, M., Lutgendorf, S. K. & Sood, A. K. Impact of stress on cancer metastasis. *Future Oncol.* **6,** 1863–81 (2010).

146. Liou, G.-Y. & Storz, P. Reactive oxygen species in cancer. *Free Radic. Res.* **44,** 479–96 (2010).

147. Ackerman, D. & Simon, M. C. Hypoxia, lipids, and cancer: surviving the harsh tumor

microenvironment. *Trends Cell Biol.* **24,** 472–8 (2014).

148. Miroshnikova, Y. A., Nava, M. M. & Wickström, S. A. Emerging roles of mechanical forces in chromatin regulation. *J. Cell Sci.* **130,** 2243–2250 (2017).

149. Singh, M. *et al.* Lamin A/C depletion enhances DNA damage-induced stalled replication fork arrest. *Mol. Cell. Biol.* **33,** 1210–22 (2013).

150. Sirbu, B. M. & Cortez, D. DNA damage response: three levels of DNA repair regulation. *Cold Spring Harb. Perspect. Biol.* **5,** a012724 (2013).

151. Nam, S. *et al.* A pathway-based approach for identifying biomarkers of tumor progression to trastuzumab-resistant breast cancer. *Cancer Lett.* **356,** 880–90 (2015).

152. Wu, Y. & Zhou, B. P. More than EMT. *Cell Adhes. Migr.* **4,** 199–203 (2010).

153. Liu, Y. *et al.* YAP modulates TGF-β1-induced simultaneous apoptosis and EMT through upregulation of the EGF receptor. *Sci. Rep.* **7,** 45523 (2017).

154. Wang, Y., Shi, J., Chai, K., Ying, X. & Zhou, B. P. The Role of Snail in EMT and Tumorigenesis. *Curr. Cancer Drug Targets* **13,** 963–72 (2013).

155. De Craene, B. & Berx, G. Regulatory networks defining EMT during cancer initiation and progression. *Nat. Rev. Cancer* **13,** 97–110 (2013).

156. Vandewalle, C. *et al.* SIP1/ZEB2 induces EMT by repressing genes of different epithelial cell-cell junctions. *Nucleic Acids Res.* **33,** 6566–78 (2005).

157. Aigner, K. *et al.* The transcription factor ZEB1 (deltaEF1) promotes tumour cell dedifferentiation by repressing master regulators of epithelial polarity. *Oncogene* **26,** 6979–88 (2007).

158. Thiery, J. P., Acloque, H., Huang, R. Y. J. & Nieto, M. A. Epithelial-Mesenchymal Transitions in Development and Disease. *Cell* **139,** 871–890 (2009).

159. Maestro, R. *et al.* Twist is a potential oncogene that inhibits apoptosis. *Genes Dev.* **13,**

2207–17 (1999).

160. Vega, S. *et al.* Snail blocks the cell cycle and confers resistance to cell death. *Genes Dev.* **18,** 1131–43 (2004).

161. Wu, W.-S. *et al.* Slug antagonizes p53-mediated apoptosis of hematopoietic progenitors by repressing puma. *Cell* **123,** 641–53 (2005).

162. Derksen, P. W. B. *et al.* Somatic inactivation of E-cadherin and p53 in mice leads to metastatic lobular mammary carcinoma through induction of anoikis resistance and angiogenesis. *Cancer Cell* **10,** 437–49 (2006).

163. Cano, A. *et al.* The transcription factor snail controls epithelial-mesenchymal transitions by repressing E-cadherin expression. *Nat. Cell Biol.* **2,** 76–83 (2000).

164. Shirley, S. H. *et al.* Slug expression during melanoma progression. *Am. J. Pathol.* **180,** 2479–89 (2012).

165. Martin, A. & Cano, A. Tumorigenesis: Twist1 links EMT to self-renewal. *Nat. Cell Biol.* **12,** 924–5 (2010).

166. Brabletz, T. EMT and MET in metastasis: where are the cancer stem cells? *Cancer Cell* **22,** 699–701 (2012).

167. Damonte, P., Gregg, J. P., Borowsky, A. D., Keister, B. A. & Cardiff, R. D. EMT tumorigenesis in the mouse mammary gland. *Lab. Invest.* **87,** 1218–26 (2007).

168. Trimboli, A. J. *et al.* Direct evidence for epithelial-mesenchymal transitions in breast cancer. *Cancer Res.* **68,** 937–45 (2008).

169. Morel, A.-P. *et al.* Generation of breast cancer stem cells through epithelial-mesenchymal transition. *PLoS One* **3,** e2888 (2008).

170. Santisteban, M. *et al.* Immune-induced epithelial to mesenchymal transition in vivo generates breast cancer stem cells. *Cancer Res.* **69,** 2887–95 (2009).

171. Bersini, S., Jeon, J. S., Moretti, M. & Kamm, R. D. In vitro models of the metastatic cascade: from local invasion to extravasation. *Drug Discov. Today* **19,** 735–42 (2014).

172. Bersini, S. *et al.* A microfluidic 3D invitro model for specificity of breast cancer metastasis to bone. *Biomaterials* **35,** 2454–2461 (2014).

173. Bissell, M. J., Radisky, D. C. & Nistico, P. Epithelial-Mesenchymal Transition : General Principles and Pathological Relevance with Special Emphasis on the Role of Matrix Metalloproteinases. *Cold Spring Harb. Perspect. Biol.* **4,** 1–12 (2016).

174. Meng, S. *et al.* Circulating tumor cells in patients with breast cancer dormancy. *Clin. Cancer Res.* **10,** 8152–62 (2004).

175. Stott, S. L. *et al.* Isolation and characterization of circulating tumor cells from patients with localized and metastatic prostate cancer. *Sci. Transl. Med.* **2,** 25ra23 (2010).

176. Aceto, N. *et al.* Circulating tumor cell clusters are oligoclonal precursors of breast cancer metastasis. *Cell* **158,** 1110–1122 (2014).

177. Su, B. *et al.* Diallyl disulfide inhibits TGF□β1□induced upregulation of Rac1 and β□catenin in epithelial□mesenchymal transition and tumor growth of gastric cancer. *Oncol. Rep.* **39,** 2797–2806 (2018).

178. Xu, J., Lamouille, S. & Derynck, R. TGF-beta-induced epithelial to mesenchymal transition. *Cell Res.* **19,** 156–72 (2009).

179. Zhan, T., Rindtorff, N. & Boutros, M. Wnt signaling in cancer. *Oncogene* **36,** 1461–1473 (2017).

180. Barnett, N. P. *et al.* Moderators and mediators of two brief interventions for alcohol in the emergency department. *Addiction* **105,** 452–65 (2010).

181. Cai, K. *et al.* Downregulation of β-catenin decreases the tumorigenicity, but promotes epithelial-mesenchymal transition in breast cancer cells. *J. Cancer Res. Ther.* **10,**

1063–70 (2014).

182. Satelli, A. & Li, S. Vimentin as a potential molecular target in cancer therapy Or Vimentin, an overview and its potential as a molecular target for cancer therapy. *Cell Mol Life Sci.* **68,** 3033–3046 (2011).

183. Gilles, C. *et al.* Transactivation of vimentin by beta-catenin in human breast cancer cells. *Cancer Res.* **63,** 2658–64 (2003).

184. Satelli, A., Hu, J., Xia, X. & Li, S. Potential Function of Exogenous Vimentin on the Activation of Wnt Signaling Pathway in Cancer Cells. *J. Cancer* **7,** 1824–1832 (2016).

185. Carver, E. a, Jiang, R., Lan, Y., Oram, K. F. & Gridley, T. The mouse snail gene encodes a key regulator of the epithelial-mesenchymal transition. *Mol. Cell. Biol.* **21,** 8184–8 (2001).

186. Francí, C. *et al.* Expression of Snail protein in tumor-stroma interface. *Oncogene* **25,** 5134–44 (2006).

187. Murray, S. A. & Gridley, T. Snail family genes are required for left-right asymmetry determination, but not neural crest formation, in mice. *Proc. Natl. Acad. Sci. U. S. A.* **103,** 10300–10304 (2006).

188. Vincent, T. *et al.* A SNAIL1-SMAD3/4 transcriptional repressor complex promotes TGF-beta mediated epithelial-mesenchymal transition. *Nat. Cell Biol.* **11,** 943–50 (2009).

189. Duncan, M. C., Costaguta, G. & Payne, G. S. Yeast epsin-related proteins required for Golgi-endosome traffic define a gamma-adaptin ear-binding motif. *Nat. Cell Biol.* **5,** 77–81 (2003).

190. Xu, B. *et al.* The endothelial cell-specific antibody PAL-E identifies a secreted form of vimentin in the blood vasculature. *Mol. Cell. Biol.* **24,** 9198–206 (2004).

191. van Roy, F. Beyond E-cadherin: roles of other cadherin superfamily members in cancer. *Nat. Rev. Cancer* **14,** 121–34 (2014).

192. Hiraguri, S. *et al.* Mechanisms of inactivation of E-cadherin in breast cancer cell lines. *Cancer Res.* **58,** 1972–7 (1998).

193. Creedon, H. *et al.* Identification of novel pathways linking epithelial-to-mesenchymal transition with resistance to HER2-targeted therapy. *Oncotarget* **7,** 11539–52 (2016).

194. Maggiorani, D. *et al.* Shear Stress-Induced Alteration of Epithelial Organization in Human Renal Tubular Cells. *PLoS One* **10,** e0131416 (2015).

195. Chu, K., Boley, K. M., Moraes, R., Barsky, S. H. & Robertson, F. M. The paradox of E-cadherin: role in response to hypoxia in the tumor microenvironment and regulation of energy metabolism. *Oncotarget* **4,** 446–62 (2013).

196. Yang, J. *et al.* Twist, a master regulator of morphogenesis, plays an essential role in tumor metastasis. *Cell* **117,** 927–939 (2004).

197. Fang, X. *et al.* Twist2 contributes to breast cancer progression by promoting an epithelial-mesenchymal transition and cancer stem-like cell self-renewal. *Oncogene* **30,** 4707–20 (2011).

198. Fan, Y. L., Zheng, M., Tang, Y. L. & Liang, X. H. A new perspective of vasculogenic mimicry: EMT and cancer stem cells (review). *Oncol. Lett.* **6,** 1174–1180 (2013).

199. Tran, D. D., Corsa, C. A. S., Biswas, H., Aft, R. L. & Longmore, G. D. Temporal and spatial cooperation of Snail1 and Twist1 during epithelial-mesenchymal transition predicts for human breast cancer recurrence. *Mol. Cancer Res.* **9,** 1644–57 (2011).

200. Tsai, J. H. & Yang, J. Epithelial-mesenchymal plasticity in carcinoma metastasis. *Genes Dev.* **27,** 2192–206 (2013).

201. Gomez, E. W., Chen, Q. K., Gjorevski, N. & Nelson, C. M. Tissue geometry patterns

epithelial-mesenchymal transition via intercellular mechanotransduction. *J. Cell. Biochem.* **110,** n/a-n/a (2010).

202. Gjorevski, N., Boghaert, E. & Nelson, C. M. Regulation of Epithelial-Mesenchymal Transition by Transmission of Mechanical Stress through Epithelial Tissues. *Cancer Microenviron.* **5,** 29–38 (2012).

203. Ansieau, S., Collin, G. & Hill, L. EMT or EMT-Promoting Transcription Factors, Where to Focus the Light? *Front. Oncol.* **4,** 353 (2014).

204. Li, M. *et al.* Epithelial-mesenchymal transition: An emerging target in tissue fibrosis. *Exp. Biol. Med. (Maywood).* **241,** 1–13 (2016).

205. Imani, S., Hosseinifard, H., Cheng, J., Wei, C. & Fu, J. Prognostic Value of EMT-inducing Transcription Factors (EMT-TFs) in Metastatic Breast Cancer: A Systematic Review and Meta-analysis. *Sci. Rep.* **6,** 28587 (2016).

206. Bastid, J., Ciancia, C., Puisieux, A. & Ansieau, S. Role of TWIST proteins in cancer progression. *Atlas Genet. Cytogenet. Oncol. Haematol.* **18,** 113–24 (2011).

207. Kress, W. *et al.* Saethre-Chotzen syndrome caused by TWIST 1 gene mutations: functional differentiation from Muenke coronal synostosis syndrome. *Eur. J. Hum. Genet.* **14,** 39–48 (2006).

208. Murray, S. S. *et al.* Expression of helix-loop-helix regulatory genes during differentiation of mouse osteoblastic cells. *J. Bone Miner. Res.* **7,** 1131–8 (1992).

209. Hebrok, M., Wertz, K. & Füchtbauer, E. M. M-twist is an inhibitor of muscle differentiation. *Dev. Biol.* **165,** 537–44 (1994).

210. Spicer, D. B., Rhee, J., Cheung, W. L. & Lassar, A. B. Inhibition of myogenic bHLH and MEF2 transcription factors by the bHLH protein Twist. *Science* **272,** 1476–80 (1996).

211. Lee, Y. S. *et al.* Twist2, a novel ADD1/SREBP1c interacting protein, represses the transcriptional activity of ADD1/SREBP1c. *Nucleic Acids Res.* **31,** 7165–74 (2003).

212. Tukel, T. *et al.* Homozygous nonsense mutations in TWIST2 cause Setleis syndrome. *Am. J. Hum. Genet.* **87,** 289–96 (2010).

213. Ansieau, S. *et al.* Induction of EMT by Twist Proteins as a Collateral Effect of Tumor-Promoting Inactivation of Premature Senescence. *Cancer Cell* **14,** 79–89 (2008).

214. Cabrera Je, E. The Role of Transcription Factor TWIST in Cancer Cells. *J. Genet. Syndr. Gene Ther.* **04,** 1–7 (2013).

215. Mao, Y. *et al.* Significance of heterogeneous Twist2 expression in human breast cancers. *PLoS One* **7,** e48178 (2012).

216. Vogel, C. & Marcotte, E. M. Insights into the regulation of protein abundance from proteomic and transcriptomic analyses. *Nat. Rev. Genet.* **13,** 227–32 (2012).

217. Wang, P. *et al.* WDR5 modulates cell motility and morphology and controls nuclear changes induced by a 3D environment. *Proc. Natl. Acad. Sci. U. S. A.* 201719405 (2018). doi:10.1073/pnas.1719405115

218. Enyedi, B., Jelcic, M. & Niethammer, P. The Cell Nucleus Serves as a Mechanotransducer of Tissue Damage-Induced Inflammation. *Cell* **165,** 1160–1170 (2016).

219. Yang, C., Tibbitt, M. W., Basta, L. & Anseth, K. S. Mechanical memory and dosing influence stem cell fate. *Nat. Mater.* **13,** 645–52 (2014).

220. Pawlowska, E. & Blasiak, J. DNA Repair--A Double-Edged Sword in the Genomic Stability of Cancer Cells--The Case of Chronic Myeloid Leukemia. *Int. J. Mol. Sci.* **16,** 27535–49 (2015).

221. Ivashkevich, A., Redon, C. E., Nakamura, A. J., Martin, R. F. & Martin, O. A. Use of

the γ-H2AX assay to monitor DNA damage and repair in translational cancer research. *Cancer Lett.* **327,** 123–33 (2012).

222. Mariotti, L. G. *et al.* Use of the γ-H2AX assay to investigate DNA repair dynamics following multiple radiation exposures. *PLoS One* **8,** e79541 (2013).

223. Farge, E. Mechanical induction of Twist in the Drosophila foregut/stomodeal primordium. *Curr. Biol.* **13,** 1365–77 (2003).